

Analysis of Femtosecond Electron Bunches at the SwissFEL Injector Test Facility

THÈSE N° 6570 (2015)

PRÉSENTÉE LE 29 AVRIL 2015

À LA FACULTÉ DES SCIENCES DE BASE
LABORATOIRE DE PHYSIQUE DES ACCÉLÉRATEURS DE PARTICULES
PROGRAMME DOCTORAL EN PHYSIQUE

ÉCOLE POLYTECHNIQUE FÉDÉRALE DE LAUSANNE

POUR L'OBTENTION DU GRADE DE DOCTEUR ÈS SCIENCES

PAR

Bennie SMIT

acceptée sur proposition du jury:

Prof. V. Savona, président du jury
Prof. L. Rivkin, Dr R. Ischebeck, directeurs de thèse
Prof. C. P. Hauri, rapporteur
Dr H. Schlarb, rapporteur
Prof. C. P. Welsch, rapporteur



ÉCOLE POLYTECHNIQUE
FÉDÉRALE DE LAUSANNE

Suisse
2015

To my family

Acknowledgements

I am happy to be able to say that I have been part of the SwissFEL project. In the time this PhD was carried out, a precursor called the SwissFEL Injector Test Facility (SITF) was commissioned. Firstly, I would like to thank the people who made the SITF a success namely those in the Laser group, the RF group, beam dynamics, the vacuum group, the magnet group and the advanced instrumentation group. Without these teams the SITF would not be running. They have therefore contributed to the success of this thesis. My special thanks go to my colleagues of the advanced instrumentation group for giving me helpful feedback and discussions to ponder over.

This thesis would not be laying in front of you without my direct supervisor Rasmus Ischebeck. I would like to thank Rasmus for his great ideas, support, discussions and his tireless efforts. I would also like to thank my thesis director Prof. Rivkin for the opportunity to perform my doctoral studies at EPFL and for the critical observations in our meetings. I would also like to thank my superior Volker Schlott for discussions during our bi-weekly meetings and Thomas Schietinger for allocating beamtime and for communicating between groups such that the SITF ran as smoothly as possible.

Long nights have been spent in the control room gathering data for this thesis. I would like to thank the control room operators - invisible to most as they work 'behind the scenes' - in supporting me during times when no staff was available and for keeping me awake during my experiments. I would also like to thank the beam dynamics group in particular who taught me the machine physics. I would like to mention the great and the prompt support I got from the control group and the engineers, with in particular Albert Kammerer, Markus Baldinger and Martin Heiniger.

My family have been very important to me over the years and without their belief and support I would not be where I am now. Last but not least I would like to thank my wife Stephanie for her unconditional support and am proud to say she obtained her own PhD.

Karlsruhe, 10th January 2015

B. Smit

Preface

Free electron lasers have become the brightest X-ray sources on Earth. They allow for the observation of molecular structures on a femtosecond time scale, opening entirely new areas of research. The measurement of the pulse length of the X-rays, as well as the electron bunches used to generate them is thus of primary interest, and significant effort has been put into the development of time-resolved beam diagnostics.

The present thesis presents a thorough analysis of the spectral distribution of optical transition radiation generated by compressed electron bunches on a vacuum-metal interface. While the baseline diagnostics for SwissFEL makes use of Schottky diodes to measure the terahertz spectrum of edge and diffraction radiation, the present analysis is based on visible light. It is shown here that the optical transition radiation spectrum depends on bunch length and shape. Using visible light gives access to commercially available spectrometers, equipped with quantum detectors that have a noise equivalent pulse energy of less than one femtojoule.

Experiments were performed at the SwissFEL Injector Test Facility. Since the nominal operation regime of this test accelerator does not extend to bunch lengths of ten femtoseconds, a special non-linear compression scheme was set up by varying the X-band RF acceleration phase. The analysis of the bunch length with the transverse deflecting cavity required special care, because transverse space charge fields present at the relatively low energies impeded the usual methods. To this purpose, a novel method to extract the bunch length from the data is presented.

The experimental results of the bunch length measurement using spectral fluctuations show a promising route towards a diagnostics for the fully compressed beams at SwissFEL.

PSI, 24th October 2014

Dr. R. Ischebeck

Zusammenfassung

Der SwissFEL (Swiss Free Electron Laser) ist ein Freie-Elektronen-Laser, der am Paul-Scherrer-Institut gebaut wird. SwissFEL wird eine Nutzeranlage, um Prozesse auf bis dato unerkundeten Raum- und Zeitskalen zu studieren. Um diese Ziele zu erreichen, muss der Freie-Elektronen-Laser Röntgenpulse erzeugen, die wenige Femtosekunden lang sind. Die Pulslänge der Elektronenpakete vom Teilchenbeschleuniger muss daher ähnlich kurz sein. Um solch kurze Elektronenpakete zu erzeugen, muss die Länge nach jedem Kompressionsschritt überwacht werden. Diese Arbeit legt zwei neuartige Methoden dar, um solche Elektronenpakete zu vermessen: eine neue spektrale Methode, die den Frequenzraum der Elektronen analysiert, und die mit kürzer werdenden Pulslängen einfacher wird, sowie eine Methode, die einen transversal ablenkenden Hohlraumresonator verwendet und die konzeptionell eine Pulslänge von Null messen kann.

Da SwissFEL zur Zeit der Erstellung dieser Doktorarbeit noch nicht fertig gestellt war, wurden alle Experimente an der SwissFEL-Injektor-Testanlage (SwissFEL Injector Test Facility, SITF) durchgeführt. SITF ist ein Linearbeschleuniger, der Elektronen auf eine Energie von 200 MeV bringt. Die Pulslänge wird in der linearen Theorie nur durch die unkorrelierte Energieunschärfe und durch höhere Ordnungen des Pulscompressors beschränkt. In der Tat treten allerdings durch die niedrige Elektronenenergie bei kurzer Pulslänge Raumladungskräfte auf, welche die Strahldynamik sowohl im transversalen als auch im longitudinalen Phasenraum dominieren. Während man mit linearer Strahldynamik eine Pulslänge von 6 fs rms erreichen könnte, führen diese Raumladungskräfte dazu, dass die tatsächliche minimale Pulslänge 20 fs rms beträgt. Diese Messungen wurden durch ein numerisches Modell bestätigt.

Ein transversal ablenkender Hohlraumresonator (Transverse Deflecting Cavity, TDC) wurde für eine Referenzmessung der Pulslänge verwendet, mit der dann die spektralen Fluktuationen korreliert wurden. Im TDC steht das elektrische Feld senkrecht auf die Strahlrichtung, was dazu führt, dass der vordere und hintere Teil des Elektronenpulses in unterschiedliche Richtungen beschleunigt werden. In einer konventionellen Messung mit dem TDC wird die Strahlgrösse auf die Zeitachse projiziert, um das Stromprofil zu erhalten. Dies setzt voraus, dass die Strahlbreite hinreichend klein ist. Allerdings ist in der SITF auf Grund der genannten Raumladungseffekte die intrinsische Strahlbreite relativ gross. Daher wurde eine neuartige Analyseverfahren für raumladungsdominierte Strahlen entwickelt.

In der vorgeschlagenen Analyseverfahren wurde eine dispersive Sektion zusammen mit dem TDC verwendet, um den longitudinalen Phasenraum darzustellen. Dieser Phasenraum wurde in der Impulsrichtung in Segmente unterteilt, und in jedem dieser Segmente wurde der

Unterschied zwischen der intrinsischen Strahlgrösse und der Strahlgrösse nach dem TDC bestimmt. Die Pulslänge wurde aus diesen Daten gewonnen, indem die Zeiten für alle Segmente bestimmt wurde. Sowohl die Simulationen als auch das Experiment zeigen, dass diese Methode es ermöglicht, die Pulslänge von raumladungsdominierten Elektronenpulsen zu bestimmen, wenn die intrinsische Strahlbreite gross ist. Die kleinste simulierte Pulslänge hat die gleiche Grössenordnung wie die Messung: 19,5 fs bzw. 24,5 fs. Da die Auflösung der TDC am PSI mit 20 fs bei einer Pulsladung von 200 pC spezifiziert ist, kann diese Methode verwendet werden, um die Auflösung der Messung zu verbessern.

Das Spektrum von Elektronenpulsen mit einer Länge von Femtosekunden enthält Informationen über die Pulslänge. Beim Aufprall des Elektronenstrahls auf eine Folie wird optische Übergangsstrahlung (Optical Transition Radiation ,OTR) emittiert. Diese Strahlung wird mit einem Spiegelaufbau auf einen Lichtwellenleiter fokussiert, der sie in ein optisches Spektrometer leitet. Das verwendete Spektrometer hat einen Bereich von 316 THz (950 nm) bis 1364 THz (220 nm). Das theoretisch erwartete flache Spektrum wurde gemessen. Bei einer Reduktion der Pulslänge unter 70 fs wurde eine periodische Fluktuation des Spektrums beobachtet. Diese Fluktuationen werden breiter, wenn die Pulslänge weiter verkürzt wird, und eine gute Übereinstimmung mit der Messung mit dem TDC wurde beobachtet.

Zusammenfassend kann gesagt werden, dass die Pulslänge mit einem TDC gemessen wurde, indem ein Bild auf einem Schirm in einer dispersiven Sektion analysiert wurde. Es wurde eine deutliche Korrelation zwischen der Pulslänge und der Breite der spektralen Fluktuationen beobachtet. Hiermit wurde gezeigt, dass sowohl die TDC als auch die spektralen Messungen ein grosses Potenzial haben, zu einem Standard für die Pulslängenmessung bei SwissFEL zu werden.

Schlüsselworte: SwissFEL, Elektronenstrahldiagnostik, Elektronenpulslänge

Abstract

The SwissFEL (Swiss Free Electron Laser) is a free electron laser which is being built at the Paul Scherrer Institute. The SwissFEL will be a user facility to study processes on unexplored scales of space and time. In order to achieve these aims the free electron laser must generate X-ray pulses on the order of femtoseconds. In order to deliver such short X-ray pulses, the electron bunch length, coming from the accelerator, must be comparable to the final X-ray pulse length. In order to achieve such a short electron bunch length, it must be monitored at every compression stage. This work proposes two novel methods to measure such electron bunches. The first of these is a novel spectral method, which analyses the frequency content of the short electron bunches and becomes easier as the bunch length becomes shorter. The second is a transverse deflecting cavity method in which the resolution depends on the energy resolution in a magnetic spectrometer.

Because the SwissFEL was not built at the time of the PhD, all experiments were performed at the SwissFEL Injector Test Facility (SITF). The SITF is a 200 MeV test bed linear electron accelerator. Theoretically the bunch length is limited due to the uncorrelated energy spread and the higher order components of the bunch compressor. However, due to the limited electron energy in combination with the short electron bunches, space charge effects dominate the beam in the transverse phase space as well as in the longitudinal phase space. Linear beam dynamics predicted a bunch length of 6 fs rms, however due to the space charge effects the shortest electron bunch length both measured and predicted by simulations was roughly 20 fs rms.

A transverse deflecting cavity (TDC) measurement was used to measure a reference bunch length to which the spectral fluctuations could be correlated. In a TDC the electric fields are oriented perpendicular to the beam direction and streaks the head and tail in opposite directions onto a screen. In a conventional TDC measurement, the projected beam size onto the temporal axis is the current profile, provided that the intrinsic beam size is small. However, in the SITF the intrinsic beam size was large due to the aforementioned space charge effects. This led to the development of a novel bunch length analysis method in a space charge dominated beam.

In the proposed analysis method, a dispersive section in combination with a TDC was used to visualise the longitudinal phase space. The longitudinal phase space was sliced in the momentum domain to reveal the centre of mass difference between the intrinsic and the streaked beam in a momentum slice. The bunch length could be extracted by recording the centre of masses for all slices. Both the simulations and experiments suggest the method

Abstract

enables the measurement of bunch length in a space charge dominated beam in which the transverse intrinsic beam size is large. The measured minimal bunch length from simulations and experiments are of the same order, 19.5 fs to 24.5 fs, respectively.

The spectral content of femtosecond electron bunches contains electron bunch length information. As an electron beam collides with an optical transition radiation (OTR) foil, radiation is emitted. The radiation is collected by means of a mirror setup into an optical fibre and into an optical spectrometer. The spectral range of the spectrometer is 316 THz (950 nm) to 1364 THz (220 nm). From OTR theory a flat OTR spectrum was expected and measured. As the electron bunch length was reduced below 70 fs, periodic fluctuations started to appear on the spectra. These fluctuations broaden with decreasing bunch length and show a good agreement with the bunch length measured with the TDC.

Key words: SwissFEL, Electron beam diagnostics, Electron bunch length

Contents

Acknowledgements	i
Preface	iii
Zusammenfassung	v
Abstract	vii
List of figures	xiii
List of tables	xix
List of notations	xxi
1 Introduction	1
1.1 SwissFEL	2
1.2 Bunch length measurement at SwissFEL	4
1.3 Aim of the Thesis	5
2 Optical Transition Radiation	7
2.1 The single particle power spectrum	7
2.2 The form factor	12
2.3 Incoherent optical transition radiation	14
2.3.1 The $d\Gamma$ method	16
2.3.2 The correlation theory method	21
2.4 Current dependence	24
2.5 Conclusions	25
3 The SwissFEL Injector Test Facility and Bunch Compression	27
3.1 Theory	27
3.1.1 Linear compression	28
3.1.2 The longitudinal phase space	30
3.1.3 Space charge effects	32
3.2 The SwissFEL Injector Test Facility	33
3.2.1 TDC Setup in the SITF	36
3.3 Simulations of the SITF	37

Contents

3.4	Linear compression in the SITF	39
3.5	Generation of sub-100 fs electron bunches	42
3.5.1	X-band phase to reduce bunch length	42
3.5.2	Scrapers to reduce bunch length	42
3.6	Transverse space charge effects	43
3.7	Conclusions	46
4	Bunch Length Measurement in a Space Charge Dominated Beam Using a Transverse Deflecting Cavity	49
4.1	Concept	49
4.2	Time calibration	51
4.3	Analysis procedure	52
4.4	Simulations	54
4.5	Results	56
4.6	Discussion	61
4.6.1	Bunch length and resolution	61
4.6.2	Advantages and disadvantages	62
4.6.3	Side notes on the measurements, optics	63
4.7	Conclusions	63
5	Measurement of Optical Transition Radiation Spectrum	65
5.1	OTR radiation collection setup	65
5.2	The QE65000 Spectrometer	70
5.2.1	Radiometric calibration	71
5.2.2	Spectrometer resolution	72
5.3	Incoherent and coherent spectra	73
5.3.1	Incoherent radiation	73
5.3.2	Coherent radiation	76
5.4	Conclusions	78
6	Bunch Length Measurement using Spectral Fluctuations	81
6.1	Multiple shot bunch length measurement	82
6.2	Single shot bunch length measurement	84
6.2.1	Single sided compression	84
6.2.2	Compression and over-compression	87
6.3	Conclusions	87
7	Outlook, SwissFEL Implementation	89
7.1	TDC implementation	89
7.2	Spectral implementation	91
8	Conclusions	93
A	Measurement of Fluctuations at the Swiss Light Source	95

B Bunch Length Measurement of Incoherent Spectra at the SwissFEL Injector Test Facility	99
C Hypothesis: Origin of the Spectral Fluctuations	103
D Observation of Interference Patterns from Optical Transition Radiation at the SITF	105
E Spike Removal from Spectra	109
F Software Code to Determine the Bunch Length with the TDC	111
G Software Code to Determine the Bunch Length Using Spectral Fluctuations	113

List of Figures

1.1	Overview of the future SwissFEL.	3
1.2	The temporal structure of a general pump-probe experiment.	4
2.1	The electric field line force in vacuum in the laboratory frame of (a) a free particle at rest, and (b) a relativistic electron.	7
2.2	A schematic of optical transition radiation, amended from [18].	8
2.3	Schematic principle of optical transition radiation, ϵ_1 is the dielectric constant of vacuum, ϵ_2 is the dielectric constant of the foil, E_T is a transverse field sample of the electron, E_{TI} is the transverse image electric field due to the electric field of the electron and v is the velocity of the electron.	9
2.4	Angular distribution of OTR, the angular peak value corresponds to $\frac{1}{\gamma}$, the electron beam energy was 200 MeV/c, $\gamma = 391$	11
2.5	Schematic of an electron bunch radiating (a) coherently and (b) incoherently. .	13
2.6	A schematic to illustrate how bunch length information is stored in the incoherent spectrum of OTR.	15
2.7	An OTR spectrum (a) and (b) the statistical spectral OTR content, which follows a Gamma distribution.	16
2.8	(a) Simulated Gaussian current profile of a 0.1 pC beam with a finite number of particles, the bunch length was 100 fs rms and 50 fs rms, (b) a magnification of the current peak showing the fluctuations, (c) the spectral response and (d) the τ distribution of the 100 fs rms bunch length.	19
2.9	(a) Simulated flat-top current profile of a 0.1 pC beam with a finite number of particles, the bunch length was 100 fs rms and 50 fs rms, (b) the spectral response and (c) the $\sigma_T(\tau)$ distribution of the simulated 100 fs rms bunch length (dots) and the convolution of two flat-tops (solid line).	21
2.10	Bunch length analysis of two Gaussian temporal profiles of 50 fs rms and 100 fs rms, (a) the correlation plot and (b) the correlation width dependence on bunch length.	22
2.11	Bunch length analysis of a flat-top temporal profile of 100 fs FWHM and 200 fs FWHM, (a) the correlation plot and (b) the correlation width dependence on bunch length.	24

List of Figures

2.12	The correlation width dependence on the simulated number of electrons, the error bars represent the standard error of 20 bunches.	25
3.1	Schematic overview of the linear chirp factor A and the uncorrelated energy spread δ	29
3.2	Overview of the SwissFEL Injector Test Facility, divided into six sections. The accelerator structures A1-4 are FINSB01 - 04 and the screens used are C1: F10D1-DSCR75 and 80, C2: F10D100-DSCR10, C3: F10D101-DSCR10 and C4: F10D1-DSCR40.	34
3.3	Schematic of the bunch compressor principle.	35
3.4	Overview of the SwissFEL Injector Test Facility with the accelerator codes used in the indicated sections. Two simulation schemes are shown, I is the simulation scheme using Astra and Elegant and II used Astra and CSRtrack as simulation codes.	37
3.5	The current density in the longitudinal phase space of (a) the experiment and (b) a simulation. Although the compression is variable, the bunch length and momentum space are of the same order. The filamentation seen in the simulation is an artefact due to the limited number of particles.	40
3.6	Observed (a) and simulated (b) longitudinal phase space at camera C3, the simulation was performed with CSRtrack.	40
3.7	Astra and Elegant simulation of the SITE, 20,000 particles, 200 pC.	41
3.8	Simulated longitudinal phase spaces of an X-band accelerator phase scan.	43
3.9	The simulated bunch length versus X-band phase of an Elegant model excluding and including the longitudinal space charge effects.	44
3.10	Simulated current profiles at the shortest bunch length at an X-band phase of 271.25 in Figure 3.9.	44
3.11	Schematic of using the bunch compressor scrapers to reduce bunch length and charge.	45
3.12	Experimental charge density profile of (a) a compressed bunch with scrapers employed and (b) the same plot but the colour scheme amended to visualise the space charge effect.	45
3.13	The transverse charge distribution in a non-dispersive section of a (a) long electron bunch (X-band phase: 270.8 deg., roughly 110 fs rms) and (b) short bunch (X-band phase: 272.8 deg., roughly 25 fs rms). The transverse beam profile blows up as the bunch is compressed.	46
3.14	The transverse beam size as a function of the X-band phase. The minimum bunch length is located at an X-band phase of 273.3 degrees.	46
4.1	High energy spectrometer, schematic depicting unstreaked (intrinsic) beam and the streaked beam, the charge Q , time ΔT , relative energy spread $\Delta\delta$ and the centre of masses $\langle y_{intrinsic} \rangle$ and $\langle y_{streak} \rangle$	50
4.2	Temporal calibration plot of the TDC deflector phase versus the deflection at screen C3 (F10D101).	51

4.3	The measured particle density distribution of a streaked and intrinsic beam at screen C3. All data presented in this section has been taken from this dataset. .	53
4.4	The measured time ΔT versus momentum according to Equation 4.1 and the charge in every slice versus the momentum deviation.	53
4.5	The charge present in every slice versus the time ΔT	54
4.6	The current profile of an electron bunch with different number of bins to illustrate the increase in noise. The data is the same as in Figure 4.5.	54
4.7	Simulation of the high energy spectrometer (a) without and (b) with transverse deflecting cavity.	55
4.8	Simulated time versus momentum and charge versus momentum.	56
4.9	Simulated charge profile	56
4.10	The simulated current profile at the non-dispersive camera C2 and the current profile obtained with the proposed method in the high energy spectrometer, camera C3.	57
4.11	The measured bunch length with the proposed method, using the TDC. Mean and standard error of 10 acquired bunch lengths are presented.	57
4.12	Observed subsequent longitudinal phase space images showing the variability in the charge density on screen C3, disabling us to subtract the intrinsic from the streaked beam.	58
4.13	The measured bunch length with the proposed method, using the TDC. Mean and standard error of 10 acquired bunch lengths. The same data as in Figure 4.11 is used.	59
4.14	The measured bunch length with the proposed method, using the TDC. Mean and standard error of 5 acquired bunch lengths, TDC 0°	60
4.15	The measured bunch length with the proposed method, using the TDC. Mean and standard error of 5 acquired bunch lengths, TDC 180°	60
4.16	Schematic of (a) the longitudinal phase space of a streaked and intrinsic electron beam and (b) a slice from the longitudinal phase space with the time ΔT indicated.	62
5.1	Schematic overview of the SITE. The z positions are relative to the surface of the cathode in the gun.	66
5.2	Systematic overview of the optical part of the spectrometer setup. 1. OTR wafer, 2. Vacuum window, 3. Flat mirror, 4. Off-axis parabolic mirror, 5. Optical fibre, 6. Optical spectrometer, 7. Camera C4. A and B are linear translation stages to focus and align the camera. After the alignment has been verified with the camera, stage B is positioned to focus the beam into the optical fibre.	66
5.3	Photo of the OTR radiation collection setup.	67
5.4	Transmission curve of the silica vacuum window, taken from [51].	68
5.5	Reflectivity curve of the flat mirror and the off-axis parabolic mirror, taken from [52]. No parabolic mirror data was available after 1100 THz.	69
5.6	Off-axis parabolic mirror flatness, analysis wavelength $\lambda = 633$ nm. Courtesy of V. Thominet.	69

List of Figures

5.7	Sensitivity of the ICX204AL CCD sensor [53]. Data was available from 300 THz to 750 THz. The curve does not include the micro-lenses mounted onto the CCD and the anti-reflective window.	70
5.8	OTR photon distribution profile at the entrance of the optical fibre, the dashed circle guides the eye to the entrance size of the optical fibre. The image was taken from an uncompressed 200 pC beam.	70
5.9	The free space part of the optical spectrometer which is enclosed in a box. The grating is installed in a reflective geometry.	71
5.10	Sensitivity of the QE65000 spectrograph. Radiation source: DH 2000.	72
5.11	Spectrometer resolution according to Equation 5.1	73
5.12	Single shot spectrum from an uncompressed bunch, 105 pC.	74
5.13	Spectral intensity versus charge at 600 THz (500 nm) of incoherent spectra for a compressed bunch. The solid and dashed lines guide the eye to a linear fit of the data. The error bars show the standard error. Bunch charge was reduced using scrapers in the bunch compressor.	75
5.14	Single shot spectrum from a compressed bunch.	76
5.15	Charge scan of Optical Transition Radiation at the entrance of the optical fibre. Taken with the camera positioned at Position 7 (Figure 5.2). The analysed spectrometer frequency was 375 THz	77
5.16	Centre of mass of the electron beam versus the X-band phase. The energy loss suggests that CSR is present.	79
6.1	Dataset I. Single shot spectral response of OTR, of two bunch lengths. The bunch length was varied using the X-band phase.	82
6.2	Dataset I. Distribution plot of the intensity at $\nu = 310$ THz, $\Delta\nu = 10$ THz of 500 subsequent spectra.	82
6.3	Dataset I. Multiple shot correlation plot of three set X-band phases, the central frequency was 310 THz, 500 spectra were used to obtain this plot.	83
6.4	Dataset I. Correlation width versus set X-band phase, the error bars are the rms spread of the measurements. The X-band phase is related to bunch length. The star marker represents the correlation width measurement and the dots the bunch length measurements.	84
6.5	Dataset I. Single shot distribution plot. X-band phase is 282.75 deg. $\Delta\nu$ was fixed at 0.3 THz and ν was varied.	85
6.6	Dataset I. Single shot correlation plot of three set X-band phases.	85
6.7	Dataset I. Single shot OTR spectrum from a compressed bunch, detailed view. The third harmonic cavity phase was 282.75 deg. Fluctuations can be seen in the spectrum.	86
6.8	Dataset I. The correlation width versus set X-band phase and the TDC bunch length versus set X-band phase. The circles represent the correlation width measurements, the dots represent the TDC bunch length measurement. The stability of the X-band phase was 0.18 degrees rms.	86

6.9	Dataset II. Correlation width versus set X-band phase (grey dots) and TDC bunch length versus the X-band phase (black stars). The spectral measurement is sensitive below 70 fs rms.	87
7.1	Overview of the SwissFEL with the proposed methods included.	89
7.2	The longitudinal phase space after BC2. Courtesy of B. Beutner.	90
7.3	Current distribution (a, c, e) and frequency response (b, d, f) of the long pulse mode (a,b), the short pulse mode (c, d) and the ultra-short pulse mode (e, f). Data for the current profiles obtained from B. Beutner.	92
A.1	Experimental setup of the fluctuation setup at the SLS.	96
A.2	Photon statistics measurement, in collaboration with Egger. [27].	96
B.1	The QE65000 signal to noise ratio of a varying charge in the accelerator	100
B.2	The QE65000 signal to noise ratio versus the frequency with an electron bunch charge of 130 pC.	100
B.3	The experimental autocorrelation (τ domain) or the temporal profile, the bunch length was varied using the scrapers in the bunch compressor.	101
C.1	(a) Current profile and (b) spectral response of a simulated electron bunch at the position of the optical spectrometer at the SITE	103
D.1	The OTR radiation as coupled into the optical fibre with camera C4 (See Figure 5.1). The images were taken subsequently, an optical density filter with an transmission of 0.01 was mounted in front of the camera to reduce the intensity.	106
D.2	The OTR radiation as coupled into the optical fibre with camera C4 (See Figure 5.1). The images were taken subsequently, an optical bandpass filter of 10 nm FWHM at 633 nm mounted in front of the camera.	107
E.1	Removal of spikes example in an uncompressed bunch.	109

List of Tables

1.1	Key design parameters of the SwissFEL accelerator [9].	3
1.2	Detection methods and their limitations.	5
3.1	The SwissFEL Injector Test Facility main parameters for the high charge mode (200 pC) [41]	36
3.2	Key design parameters of the transverse deflecting cavity [41].	36
3.3	Accelerator code summary, simulating the SITF with relevant parameters. . . .	37
4.1	Arrival time jitter at screen C3. The mean jitter and the standard deviation of the jitter are taken at 5 different TDC phases	52
7.1	Key design parameters of the SwissFEL accelerator according to simulations by B. Beutner. The difference in rms values from chapter 1 originate from the calculation method, all currents below 100 A were set to zero.	89

List of notations

c	Speed of light in vacuum.
d	The diameter.
e	The electric charge of a single electron.
j	The current density.
k	Wave vector.
m	The mass.
p	Momentum of the particle.
r	Distance of the observer and the shape parameter (chapter 2, Gamma distribution).
s	The position of an electron in the bunch.
t	The time.
v	The velocity.
x	Horizontal position, perpendicular to the beam direction.
y	Vertical position, perpendicular to the beam direction.
z	The position along the accelerator.
B	The magnetic flux density or the TDC time calibration factor.
E	The energy of the particle or the electric field.
F	The form factor or the force.
H	The magnetic field strength.
P	The multiple particle power.
W	The single particle power.
β	The Beta function or the relative velocity $\beta = v/c$.
δ	The relative energy spread.
λ	The wavelength or the scale parameter (chapter 2, Gamma distribution) or the density distribution.
ϵ	The dielectric constant.
μ	The magnetic permeability.
γ	The relativistic Lorentz factor.
ω	The radial frequency.
ν	The frequency.
σ	The standard deviation.
R	The beam transfer matrix.
ρ	The radius.

1 Introduction

Many novel ideas and discoveries cannot be credited to one group or person. The discovery that the electron is a particle can be traced back to C.F. Varley in 1871 [1]. The English engineer suggested that the discharge arc, or electricity as he called it, between a negative and positive charged plate were particles of matter. Moreover, the electricity he observed could be directed using magnetic fields as discovered earlier by Plücker in 1858 [2]. Following this experiment the British physicist J.J. Thomson discovered properties of the electron in 1897, following his experiments on cathode rays, earning him the 1906 Nobel Prize in Physics [3, 4]. Similarly to Varley, Thomson deflected electrons with a magnetic field. Thomson however, used free electrons and managed to deflect the electrons in such a way to be able to determine the charge to mass ratio. Although they were not called as such, the aforementioned apparatus were effectively early particle accelerators.

In 1907, Schott predicted the existence of synchrotron radiation, the photon radiation of accelerated particles [5]. This was confirmed in 1945 by J.P. Blewett [6]. Blewett measured the electron energy loss due to synchrotron radiation on the electron beam orbit.

In a synchrotron, relativistic electrons are stored in a ring. In order to confine the electrons to the ring, dipoles and other magnetic elements are needed. Synchrotron radiation is emitted when a charged particle is accelerated. As a convenience, the dipoles accelerate the electron beam transversely and thus generate synchrotron radiation. The use of such a synchrotron has shown and continues to show a great potential for research. The frequency content of synchrotron radiation ranges from zero to the X-ray frequencies. This wide spectrum enables the users of synchrotron radiation to choose the relevant frequency needed for the specific research. Due to the storage of the electrons with relativistic velocities in a ring, the repetition rate of the synchrotron radiation is very large. The synchrotron has two disadvantages. Firstly, the temporal length of the accelerated electron bunches and the resulting radiation is long (tens of picoseconds). This limits the temporal resolution in time resolved measurements. Secondly, synchrotron radiation from bending magnets radiates across a wide frequency spectrum. An exception is the radiation from undulators. This radiation is narrow band, depending on the strength parameter, the resulting spectrum will have higher harmonics from

the fundamental wiggler frequency.

Synchrotron radiation may be used for research, in particular for imaging at small spatial scales. The maximum achievable radiation frequency, or minimum wavelength, of synchrotron radiation depends on the energy of the particle beam and the magnet strength. The smallest imaging resolution achievable is equal to the radiating wavelength, called the diffraction limit. Thus in order to image smaller scales the particle beam must either have a larger beam energy or the synchrotron dipole strength must be increased.

Another method of generating photons is a laser. Since the experimental discovery of the microwave laser in 1955, called a "maser" [7], lasers have contributed greatly to many applications in society. Lasers emit light with a narrow band around a single frequency. Moreover they have been developed to achieve photon pulse lengths much shorter than is possible in synchrotrons. However, the spectrum of lasers spans only from the ultra-violet domain to the infra-red domain due to optics limitations in the resonator. Due to the diffraction limit, the minimum achievable imaging resolution is the ultra-violet wavelength, hence lasers are unsuitable for imaging small scales.

A free electron laser capitalises on the merits of both the laser and the synchrotron. Firstly, the electron bunch length can be very short, resulting in similar short photon pulses. Secondly, since the electrons, used to generate photons, are used once, the electron beam quality after X-ray generation is unimportant. Finally, the radiation from free electron lasers has a very narrow bandwidth, with a high number of photons per unit area. In spectroscopic experiments the narrow bandwidth is important because an increase in bandwidth will introduce blurring. The number of photons per unit area of the photon beam is important because it improves the signal to noise ratio of the user experiment.

1.1 SwissFEL

The SwissFEL (Swiss Free Electron Laser) is a free electron laser which is being built at the Paul Scherrer Institute. The SwissFEL's first operation is foreseen towards the end of 2017.

The SwissFEL will be a user facility to study processes on unexplored scales of space and time, examples can be found in 'Ultrafast Phenomena at the Nanoscale' [8]. In order to achieve these aims the FEL must generate X-ray pulses that are thus ultra-short (tens of femto-seconds) and spatially sufficiently small. Pump probe experiments require such ultra-short X-ray pulses (see Figure 1.2). The temporal resolution of the experiment depends on the X-ray pulse duration t_2 , pulse length jitter of t_2 and arrival time jitter t_1 with respect to the pump event. The design arrival time jitter at the entrance of the undulator is 6.1 fs. The bunch length at the entrance of the undulator for long, short and ultra-short pulses can be obtained from Table 1.1

A free electron laser consists of three major parts, namely the accelerator, the X-ray generation and the experimental endstations. Figure 1.1 gives a schematic overview of the 726 meter

Table 1.1 – Key design parameters of the SwissFEL accelerator [9].

Parameter	Long pulse	Short Pulse	Ultra-short Pulse
Bunch charge (pC)	200	10	10
Initial bunch length at the gun (fs rms)	2600	1574	1574
Bunch length, before undulator (fs rms)	20.7	3.3	0.6
Bunch compression factor	126	477	2623

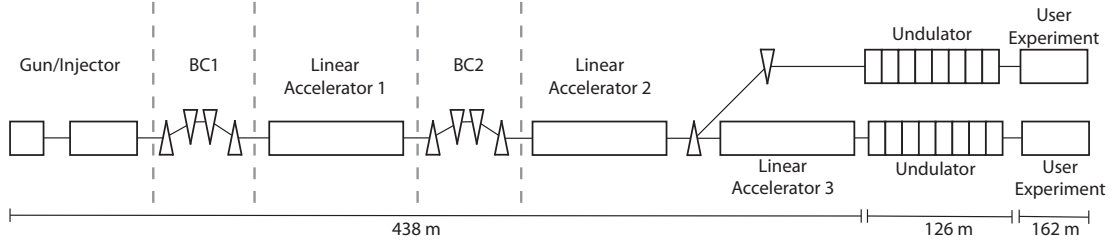


Figure 1.1 – Overview of the future SwissFEL.

SwissFEL. Free electrons are created by illuminating a cathode with a laser. Radio frequency structures accelerate the electron beam. Due to space charge effects the bunch length at the cathode must be on the order of pico-seconds. Two compression stages are installed to compress the electron bunch to femto-second long electron bunches. In an undulator, electrons are traveling through a series of magnets, wiggling the beam and thus generating radiation. The emitted frequency ν , of the photons coming from the undulator depend on the relativistic factor of the electron beam γ , the undulator's period length λ and the undulator parameter K [10].

$$\frac{c}{\nu} = \frac{\lambda}{2\gamma^2} \left(1 + \frac{K^2}{2} \right) \quad (1.1)$$

The frequency of the undulator radiation is proportional to the square of the relativistic factor. High energy electrons are needed to reach sufficiently high frequencies. In the case of the SwissFEL, the energies will range from 2.1 GeV to 5.8 GeV, with resulting frequencies in the range from 0.43 EHz (0.7 nm) to 3 EHz (0.1 nm), depending on the undulator parameters. The emitted radiation is highly polarised with small bandwidth due to the small energy spread. Using mirror optics, the X-ray beam is delivered to the user. Finally, the electron beam is deflected into a beam dump by means of a magnet.

In order to deliver such short X-ray pulses, the electron bunch length, coming from the accelerator, must be comparable to the final X-ray pulse length. In order to achieve such short electron bunch length, the electron bunch length must be monitored at every stage of the compression process. The bunch length at the gun is long and thus different compression stages are foreseen to reach ultra-short bunch lengths. Throughout the accelerator a broad range of bunch length diagnostics ranging from ps to sub fs must be installed.

1.2 Bunch length measurement at SwissFEL

The SwissFEL will require a large range of temporal diagnostics. The final bunch length before the undulator will be between 0.6 fs and 20.7 fs. A range of possible bunch length diagnostic techniques is summarised in Table 1.2.

The first of these methods is the use of electro-optical monitors to measure the electric field of the electron bunch. Electro-optical monitors measure the electric field of the electron bunch. A laser is optically stretched and guided through a polariser to increase the temporal duration as well as correlating the temporal position with wavelength. A birefringent crystal is installed in the beam pipe, close to the electron beam. The birefringent crystal changes the polarisation of the reference laser as the electron beam passes the crystal. The elliptical polarisation after the crystal is converted into an intensity modulation by means of a second polariser. A spectral analyser gives the temporal profile. The bunch length limitation is the birefringent crystal polarisation response. The resolving power is dependent on the excitation of transverse optical lattice vibrations [11].

The Fourier transform of an electron bunch radiating coherently at the observed frequency may also be used to measure bunch length. Extracting bunch length information from Smith Purcell radiation, transition radiation and diffraction radiation relies on the spectral analysis of coherent radiation. Smith Purcell radiation is generated as an electron travels close to a grating. Due to diffraction of the electromagnetic fields around the electron on the grating such as in optical spectrometers, electromagnetic radiation is emitted from the grating. Smith Purcell radiation has the advantage that the frequency emitted is angle dependent. Transition radiation (TR) is generated as a charged particle transverses the boundary between different dielectric constants. Due to the perturbation of the electric fields as the electron transverses the dielectric boundary, electromagnetic radiation is emitted. Diffraction radiation is generated in a similar fashion to transition radiation but features a high frequency cutoff due to a hole in the transition radiation foil. In recording the spectra, the phase of the electromagnetic radiation is lost, resulting in incorrect results. A limited spectral response may also reduce the frequencies that may be recorded with the method. Moreover, the coherent frequency content of ultra-short electron bunches shifts to the $4\text{ }\mu\text{m}$ to $40\text{ }\mu\text{m}$ domain, where filter and detection methods are limited.

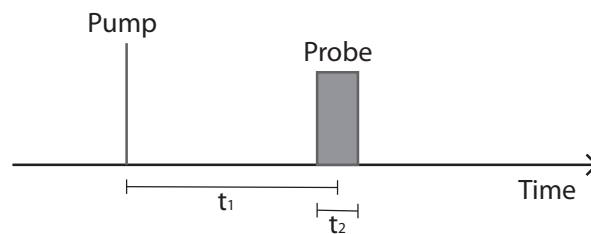


Figure 1.2 – The temporal structure of a general pump-probe experiment.

From Table 1.2 it can be seen that the Transverse Deflecting Cavity (TDC) is capable of measuring the bunch length before the undulator in the Long pulse and Short pulse mode. Despite the fact that the TDC is widely accepted in the free electron laser community as a reliable bunch length measurement, for the shortest bunch lengths in the SwissFEL no measurement has been selected yet. The reason is the costs of such an X-band TDC and the resolution which is not sufficient for the shortest bunches in SwissFEL. The bunch length methods in the table all point to a lower limit. All of the methods share the common feature that measurement becomes more difficult as bunch length is reduced. Conversely, using the method described in this thesis, the measurement becomes easier with shorter bunch length.

Table 1.2 – Detection methods and their limitations.

Method	Destructive	Limit according to reference
Electro optical monitor [11]	No	60 fs fwhm
Coherent Smith Purcell radiation [12]	Yes/no	600 fs fwhm
Coherent diffraction radiation [13]	Yes/no	730 fs rms
Coherent transition radiation [14]	Yes	210 fs fwhm
Transverse deflecting cavity (S-Band) [15]	Yes	27 fs resolution
Transverse deflecting cavity (X-Band) [16]	Yes	1.3 fs resolution

Transition radiation (TR) is used to measure the electron bunch length in this thesis. TR was chosen because of its trivial process and experimental setup. The single particle power spectrum is a flat spectrum over the whole frequency range of the interested domain. Simulations show that as bunch length is reduced, fluctuations appear on the incoherent spectrum. Analysis of the simulated fluctuations shows that the width of these fluctuations depends on the electron bunch length.

The use of spectrometers and detectors that operate in the visible light domain profit from the sensitivity in comparison to THz detectors. In the visible domain, single photon detectors are available and thus it is preferable to measure bunch length in the visible domain rather than in the THz domain if the means are available.

1.3 Aim of the Thesis

The aim of this thesis is to develop and test a method to measure the electron bunch length of femtosecond long electron bunches. We mean to use the aforementioned fluctuations in the visible light domain from optical transition radiation (OTR) and correlate these measurements to a novel bunch length analysis method with the TDC. All experiments were performed at the SwissFEL Injector Test Facility.

The theory chapter (chapter two) describes the OTR theory and the spectral content as a function of bunch length in both the coherent and incoherent spectral domain. This chapter also discusses the two different analysis methods that can be used to extract bunch length

Chapter 1. Introduction

information from OTR spectra. The third chapter describes the theory needed to understand the bunch compression in linear accelerators and introduces the SwissFEL Injector Test Facility (SITF). The effects of high compression on an accelerator beam will be described with reference to experimental results and to theoretical and numerical simulations. Because the SITF was not built for femto-second electron bunches, the standard TDC bunch length measurement tools could not be used. The fourth chapter introduces a novel analysis method, which uses the TDC in combination with the high energy spectrometer to measure the electron bunch length.

The fifth chapter describes the OTR radiation collection setup and characterises the components used in the setup. The chapter also characterises incoherent and coherent spectra. The results of the OTR spectral content as a function of bunch length are described in chapter six. Finally the outlook and conclusions are presented in the final two chapters.

2 Optical Transition Radiation

Transition radiation is emitted as a relativistic charge passes a boundary surface between two different dielectric constants, for example from vacuum to aluminum foil. As a relativistic electron beam passes close to or through a metallic foil, electric fields are perturbed due to the foil resulting in the emission of electromagnetic radiation. The power spectrum of Optical Transition Radiation (OTR) of an infinitely large foil and infinitely small plasma frequency spans over the whole frequency domain (see e.g. [17–19]).

This chapter describes the emission of OTR and its dependencies. In particular the chapter will focus on the incoherent domain and the bunch length information that may be stored in the OTR spectra.

2.1 The single particle power spectrum

The single particle power spectrum is defined as the energy per unit frequency per unit time. In this section the single particle power spectrum is deduced for OTR in the case of an electron colliding with a foil which is located perpendicular to the direction of travel of the electron. In this section the OTR power dependence on frequency is derived.



Figure 2.1 – The electric field line force in vacuum in the laboratory frame of (a) a free particle at rest, and (b) a relativistic electron.

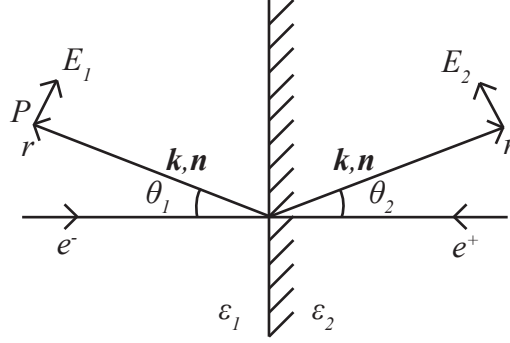


Figure 2.2 – A schematic of optical transition radiation, amended from [18].

In order to clarify the symbols used in the theoretical calculations a schematic diagram is presented in Figure 2.2. The model assumes that an electron travels in the z direction and encounters a foil with dielectric constant ϵ_2 at time $t = 0$. Similarly an image charge travels in the opposite direction and encounters the vacuum with dielectric constant ϵ_1 at exactly the same time. The electron and image charge travel both with velocity v . If the velocity of the particle is close to the speed of light in vacuum, the electric fields are mainly orientated perpendicular to the direction of travel, as shown in Figure 2.1 (b). The ratio of the transverse field over the longitudinal field is proportional to the relativistic factor $E_T/E_L \propto \gamma$. The foil is an ideal conductor with a dielectric constant $\epsilon_2 \gg 1$ in which the potential over the foil is constant. The electric field arising from such a potential in the conductor favours an electric field perpendicular to the surface.

A stepwise schematic of Figure 2.2 is shown in Figure 2.3 (a). As the relativistic charge transverses the metallic foil (see Figure 2.3 b), the transverse electric field is superimposed onto the foil. In order to equilibrate the electric field in the foil, as it was before the charge entered the conductor, an image electric field E_{TI} is created in the opposite direction of E_T . As the electron moves into the foil with dielectric constant ϵ_2 , (see Figure 2.3 c), the electric field coming from the charge disappears and the foil is left with the image electric field component. In order to restore the original electric field onto the foil, the foil needs to return to its equilibrium state. In doing so, electromagnetic radiation is emitted.

Optical transition radiation is emitted with an angle of θ (see Figure 2.2) with respect to the electron path and directed towards the observer P . The wave vector \mathbf{k} is the momentum of the photon given by $\mathbf{k} = \omega/c\sqrt{\epsilon}\mathbf{n}$ where \mathbf{n} is a vector giving the direction of the emission.

The theory presented has been taken from several authors [19–22]. In order to define the single particle spectrum from optical transition radiation, the electric or magnetic field must be defined for an electron in vacuum. The magnetic field \mathbf{H} at an observation point P , a large

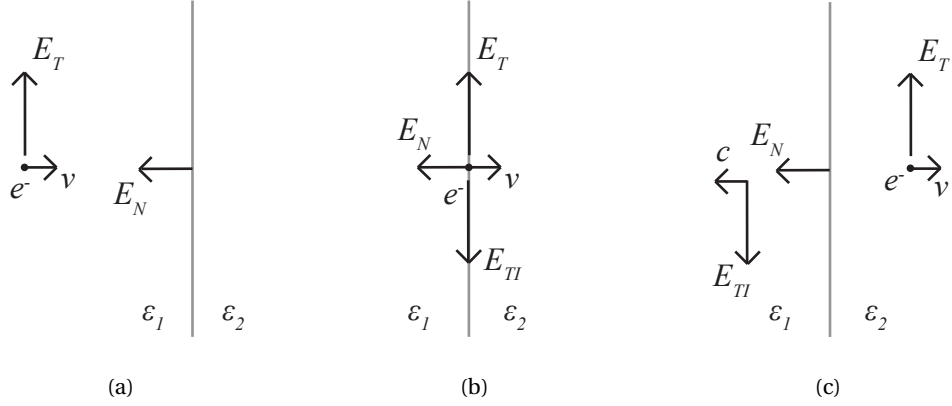


Figure 2.3 – Schematic principle of optical transition radiation, ϵ_1 is the dielectric constant of vacuum, ϵ_2 is the dielectric constant of the foil, E_T is a transverse field sample of the electron, E_{TI} is the transverse image electric field due to the electric field of the electron and v is the velocity of the electron.

distance \mathbf{r} from the point charge, may be defined as a function of \mathbf{r} and the radial frequency ω :

$$\mathbf{H}(\mathbf{r}, \omega) = \frac{i e^{i k r}}{4 \pi \sqrt{\mu_0 \epsilon_0} c r} \int' [\mathbf{j}(\mathbf{r}', \omega)] e^{-i \mathbf{k} \mathbf{r}'} d r', \quad (2.1)$$

where c is the speed of light in vacuum and \mathbf{j} is the current density. The radiation energy per observation angle $d\Omega$ may be described with:

$$\frac{dW(\mathbf{n})}{d\Omega} = 4 \pi \sqrt{\mu_0 \epsilon_0} c r^2 \int_0^\infty [\mathbf{E}(\mathbf{r}, \omega) \mathbf{H}(\mathbf{r}, \omega)] d\omega. \quad (2.2)$$

With the Coulomb gauge, Gauss' law reduces to $\nabla \cdot \epsilon \mathbf{E} = 0$, in which the permeability is $\epsilon = 1$ for vacuum. Combining Gauss' law for magnetism ($\nabla \cdot \mathbf{B} = 0$) and the reduced Gauss' law as aforementioned, the electric field is:

$$\mathbf{E}(\mathbf{r}, \omega) = \sqrt{\frac{\mu_0}{\epsilon_0}} \mathbf{H}(\mathbf{r}, \omega), \quad (2.3)$$

insertion into Equation 2.2 gives:

$$\frac{dW(\mathbf{n})}{d\Omega} = 4 \pi \mu_0 c r^2 \int_0^\infty |\mathbf{H}(\mathbf{r}, \omega)|^2 d\omega. \quad (2.4)$$

Chapter 2. Optical Transition Radiation

Performing a differentiation over ω gives:

$$\frac{dW^2(\mathbf{n}, \omega)}{d\Omega d\omega} = 4\pi\mu_0 c r^2 |\mathbf{H}(\mathbf{r}, \omega)|^2. \quad (2.5)$$

Substituting the defined magnetic field (Equation 2.1) into Equation 2.5 with $\mathbf{k} = \omega/c\sqrt{\epsilon}\mathbf{n}$, $|ie^{ikr}| = 1$ and $\epsilon = 1$ gives:

$$\frac{dW^2(\mathbf{n}, \omega)}{d\Omega d\omega} = \frac{\omega^2}{4\pi\epsilon_0 c^3} \left| \int' [\mathbf{n}\mathbf{j}(\mathbf{r}', \omega)] e^{-i\mathbf{k}\mathbf{r}'} dr \right|^2. \quad (2.6)$$

At times $t < 0$ the electron and the image charge travel towards each other. At $t = 0$ the electron and image charge meet exactly at the surface of the foil. The current density can be described with delta functions since we have a single point charge.

$$\mathbf{j}(\mathbf{r}, t) = e\mathbf{v}\sqrt{4\pi\epsilon_0}[\delta(\mathbf{r} - \mathbf{v}t) + \delta(\mathbf{r} + \mathbf{v}t)] \text{ with } t < 0 \text{ and } \mathbf{j}(\mathbf{r}, t) = 0 \text{ with } t > 0 \quad (2.7)$$

The Fourier transform of the current density at $t < 0$ becomes:

$$\mathbf{j}(\mathbf{r}, \omega) = \frac{e\mathbf{v}\sqrt{4\pi\epsilon_0}}{2\pi} \int [\delta(\mathbf{r} - \mathbf{v}t) + \delta(\mathbf{r} + \mathbf{v}t)] e^{i\omega t} dt. \quad (2.8)$$

Inserting Equation 2.8 into Equation 2.6 gives:

$$\frac{dW^2(\mathbf{n}, \omega)}{d\Omega d\omega} = \frac{e^2 \omega^2}{4\pi^2 c^3} (\mathbf{n} \times \mathbf{v})^2 \left| \int \left[\int [\delta(\mathbf{r} - \mathbf{v}t) + \delta(\mathbf{r} + \mathbf{v}t)] e^{i\omega t} dt \right] e^{-i\mathbf{k}\mathbf{r}'} dr \right|^2. \quad (2.9)$$

The integral over the distance r is calculated. The distance of observation must be larger than the inverse frequency, or wavelength, of observation, thus $r \gg c/\omega$. With $\int \delta(\mathbf{r} - \mathbf{v}t) e^{-i\mathbf{k}\mathbf{r}} = e^{-i\mathbf{k}\mathbf{v}t}$ Equation 2.9 becomes:

$$\frac{dW^2(\mathbf{n}, \omega)}{d\Omega d\omega} = \frac{e^2 \omega^2}{4\pi^2 c^3} (\mathbf{n} \times \mathbf{v})^2 \left| \int_{-\infty}^0 [e^{i(\omega - \mathbf{k}\mathbf{v})t} + e^{i(\omega + \mathbf{k}\mathbf{v})t}] dt \right|^2. \quad (2.10)$$

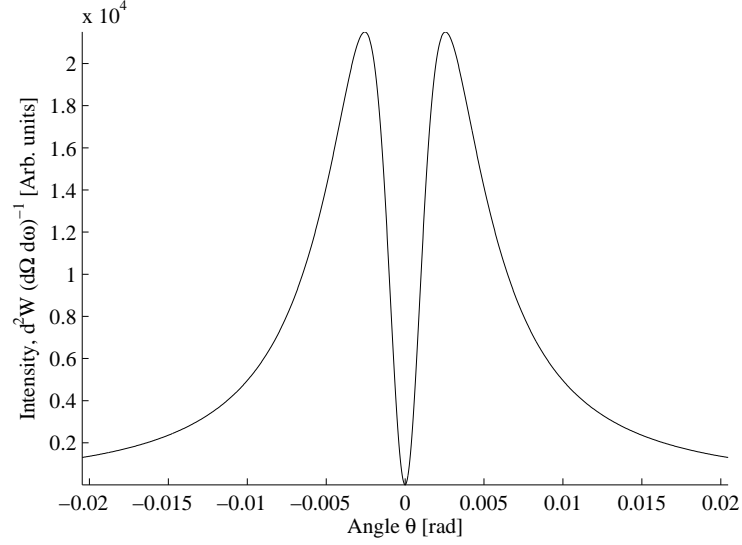


Figure 2.4 – Angular distribution of OTR, the angular peak value corresponds to $\frac{1}{\gamma}$, the electron beam energy was 200 MeV/c, $\gamma = 391$.

As a result of the assignment of the charge and image charge, the integral over time is calculated from minus infinity to zero at which point the electron and image charge meet.

$$\frac{dW^2(\mathbf{n}, \omega)}{d\Omega d\omega} = \frac{e^2 \omega^2}{4\pi^2 c^3} (\mathbf{n} \times \mathbf{v})^2 \left| \frac{1}{(\omega - \mathbf{k}\mathbf{v})} + \frac{1}{(\omega + \mathbf{k}\mathbf{v})} \right|^2. \quad (2.11)$$

The equation above can be reduced using $\mathbf{k} = \frac{\omega}{c} \mathbf{n}$, $\mathbf{n}\mathbf{v} = v \cos \theta$, $\mathbf{n} \times \mathbf{v} = v \sin \theta$ and $\beta = \frac{v}{c}$.

$$\frac{dW^2(\mathbf{n}, \omega)}{d\Omega d\omega} = \frac{e^2 \beta^2}{\pi^2 c} \frac{\sin^2 \theta}{(1 - \beta^2 \cos^2 \theta)^2}. \quad (2.12)$$

Figure 2.4 shows the angular distribution of optical transition radiation according to Equation 2.12. The figure shows that optical transition radiation has a maximum at the angle of $1/\gamma$. The polarisation of the electric field is pointing radially outward. Integration over the angle Ω gives:

$$\frac{dW(\omega)}{d\omega} = \frac{e^2}{\pi c} \left(\frac{1 + \beta^2}{2\beta} \ln \frac{1 + \beta}{1 - \beta} - 1 \right). \quad (2.13)$$

In the relativistic case in which $\gamma \gg 1$, the optical transition radiation intensity has a natural

logarithmic dependence on the particle energy. The above equation may be simplified to:

$$\frac{dW}{d\omega} \approx \frac{e^2}{\pi c} \ln \gamma. \quad (2.14)$$

The radiated energy of a single point charge as shown in Equation 2.14 has no dependence on frequency. Theoretically the single particle power spectrum spreads from zero to infinity. In practice, a low and high frequency cutoff arises due to the screen size and the plasma frequency of the foil, respectively. The radial plasma frequency ω is defined as [23]:

$$\omega = \sqrt{\frac{n_e e^2}{m \epsilon_0}}. \quad (2.15)$$

In which n_e is the number of electrons per unit area, e is the electric charge, m is the mass of an electron and ϵ_0 is the vacuum permittivity. The plasma frequency of aluminium is roughly 162 PHz (1.85 nm). The low frequency cutoff ν_{cutoff} is due to the size of the OTR foil.

$$\nu_{cutoff} = \frac{\gamma c}{2\pi d}, \quad (2.16)$$

where γ is the relativistic factor, c the speed of light in vacuum and d the diameter of the transition radiation foil. The low frequency cutoff is roughly 0.93 THz (0.32 mm) for the momentum of 200 MeV/c and a hole diameter of 2 cm. The visible light domain is well away from these limits.

2.2 The form factor

The electron bunch is observed to radiate coherently if the observed wavelength is much longer than the electron bunch length. Similarly, if the observed radiation wavelength is much shorter than the electron bunch length the observed radiation is incoherent. Figure 2.5 shows a schematic of three electrons radiating coherently and incoherently. The transition between the observed wavelength radiating incoherently or coherently is given by the form factor. In order to derive the form factor and its dependencies on the measured spectral intensities, a number of N particles is present in the electron bunch. The total electric field $\mathbf{E}(t)$ is the sum of the single particle electric fields [24]:



Figure 2.5 – Schematic of an electron bunch radiating (a) coherently and (b) incoherently.

$$\mathbf{E}(t) = \sum_{k=1}^N \mathbf{e}(t - t_k), \quad (2.17)$$

where $\mathbf{e}(t)$ is the electric field of a single electron, N the number of particles and t_k the random arrival time of the k^{th} particle. The total radiated power is proportional to the square of the electric field and may be described with $dP(\omega)/d\omega \propto |E(\omega)|^2$, and hence:

$$\frac{dP(\omega)}{d\omega} = \frac{dW}{d\omega} \left| \sum_{k=1}^N e^{i\omega t_k} \right|^2 \quad (2.18)$$

$$= \frac{dW}{d\omega} \sum_{k=1}^N e^{i\omega t_k} \sum_{l=1}^N e^{-i\omega t_l} = \frac{dW}{d\omega} \sum_{k,l=1}^N e^{i\omega(t_k - t_l)} \quad (2.19)$$

$$= \frac{dW}{d\omega} \left[\sum_{k=l}^N e^{i\omega(t_k - t_l)} + \sum_{k,l=1(k \neq l)}^N e^{i\omega t_k} e^{-i\omega t_l} \right] \quad (2.20)$$

$$= \frac{dW}{d\omega} \left[N + \sum_{k,l=1(k \neq l)}^N e^{i\omega(t_k - t_l)} \right] \quad (2.21)$$

$$= \frac{dW}{d\omega} [N + (N^2 - N)F(\omega)] \quad (2.22)$$

Where the form factor is defined as:

$$F(\omega) = \frac{1}{N(N-1)} \sum_{k,l=1(k \neq l)}^N e^{i\omega(t_k - t_l)}. \quad (2.23)$$

If no coherence is present at the wavelength of observation, $F(\omega)$ amounts to zero and the radiated power is linearly proportional to the number of electrons. If the observed wavelength is fully coherent, $F(\omega)$ becomes one and the radiated power is proportional to the square of the number of electrons. The above equations are valid for any particle distribution.

To find a continuous expression for the form factor, assumptions must be made. Firstly the average of the particle distribution is taken such that the fluctuations on the general profile

are lost. In this derivation it is assumed that the incoherent radiation does not contain bunch length information and that the observed wavelength is larger than the temporal fluctuations on the profile $\omega\sigma_b \gg 1$. Secondly, the number of particles is large such that $N^2 - N \approx N^2$. Finally, the individual particles are replaced by a continuous distribution, in Equation 2.23 the sum is replaced by an integral. The resulting form factor is the Fourier transform of the continuous temporal electron bunch distribution $f(t)$ [24].

$$F(\omega) = \left| \int_{-\infty}^{\infty} f(t) e^{-i\omega t} dt \right|. \quad (2.24)$$

Thus in order to retrieve the bunch length and distribution a spectroscopic analysis is required. By measuring the power spectrum $dP/d\omega$, Equation 2.22 may be used to calculate the form factor, given that the charge is known. Explicit knowledge of the single particle energy distribution $dW/d\omega$ is not needed in the case of transition radiation because of the independence of the OTR intensity on frequency. Upon Fourier transforming the form factor, the bunch length as well as the bunch shape may be retrieved using Equation 2.24. It should be noted that detectors record only the absolute power and not the phase, leading to incorrect results. Efforts have been made to retrieve the phase using the Kramers-Kronig relations, examples of the non-trivial method can be found in [25, 26].

2.3 Incoherent optical transition radiation

From the previous section it was concluded that the coherent domain in OTR spectra contains bunch length information. It can be shown that the incoherent OTR spectrum contains bunch length information too.

In the following an electron bunch travelling with a finite velocity onto an OTR foil is assumed. The temporal electron bunch profile can be divided into a deterministic process and a stochastic process. The deterministic process varies on the order of the bunch length. The stochastic process is a random process due to the finite number of particles. Therefore the temporal profile $p(t)$ is the multiplication of the stochastic process $s(t)$ with the deterministic process $d(t)$:

$$p(t) = s(t) \cdot d(t). \quad (2.25)$$

A multiplication in the time domain is a convolution in the frequency domain. The same

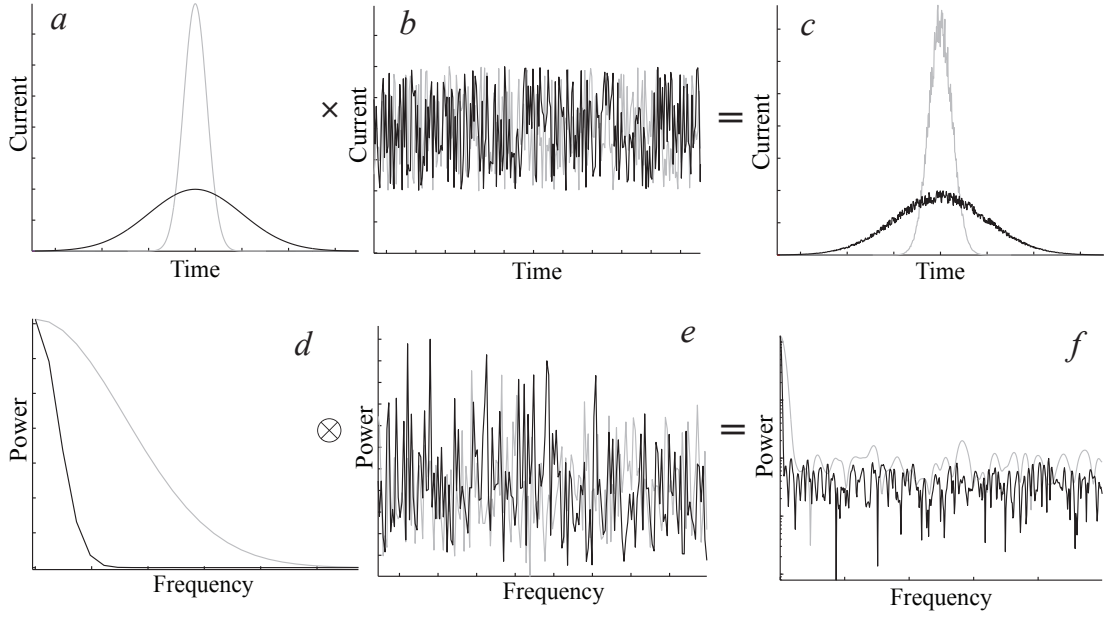


Figure 2.6 – A schematic to illustrate how bunch length information is stored in the incoherent spectrum of OTR.

process in the frequency domain becomes:

$$P(\omega) = S(\omega) \otimes D(\omega). \quad (2.26)$$

For simplicity two Gaussian beams are chosen with two different bunch lengths. Figure 2.6 *a* shows two deterministic processes. The stochastic process in Figure 2.6 *b* shows the same random process for both bunch lengths. Due to the multiplication in the time domain, the resulting profile (Figure 2.6 *c*) features fluctuations on top of the deterministic process. The fluctuations are due to the finite number of electrons and scale with \sqrt{N} . Figure 2.6 *d-f* shows the Fourier transform of the individual processes. Thus *d* is the Fourier transform of *a*, *e* is the Fourier transform of *b* and *f* is the Fourier transform of *c*. Either performing the Fourier transforms separately or convoluting *d* and *e* gives the same result, i.e. Figure 2.6 *f*. Figure 2.6 *f* is plotted on a logarithmic scale, in contrast to the other plots which are plotted with a linear scale. In the low frequency domain, the coherent domain stretches further into higher frequencies as the bunch length is reduced. However in the incoherent domain, fluctuations are observed which are dependent on the bunch length. The light grey curve comes from the shorter bunch and shows less fluctuations than the black curve which comes from the longer bunch length. The resulting dependence on bunch length comes from the convolution of the statistical noise with the Gaussian Fourier response of the temporal profile.

The emission of OTR follows Poisson statistics [27]. The detected intensities in the frequency

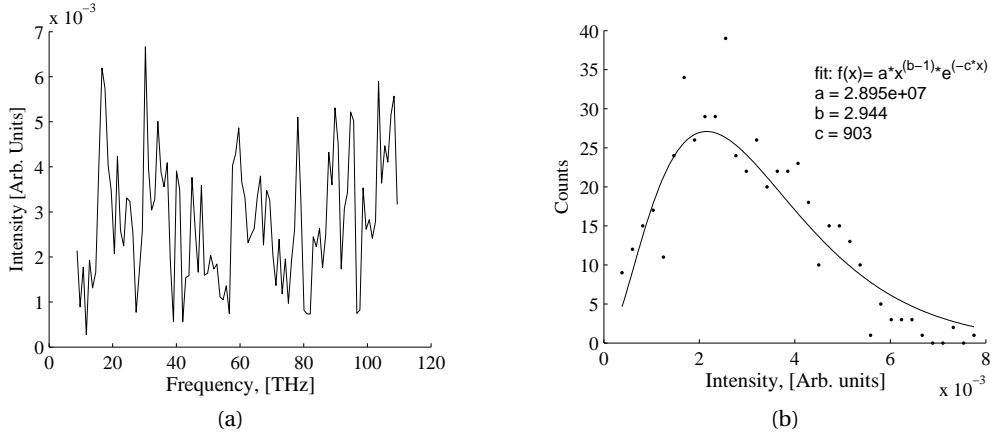


Figure 2.7 – An OTR spectrum (a) and (b) the statistical spectral OTR content, which follows a Gamma distribution.

bins $\Delta\nu$ can be binned in a histogram, which is expected to follow a Gamma distribution:

$$f(x) = \frac{\lambda^r x^{r-1} e^{-\lambda x}}{\Gamma(r)}, \quad (2.27)$$

where the Gamma function given by $\Gamma(r) = \int_0^\infty x^{r-1} e^{-x} dx$. λ and r are the scale and shape parameters respectively. Figure 2.6 (c) displays a plot of the temporal fluctuations. Performing a Fourier transform on this data, the plot of Figure 2.7 (a) is obtained. In the plot the coherent domain has been removed to draw attention to the incoherent spectrum. The histogram in Figure 2.7 (b) shows the binned intensities from the incoherent spectrum. The data is fitted to a Gamma distribution.

The resulting Gamma distribution is independent on bunch length and thus another quantity must be presented that does depend on bunch length. In the upcoming sections two analysis methods are presented and justified with simulations to quantify the incoherent spectrum fluctuations to the bunch length.

2.3.1 The $d\Gamma$ method

It can be shown that the variability of the Fourier transform of the incoherent transition radiation spectrum contains bunch length information. The derivation of Egger [27] was followed but others are available [28–30].

Theory

Let $dP(\omega)/d\omega$ be the measured spectrum, the autocorrelation function of the temporal distribution is $\Gamma_n(\tau)$:

$$\Gamma(\tau) = \int_{-\infty}^{\infty} \frac{dP(\omega)}{d\omega} e^{-i\omega\tau} d\omega. \quad (2.28)$$

Following Equation 2.18 the average of the autocorrelation becomes:

$$\langle \Gamma_n(\tau) \rangle = \int_{-\infty}^{\infty} \left| \frac{dW(\omega)}{d\omega} \right|^2 \sum_{k,l=1}^N e^{i\omega(t_k-t_l)} e^{-i\omega\tau} d\omega. \quad (2.29)$$

In the last section it was assumed that the bunch length multiplied by the frequency was much larger than one, i.e. $\omega\sigma_b \gg 1$. In the upcoming derivation it is assumed that no coherence occurs in the spectrum. The standard derivation of the autocorrelation function is:

$$\sigma_{\Gamma}(\tau) = \langle |\Gamma_n(\tau)|^2 \rangle_n - |\langle \Gamma_n(\tau) \rangle_n|^2. \quad (2.30)$$

The summation in Equation 2.29 can be rewritten as [27, 28]:

$$\left\langle \sum_{k,j,m,l=1}^N e^{i\omega(t_k-t_l)} e^{i\omega(t_j-t_m)} \right\rangle = N^2 (1 + |f_b(\omega_1 - \omega_2)|^2). \quad (2.31)$$

The first term in Equation 2.30 becomes:

$$\langle |\Gamma_n(\tau)|^2 \rangle_n = \int_{-\infty}^{\infty} \left| \frac{dW(\omega_1)}{d\omega} \right|^2 \left| \frac{dW(\omega_2)}{d\omega} \right|^2 \times N^2 (1 + |f_b(\omega_1 - \omega_2)|^2) e^{-i(\omega_1 - \omega_2)\tau} d\omega_1 d\omega_2. \quad (2.32)$$

The second term in Equation 2.30 becomes:

$$|\langle \Gamma_n(\tau) \rangle_n|^2 = \int_{-\infty}^{\infty} \left| \frac{dW(\omega_1)}{d\omega} \right|^2 \left| \frac{dW(\omega_2)}{d\omega} \right|^2 \times N^2 e^{-i(\omega_1 - \omega_2)\tau} d\omega_1 d\omega_2. \quad (2.33)$$

Chapter 2. Optical Transition Radiation

Substituting Equation 2.32 and 2.33 into Equation 2.30 gives:

$$\sigma_{\Gamma}(\tau) = N^2 \int_{-\infty}^{\infty} \left| \frac{dW(\omega_1)}{d\omega} \right|^2 \left| \frac{dW(\omega_2)}{d\omega} \right|^2 \times (|f_b(\omega_1 - \omega_2)|^2) e^{-i(\omega_1 - \omega_2)\tau} d\omega_1 d\omega_2, \quad (2.34)$$

with $\omega_1 = \Delta\omega + \omega_2$ the fluctuations become:

$$\sigma_{\Gamma}(\tau) = N^2 \int_{-\infty}^{\infty} \left| \frac{dW(\Delta\omega + \omega_2)}{d\omega} \right|^2 \left| \frac{dW(\omega_2)}{d\omega} \right|^2 \times (|f_b(\Delta\omega)|^2) e^{-i(\Delta\omega)\tau} d\Delta\omega d\omega_2. \quad (2.35)$$

The electric field terms with ω_2 and $\omega_2 + \Delta\omega$ are deterministic processes whereas the electric field terms with $\Delta\omega$ are stochastic processes and vary quickly over time. If $\Delta\omega$ approaches zero, the saddle point approximation gives:

$$\sigma_{\Gamma}(\tau) = N^2 \int_{-\infty}^{\infty} \left| \frac{dW((\Delta\omega_0 + \omega_2))}{d\omega} \right|^2 \left| \frac{dW(\omega_2)}{d\omega} \right|^2 d\omega_2 \times \int_{-\infty}^{\infty} |f_b(\Delta\omega)|^2 e^{-i(\Delta\omega)\tau} d\Delta\omega. \quad (2.36)$$

In this last step we assume that the integration over ω_2 is a constant and can be denoted as κ . The Wiener Khinchin integral is defined as: $E[x(t)x^*(t - \tau)] = \int_{-\infty}^{\infty} e^{2\pi i f \tau} dF(f)$. Applying the Wiener-Khinchin theorem to the integral over $\Delta\omega$ gives:

$$\sigma_{\Gamma}(\tau) = \kappa \times \int_{-\infty}^{\infty} f_b(t) f_b(t - \tau) dt. \quad (2.37)$$

The fluctuations $\sigma_{\Gamma}(\tau)$ are equal to the autocorrelation of the temporal profile. Multiple spectral measurements are needed in order to measure the fluctuations around $\Gamma(\tau)$.

Gaussian Bunch simulations

The temporal profile and its Fourier transform are shown in Figure 2.8 a and c, the data in plot b shows an enlargement of the peak with the temporal fluctuations superimposed on the temporal profile. Temporal Gaussian shaped bunches with standard deviations of 100 fs and 50 fs were filled with single electrons up to an equivalent bunch charge of 0.1 pC. The electrons were binned such that the bin size was well below the Nyquist frequency. In Matlab the Fast Fourier Transform (FFT) was used to calculate the simulated diagnosed spectrum. To calculate the $\Gamma(\tau)$ domain, the diagnosed power spectrum was trimmed such that no coherence was present. The fluctuations in the τ domain were calculated using Equation 2.30. 100 spectra

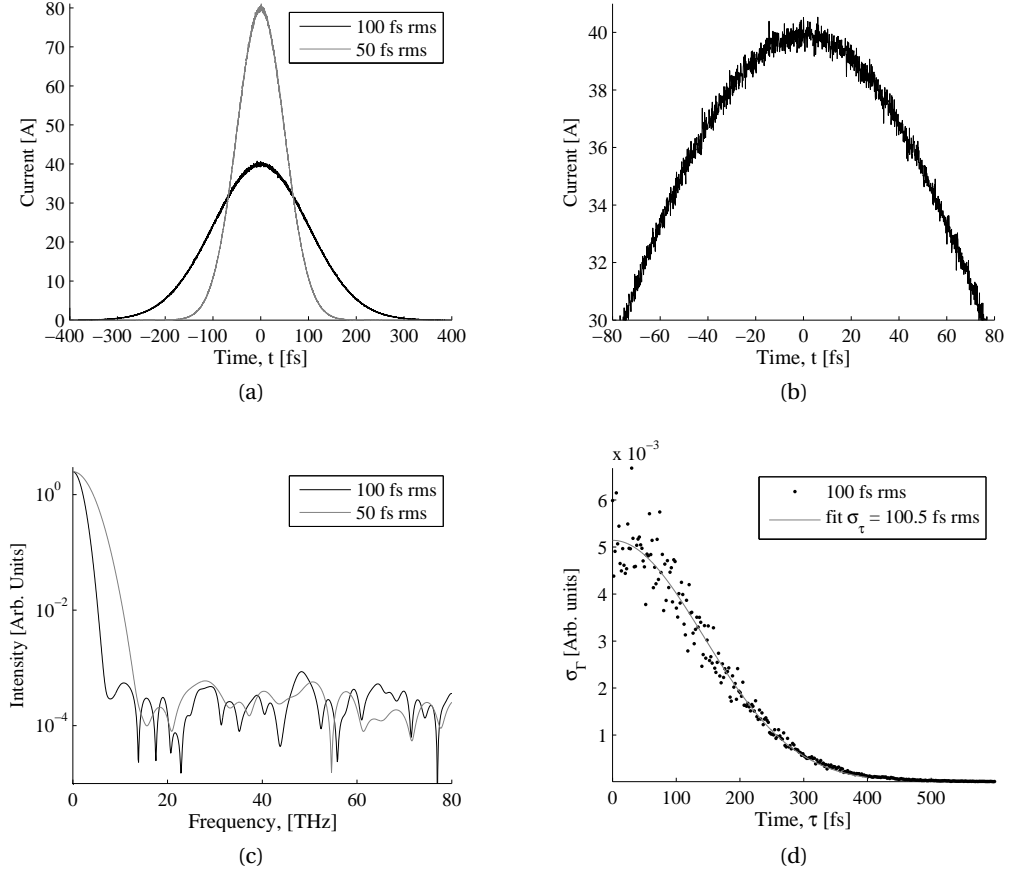


Figure 2.8 – (a) Simulated Gaussian current profile of a 0.1 pC beam with a finite number of particles, the bunch length was 100 fs rms and 50 fs rms, (b) a magnification of the current peak showing the fluctuations, (c) the spectral response and (d) the τ distribution of the 100 fs rms bunch length.

were used for the σ_τ calculation.

Figure 2.8 d shows the result of the $\Gamma(\tau)$ method. The simulated data was fitted to a Gaussian in the form:

$$\sigma_\Gamma(\tau) \propto e^{-\frac{\tau^2}{4\sigma^2}}. \quad (2.38)$$

The fitted sigma was $100.5 \text{ fs} \pm 0.4 \text{ fs}$, where the original Gaussian bunch had a standard deviation of 100 fs.

Flat-top simulations

Electron beams can often not be treated as Gaussian bunches. Particularly electron bunches in the SITF are non-Gaussian under strong longitudinal compression. Other longitudinal bunch profiles may thus be possible, such as a skewed Gaussian or a flat top. Figure 2.9 (a) shows such a flat top beam profile with a finite number of electrons. A uniform electron bunch was created in the time domain and binned. Because an ideal step function will generate a coherent domain that stretches into the visible domain, the hard edges are smoothed out. The uniformly filled profile is multiplied by a super-Gaussian of the form:

$$f(t) = e^{\frac{-t^M}{2\sigma^M}}, \quad (2.39)$$

where $\sigma = \text{FWHM}/2$ and M defines the sharpness of the edges, where a larger M gives sharper edges. For the simulations presented in this section, an M of 16 was chosen.

The Fourier transform is shown in Figure 2.9 (b). As can be seen the coherent domain stretches further into higher frequencies. The coherent domain shows a periodic modulation due to the remaining flat-top. As the bunch length is reduced the width of these periods increase. It can also be seen that the incoherent domain still retains the fluctuations.

The fluctuations were analysed on bunch length dependence by Fourier transforming to the τ domain and calculating the fluctuations. The data in Figure 2.9 c shows the simulated $\Gamma(\tau)$ distribution. The simulated data may be compared to the convolution of the two flat-tops, which is shown in the Figure as a solid line. Theoretically, convoluting two perfect flat-tops generates triangle shaped curve, however, due to the smoothened edges of the flat-top the edges of the convolution are also smoothened out. Both the convoluted data and the data calculated using the $d\Gamma(\tau)$ method agree well, thus proving numerically that the method works and the bunch shape may be deduced using the $d\Gamma(\tau)$ method.

Conclusions

The $d\Gamma(\tau)$ method can be used to obtain the bunch length information. The drawback of the method is that multiple shots are needed to deduce a temporal profile. The advantage is that the shape of the electron bunch may be deduced, which was proven with a Gaussian bunch and a flat top bunch. Although the shape of the electron bunch may be determined, the orientation of the electron bunch is unclear. The resolution of the bunch length measurement depends mainly on the spectral range of the optical spectrometer. It can be easily seen that if the spectral domain becomes larger, the Fourier transform will have smaller time steps in the τ domain. On the other hand the spectrometer resolution determines the resulting temporal range and thus it should be set as small as possible.

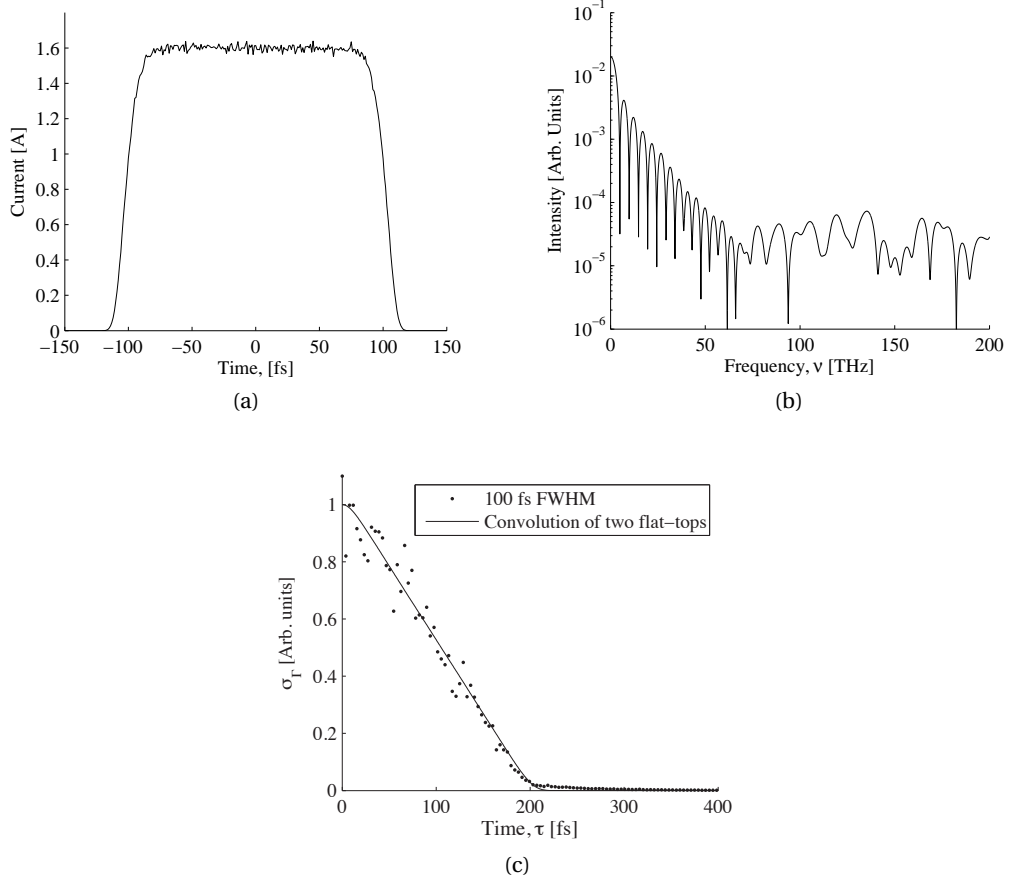


Figure 2.9 – (a) Simulated flat-top current profile of a 0.1 pC beam with a finite number of particles, the bunch length was 100 fs rms and 50 fs rms, (b) the spectral response and (c) the $\sigma_{\Gamma}(\tau)$ distribution of the simulated 100 fs rms bunch length (dots) and the convolution of two flat-tops (solid line).

2.3.2 The correlation theory method

Correlation theory has previously been used to measure bunch length [31, 32]. The method quantifies the correlation of two variables to each other. In this work, first order correlation theory has been applied.

Theory

The first order correlation may be described by the covariance Σ which is the linear relationship between two scalar variables X and Y [33, 34]:

$$\Sigma_{X,Y} = \langle (X - \langle X \rangle)(Y - \langle Y \rangle) \rangle = \langle XY \rangle - \langle X \rangle \langle Y \rangle. \quad (2.40)$$

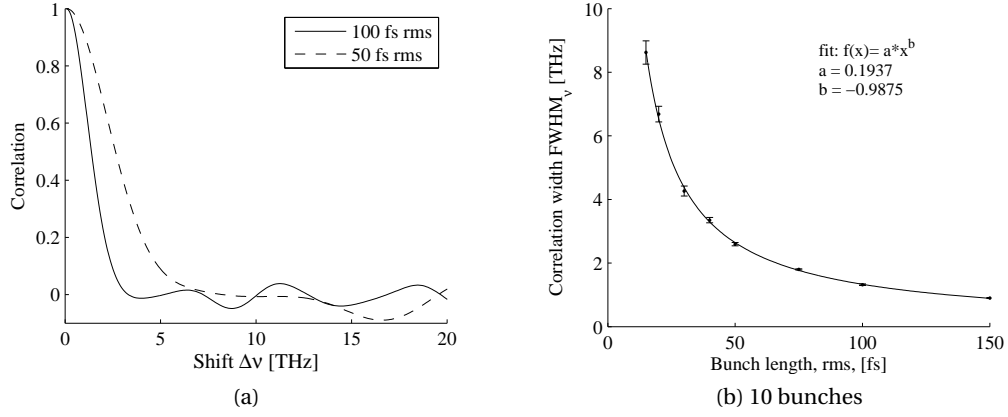


Figure 2.10 – Bunch length analysis of two Gaussian temporal profiles of 50 fs rms and 100 fs rms, (a) the correlation plot and (b) the correlation width dependence on bunch length.

In which $\langle X \rangle$ is the average of a one dimensional array X . The correlation is the covariance divided by a normalisation factor,

$$C = \frac{\Sigma_{XY}}{\sigma_X \sigma_Y}. \quad (2.41)$$

In which $\sigma_X \sigma_Y$ are the root mean squares defined as $\sqrt{\langle (X - \langle X \rangle)^2 \rangle}$ of the variables X and Y . The correlation is dimensionless. With Equations 2.40 and 2.41, the first-order correlation function is defined as:

$$C = \frac{\langle XY \rangle - \langle X \rangle \langle Y \rangle}{\sqrt{\langle (X - \langle X \rangle)^2 \rangle \langle (Y - \langle Y \rangle)^2 \rangle}}. \quad (2.42)$$

The incoherent domain from the resulting Fourier transform of a Gaussian temporal bunch is shown in the Figures 2.6 f and 2.8 c. The Gaussian temporal bunches were generated and Fourier transformed as presented in the previous section. The simulation forwarded only the frequencies from the ultraviolet to infra-red domain, i.e. 334 THz to 1500 THz. The bunch length is stored in the width of the fluctuations and may be retrieved by calculating the correlation of different frequency intervals $\Delta\nu$. We therefore take the first order correlation of the frequency response.

Gaussian Bunch simulations

The correlation was calculated for different frequency shifts $\nu + \Delta\nu$ across a single spectrum. For a single correlation point the frequency ν was increased for a single frequency shift $\Delta\nu$. The resulting data in Figure 2.10 (a) shows a Gaussian response. At $\Delta\nu = 0$ the correlation C , as presented in Equation 2.42, is one and tails off to zero for higher shifts $\Delta\nu$. The width of the correlation peak around $\Delta\nu$ is a measure of bunch length. In order to extract this bunch length, the FWHM or standard deviation of the peak is recorded.

Figure 2.10 (b) shows the correlation peak width versus bunch length. The bunch length was varied between 15 fs and 150 fs. The figure shows the data points with standard error of 10 measurements. It was noted by [27] that the correlation between bunch length and the correlation width was $\sigma_t \propto \sigma_\nu^{-1}$ where σ_t is the rms bunch length and σ_ν is the rms correlation width. The fit is of the form $y(t) = ax^{(b)}$ in which a and b were 0.1937 and -0.9875 respectively with a confidence level of 95%, corresponding well to the predicted inverse proportionality that was predicted. Although the bunch length was fixed in the simulation program, the standard error of 10 simulated bunches increases significantly towards higher compressions, i.e. shorter bunch lengths.

Flat top simulations

Similarly to the previous section, a temporal flat-top electron bunch was analysed to assess if the bunch shape could be retrieved.

Analysing the fluctuations by performing the first order correlation, the data in Figure 2.11 (a) was obtained. As expected the correlation peak around zero broadens as bunch length was reduced. A drawback is that the correlation peak does not show bunch shape information since a Gaussian shape peak was observed. Performing the simulation over different bunch lengths gives the result in Figure 2.11 (b). The bunch length follows a power function similar to the Gaussian bunches, expressed as $\sigma_t \propto \sigma_\nu^{-1}$.

Bunch length limits

If a Gaussian shaped bunch is assumed and the fluctuations we measure are due to bunch length, the fluctuations relate to bunch length via the following equation (rewriting the equation in the inset of Figure 2.10 (b)):

$$\sigma_b = 10^{\frac{\log_{10}\left(\frac{C_{FWHM}}{a}\right)}{b}}, \quad (2.43)$$

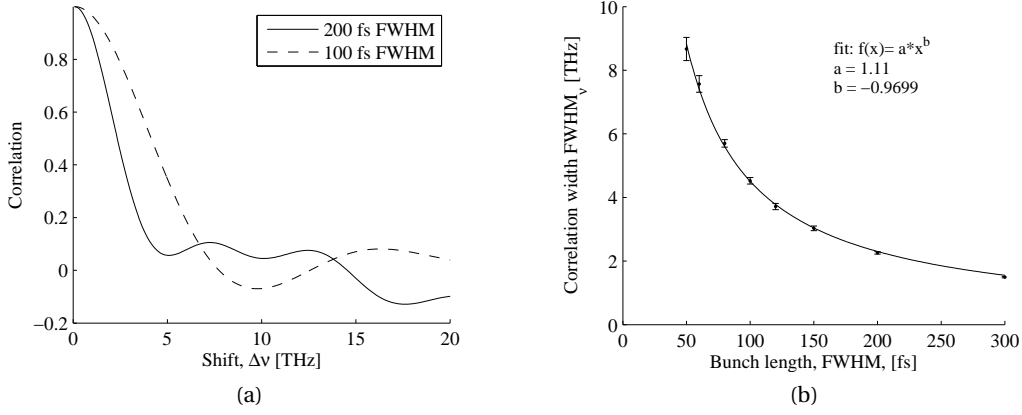


Figure 2.11 – Bunch length analysis of a flat-top temporal profile of 100 fs FWHM and 200 fs FWHM, (a) the correlation plot and (b) the correlation width dependence on bunch length.

where σ_b is the bunch length in seconds and C_{FWHM} is the correlation width in Hz. In Figure 2.10 the parameters $a = 0.1937$ and $b = -0.9875$ were taken from a Gaussian temporal bunch.

The minimum bunch length that may be detected with the proposed method depends on the spectral domain of the spectrometer. The spectrometer used has a spectral domain of 316 THz (950 nm) to 1364 THz (220 nm). The maximum possible FWHM which can be detected is 524 THz. Using Equation 2.43 and a C_{FWHM} of 524 THz, the calculated bunch length is 0.24 fs rms with the Gaussian approximation fluctuation theory.

Conclusions

The correlation theory may be used to measure bunch length single shot. The drawback of the analysis method is that no bunch shape may be retrieved. The minimal bunch length that can be measured depends on the optical spectrometer's domain.

2.4 Current dependence

In this thesis, the correlation theory will be used to extract bunch length information in two ways. Firstly, it will be applied to multiple shots spectra. Secondly, the theory may be applied to extract information from a single shot spectrum.

Because the electron bunch charge was kept low in simulations, to reduce the computation time, the width of the fluctuations were assessed on charge dependence. The bunch length was kept constant and the number of electrons present in the bunch was varied between 0.16 fC to 3.2 pC. The number of spectra used was 20, and the error bars represent the standard error. No change in the correlation width could be observed as seen in Figure 2.12 and thus simulations at a lower charge may be trusted.

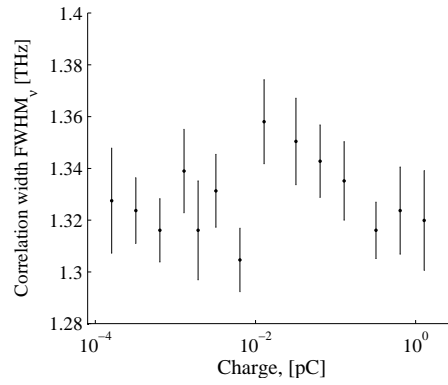


Figure 2.12 – The correlation width dependence on the simulated number of electrons, the error bars represent the standard error of 20 bunches.

2.5 Conclusions

In summary it was shown that for femtosecond bunches, the visible spectrum of transition radiation contains bunch length and bunch shape information. We have tried to exploit this dependency to determine the bunch length in the SwissFEL Injector Test Facility. For infinitely long bunches the visible optical transition radiation spectrum is flat. We can use this incoherent spectrum to measure bunch length and shape. Two methods were presented to extract the bunch length information, namely the $d\Gamma$ and the correlation method.

3 The SwissFEL Injector Test Facility and Bunch Compression

The SwissFEL Injector Test Facility (SITF) is a linear electron accelerator test bed for the future SwissFEL [6, 5]. The goal of the SITF is to analyse the generation and propagation of electron bunches through the accelerator. This leads into the goal of optimising beam parameters such as emittance, stability and bunch length.

As it is a test facility, the SITF does not incorporate all stages and components needed for the final SwissFEL. In order for it to reach the final bunch length, a magnetic compression stage called a bunch compressor is installed. A momentum chirp is generated on the electron profile such that the head of the electron bunch receives less energy than the tail. The momentum chirp onto the electron beam is employed in the bunch compressor to create a path length difference between the head and the tail of the bunch. Thus the head and tail catch up, generating a longitudinally compressed electron bunch.

All experiments described in this thesis have been carried out at the SITF. In the first section the theory is described that is needed to understand bunch compression, the longitudinal phase space and space charge effects. The second section describes the SITF and its main components, which are relevant to this thesis. The third section briefly describes the simulations that are used to model the electron propagation through the accelerator. The fourth and fifth sections describe the linear compression at the SITF of both long and the shortest electron bunches possible. The sixth section describes the transverse space charge effects as a result of the short bunch lengths. The last section summarises the main conclusions.

3.1 Theory

The SwissFEL project has magnetic bunch compressors planned to compress the electron bunches. As a test bed for the future SwissFEL, the SITF has one bunch compressor installed to reduce the bunch length. The beam dynamics to describe the particles from one point in

the accelerator to another is called the beam transfer matrix:

$$\begin{pmatrix} x \\ x' \\ y \\ y' \\ s \\ \delta \end{pmatrix} = \begin{pmatrix} R_{11} & R_{12} & R_{13} & R_{14} & R_{15} & R_{16} \\ R_{21} & R_{22} & R_{23} & R_{24} & R_{25} & R_{26} \\ R_{31} & R_{32} & R_{33} & R_{34} & R_{35} & R_{36} \\ R_{41} & R_{42} & R_{43} & R_{44} & R_{45} & R_{46} \\ R_{51} & R_{52} & R_{53} & R_{54} & R_{55} & R_{56} \\ R_{61} & R_{62} & R_{63} & R_{64} & R_{65} & R_{66} \end{pmatrix} \begin{pmatrix} x_0 \\ x'_0 \\ y_0 \\ y'_0 \\ s_0 \\ \delta_0 \end{pmatrix}. \quad (3.1)$$

In order to compress an electron bunch two parameters are needed, that is the bunch compressor factor called R_{56} and an energy chirp onto the electron bunch, $A = d\delta/ds$, where $d\delta$ is the change in relative energy spread and ds is the change in distance. This section discusses how the bunch length and the aforementioned parameters are related. Secondly, the longitudinal phase space has been extensively used to characterise and measure bunch length, and is treated in this section too. Finally, the effects observed later in this work are mainly as a result of space charge effects, this theory section also addresses this effect and its dependencies.

3.1.1 Linear compression

The initial bunch length at the cathode is designed to be 2700 fs rms. The bunch length after the bunch compressor may be varied by tuning the bunch compressor dipole field or the energy chirp on the accelerator structures. The bunch compressor factor R_{56} is defined as [35]:

$$R_{56} = 2 \left(\frac{L_{mag}}{\rho} \right)^2 \left(\frac{2}{3} L_{mag} + L_{space} \right), \quad (3.2)$$

where ρ is the bending radius of the dipoles, L_{mag} the effective length of the bending magnets and L_{space} the distance between the first and second dipole magnets as well as the third and fourth dipole magnets. The final position of a single particle may be described using the bunch compressor factor R_{56} [36]:

$$s_f = s_i + R_{56}\delta, \quad (3.3)$$

where s_f is the final position of the particle with respect to the reference particle after the bunch compressor, s_i is the initial position before the bunch compressor and $\delta = \frac{\Delta E}{E}$ is the relative momentum difference between the reference particle and the particle of interest. This

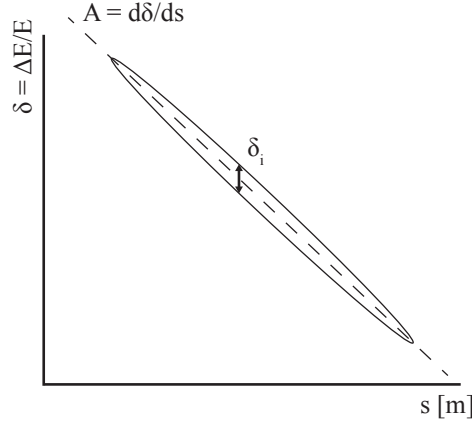


Figure 3.1 – Schematic overview of the linear chirp factor A and the uncorrelated energy spread δ .

equation was limited to the first order. In this equation, δ is independent of the position s_i , thus it is uncorrelated to the longitudinal position. The longitudinal position is introduced through the linear chirp of the electron beam $s_i AR_{56}$. Equation 3.3 becomes:

$$s_f = (1 + AR_{56})s_i + R_{56}\delta_i. \quad (3.4)$$

If a linear correlation is imposed on the longitudinal position versus the momentum of the particle, the slope can be described with $A = \frac{dE/E}{ds}$, which is the linear momentum chirp. Figure 3.1 depicts the linear chirp factor A and the uncorrelated energy spread δ_i .

Considering a bunch of particles, the rms bunch length is defined as $\sigma^2 = \langle (s_f - \langle s_f \rangle)^2 \rangle$. With $\sigma_s^2 = \langle s^2 \rangle$ and $\sigma_\delta^2 = \langle \delta^2 \rangle$, the rms of the bunch length becomes:

$$\sigma_{s_f} = \sqrt{(1 + AR_{56})^2 \sigma_{s_i}^2 + R_{56}^2 \sigma_{\delta_i}^2}. \quad (3.5)$$

If no R_{56} is present, i.e. the bunch compressor is off, the final bunch length is equal to the initial bunch length $\sigma_{s_f} = \sigma_{s_i}$. At maximum compression the term AR_{56} becomes minus one and the minimum bunch length is therefore $\sigma_{s_f} = R_{56}\sigma_{\delta_i}$ where σ_δ^2 is the uncorrelated rms energy spread. In practice we can never obtain the linear approximation and the longitudinal phase space is always slightly curved [36]. This non-linearity may originate from sources including space charge effects in the gun and from the remaining curvature of the acceleration fields. It may also arise from higher order effects in the bunch compressor transfer matrix.

3.1.2 The longitudinal phase space

The longitudinal phase space reveals the momentum spread as well as the temporal structure of the particle beam. To measure the temporal structure, a transverse deflecting cavity is employed. The momentum spread is measured in a dispersive section. The particle position in a longitudinal phase space is now derived.

The transverse deflecting cavity

Electromagnetic fields may be used to deflect charged particles. To derive the deflection at a distance Δz from an electrostatic deflector, the Lorentz force must be considered:

$$\mathbf{F} = e\mathbf{E} + e(\mathbf{v} \times \mathbf{B}), \quad (3.6)$$

where F is the force on the particle, e is the electric charge, E is the electric field, v is the velocity of the particle and B is the magnetic field. In the electrostatic case the magnetic field is zero. To achieve an equilibrium, the centrifugal force on the particle must be equal to the electrostatic force. The centrifugal force is described by $F = \frac{\gamma m v^2}{\rho}$, inserting into Equation 3.6 and $v \approx c$ gives:

$$\frac{\gamma m c^2}{\rho} = eE, \quad (3.7)$$

in which γ is the relativistic factor, ρ is the radius of the electrostatic deflector and m is the mass of the particle. Rearranging the equation with $p = m\gamma c$ and assuming that the deflection angle is small, the deflection Δy at a distance $\Delta z = z_{scr} - z_{TDC}$ becomes:

$$\Delta y(z) = \frac{e|\mathbf{E}|}{pc} \Delta z. \quad (3.8)$$

The transverse deflecting cavity (TDC) is not an electrostatic deflector, but has a varying electromagnetic field. The electromagnetic field is sinusoidally varying in time. The vertical deflection y becomes from Equation 3.8:

$$\Delta y(z) = \frac{e|\mathbf{E}|}{pc} \sin\left(\frac{2\pi}{\lambda} s + \varphi\right) \Delta z, \quad (3.9)$$

where s is the position of the particle with respect to the reference particle at the zero-crossing, λ is the RF wavelength and φ the phase of the RF wave. If no optics were installed and the beam were not deflected between the TDC and imaging screen, the above equation would suffice. However, in order to focus the beam onto the imaging screen, magnetic optics are installed. The β function is a measure of the transverse electron beam size. The relation between the rms beam size σ_b , β -function and the normalised emittance ε_n is $\sigma_b = \sqrt{\beta\varepsilon_n}$. For any lattice the angular to spatial component is defined as [37]:

$$\sqrt{\beta_{d_y}\beta_{s_y}} \sin \Delta\Psi = R_{12}, \quad (3.10)$$

where β_{d_y} is the β value at the deflector, β_{s_y} is the β value at the imaging screen and $\Delta\Psi$ is the phase advance. This component is also called the R_{12} or R_{34} component of the transfer matrix from the TDC to the imaging screen. In order to achieve the best angular to spatial component, the phase advance and the β -functions must be optimised. The phase advance is determined by the lattice. $\Delta\Psi$ must be set as close to 90° (or 270°) as possible to optimise the term $\sin \Delta\Psi$. To obtain the smallest TDC measurement resolution possible, β_{s_y} must be minimised. Conversely, the β at the TDC must be increased so as to maximise the angular to spatial component. Multiplying Equation 3.9 with 3.10 the deflection Δy of an electron becomes [15, 38]:

$$\Delta y(z) = \frac{eV_0}{pc} \sqrt{\beta_{d_y}\beta_{s_y}} \sin \Delta\Psi \sin \left(\frac{2\pi}{\lambda} s + \varphi \right) \Delta z, \quad (3.11)$$

where E is replaced by V_0 , which is the maximum deflecting voltage.

The dispersive section

The high energy spectrometer is a magnetic dispersive section consisting of a single dipole. The horizontal position, x (i.e. the dispersive direction), in the spectrometer depends on the initial position, the initial divergence, the relative momentum of the particle and the magnetic field in the dipole. The transfer matrix for a rectangular dipole with a drift space of length l yields:

$$\begin{pmatrix} x \\ x' \\ \delta \end{pmatrix} = \begin{pmatrix} 1 & \rho_0 \sin(\varphi) + l & \rho_0(1 - \cos(\varphi)) + 2l \tan(\frac{\varphi}{2}) \\ 0 & 1 & 2 \tan(\frac{\varphi}{2}) \\ 0 & 0 & 1 \end{pmatrix} \begin{pmatrix} x_0 \\ x'_0 \\ \delta_0 \end{pmatrix} \quad (3.12)$$

$$\Delta x(z) = x_0(z) + (\rho_0 \sin(\varphi) + l)x'_0(z) + (\rho_0(1 - \cos(\varphi)) + 2l \tan(\frac{\varphi}{2}))\delta, \quad (3.13)$$

where Δx is the horizontal deflection of the particle, x_0 is the initial horizontal position of the particle, x'_0 is the horizontal angular component of the particle, φ is the bending angle of the reference particle and $\delta = \Delta E/E$ is the relative energy deviation from the reference particle. Because the divergence of a single particle is small in comparison to the dispersion of the spectrometer, the second term $(\rho_0 \sin(\varphi) + l)x'_0(z)$ can be assumed to be zero. The focussing in the vertical plane from fringe fields is not taken into account. The radius of the trajectory of the reference particle in the dipole depends on the momentum and the applied magnetic field. The radius of the trajectory of the reference particle is [10]:

$$\rho_0 = \frac{p}{eB} \text{ in practical units } \rho(m) = 3.3356 \frac{\beta E(\text{GeV})}{|B(T)|}, \quad (3.14)$$

where p and e are as defined in section 3.1.2 and B is the magnetic field in the dipole.

3.1.3 Space charge effects

The space charge effect is the force of particles on each other due to the Coulomb fields. The forces may be divided into transverse and longitudinal space charge effects.

Longitudinal space charge effects

The longitudinal electric field E_L of an electron bunch may be described with:

$$E_L(z) = E_z - \frac{q}{4\pi\epsilon_0} \frac{1}{\gamma^2} \left(1 + 2 \ln \frac{r_w}{r_0} \right) \frac{d\lambda}{dz}, \quad (3.15)$$

where E_z is the electric field in the direction of the beam propagation, ϵ_0 is the dielectric constant of the medium, q is the total charge of the electron bunch, γ is the relativistic factor r_0 is the radius of the transverse beam and r_w is the radius of the beam pipe [19]. The particle line density in the longitudinal direction $\lambda(z)$ is described as:

$$\lambda(z) = \int \int \rho(x, y, z) dx dy, \quad (3.16)$$

where ρ is the particle density distribution. Assuming a perfectly uniform electron beam in the direction of travel z , the longitudinal field becomes zero. On the other hand a sharp spike in the electron beam distribution results in large longitudinal electric fields. A sharp spike on the longitudinal profile also induces an AC component on the beam pipe, which acts back on the particle beam, hence the beam pipe radius dependence.

Transverse space charge effects

The transverse force, e.g. in the vertical direction, F_y experienced by a particle is [10]

$$F_y = \frac{1}{4\pi\epsilon_0} \frac{2q\lambda(z)}{\gamma^2\sigma_y(\sigma_y + \sigma_x)} y, \quad (3.17)$$

where $\sigma_{x,y}$ is the transverse beam size and λ as defined in Equation 3.16. From Equation 3.17 it is evident that the transverse force experienced at the boundary due to all other particles is linearly proportional to the charge. More importantly, the electric field experienced is inversely proportional to the square of the relativistic factor. A numerical field may be calculated for before and after the bunch compressor. Before the bunch compressor, the bunch length is 2700 fs (0.8 mm), the typical beam size (r_0) is 0.1 mm and the relativistic factor is 391. The transverse field the particle experiences is 145 V m^{-1} . Leaving all parameters unchanged but varying the bunch length to 100 fs and 10 fs gives 3.9 kV m^{-1} and 39.1 kV m^{-1} respectively. The transverse beam size depends on the emittance of the electron beam and the beta-functions from the lattice: $\sigma = \sqrt{\epsilon\beta}$. Due to the increasing forces, the emittance increases and thus with the same Beta-functions, the transverse beam size becomes larger.

3.2 The SwissFEL Injector Test Facility

The SITF is a 61.4 m linear electron accelerator. The facility can be divided into 6 sections, as shown in the schematic in Figure 3.2. The SITF consists of the RF gun (1), RF accelerating structures (2), the X-band section (3), the bunch compressor (4), the FODO section (5) and finally the high energy spectrometer and beam dump (6). The main characteristic of each section is discussed in turn below.

In the gun section (section (1) in Figure 3.2) free electrons are generated from a copper photocathode. Two lasers are available to generate the free electrons. For simplicity of the thesis, only experiments are presented using the Jaguar (Nd:YLF, Neodymium-doped Yttrium Lithium Fluoride) laser. The laser operates at 1040 nm and is frequency quadrupled to 262 nm [39] with an energy of $250 \mu\text{J}$ per pulse, the temporal profile is Gaussian distributed. With a radio frequency (RF) cavity the electron energy after the gun is 7.1 MeV. The cavity is a 2.6 cell S-band (3 GHz) standing wave RF structure. Included in the gun section is a low energy magnetic

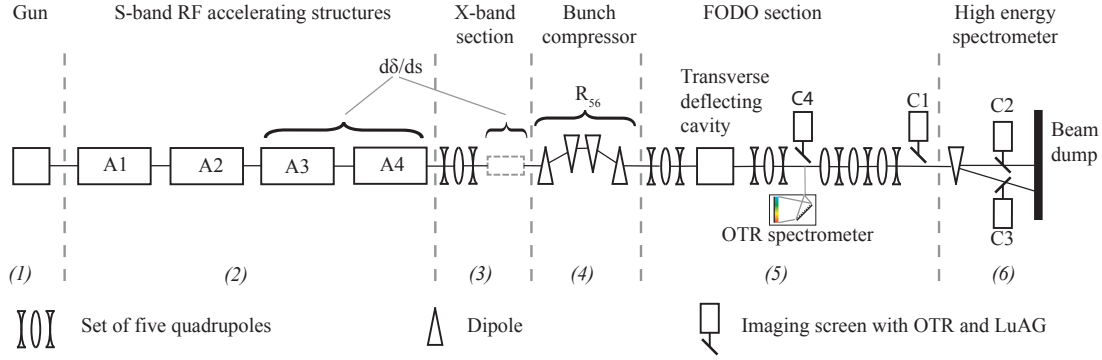


Figure 3.2 – Overview of the SwissFEL Injector Test Facility, divided into six sections. The accelerator structures A1-4 are FINSB01 - 04 and the screens used are C1: F10D1-DSCR75 and 80, C2: F10D100-DSCR10, C3: F10D101-DSCR10 and C4: F10D1-DSCR40.

spectrometer. In the spectrometer arm the energy and the energy-spread can be measured.

Four traveling wave S-band RF structures (section (2), Figure 3.2) accelerate the bunch further up to a maximum of 250 MeV. The momentum may be varied by tuning the power and phase of the RF input. In the case of compression, the last two accelerator structures are set off-crest in order to create a momentum chirp.

The third section linearises the longitudinal phase space and matches the beta-functions. The S-band structures mentioned in the previous paragraph impose a sinusoid shape onto the longitudinal profile. In order to linearise the longitudinal phase space a fourth harmonic accelerator cavity is installed (12 GHz). The phase of the X-band structure is set to the bottom valley of the sinusoid (on-crest + π). The X-band structure decelerates the electron beam. The substructure on the transverse laser beam profile, irradiating the photocathode, changes from day to day due to changes on the laser. Therefore the space charge effects change and thus the emittance as well as the β functions in the accelerator are amended. In order to achieve similar β functions after the X-band section, the quadrupole fields in the X-band section are tuned. The SITF machine is described as ‘matched’ if the Beta-functions after the X-band section can be assumed to be in a fixed state, i.e. the same on every measurement day.

The fourth section, a magnetic chicane consisting of four dipoles, is installed to utilise the momentum chirp to compress the electron bunch. A linear energy chirp means that particles at the head of the bunch have less energy than the particles in the tail. Due to the dispersion of the magnetic chicane the particles with less momentum travel on a longer trajectory. Figure 3.3 shows the principle of the bunch compressor with the longitudinal phase space at the corresponding points.

The fifth section, the FODO section, is used to analyse the beam parameters and consists of correction magnets and quadrupoles. In this section specialised diagnostics are installed such as the transverse deflecting cavity and the optical spectrometer (positioned in the FODO

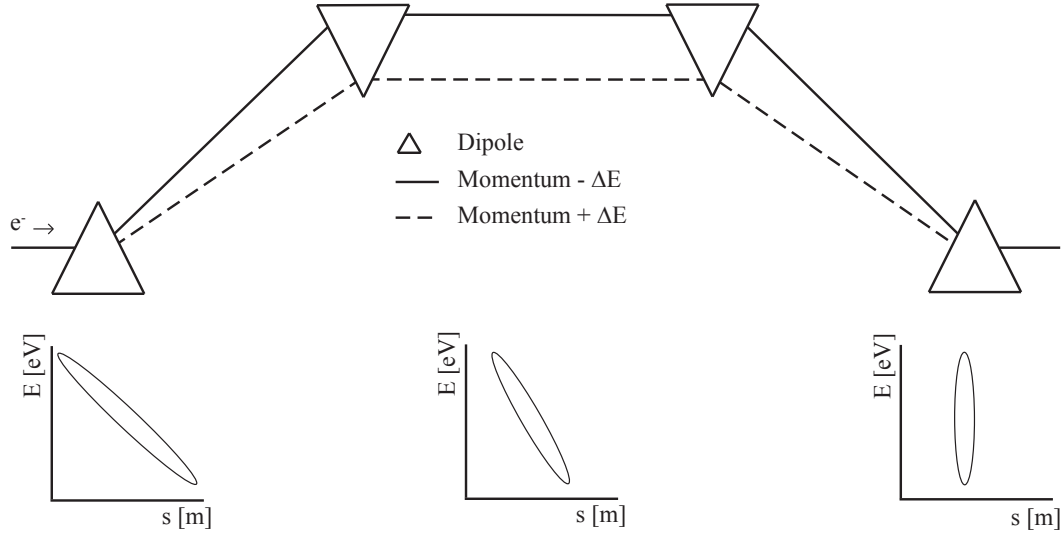


Figure 3.3 – Schematic of the bunch compressor principle.

section, camera C4, Figure 3.2), both to analyse the temporal electron bunch profile. The transverse deflecting cavity is a 3 GHz standing wave 5 cell RF cavity in which the electric fields are oriented perpendicular to the direction of travel. Electromagnetic fields are used despite their inefficiency at relativistic speeds because magnetic dipole fields cannot be varied in the time-scales of sub pico-seconds. The electric fields are sinusoidal in the time domain. Since the bunch length is much smaller than the periodicity, the derivative of the electric field around the zero-crossing may be considered constant.

The high energy spectrometer, is used to measure the particle momentum and its momentum spread at the end of the accelerator before the beam dump. In combination with the transverse deflecting cavity, the high energy spectrometer may be used to view the longitudinal phase space. The dipole provides the energy spread in the horizontal direction whereas the TDC streaks the beam in the vertical direction.

Imaging screens are installed to view the beam in various places along the accelerator. In particular cameras C1-4 were used at the positions presented in Figure 3.2. The imaging screens consist of a set of scintillators and conducting foils which can be inserted into the electron beam path. The generated light is coupled out of the vacuum and collected onto a camera by means of imaging lenses. Both the conducting foils and the scintillators have been installed at every position. At low electron beam charges, the signal to noise ratio of optical transition radiation from the conducting foil is too low. On the other hand, at high charges the beam size is overestimated in the scintillators and optical transition radiation is preferred.

Beam profile images in this thesis are post-processed to reduce the background to zero. The tool used was developed by DESY and described in [40]. The tool collects firstly all intensities from all pixels in a histogram. Since the background intensities are much lower than the

Chapter 3. The SwissFEL Injector Test Facility and Bunch Compression

Table 3.1 – The SwissFEL Injector Test Facility main parameters for the high charge mode (200 pC) [41]

Parameter	Design value
Beam energy	250 MeV/c
Beam charge	200 pC
Initial bunch length (rms)	2700 fs
Designed Minimal final bunch length (rms)	193.3 fs
Initial peak current	22 A
Final peak current	352 A
Compression factor	14.4
Repetition rate	10 Hz

Table 3.2 – Key design parameters of the transverse deflecting cavity [41].

Parameter	Design value
Frequency	2997.912 MHz
Length (flange to flange)	0.5 m
No. of cells	5
Maximum deflecting voltage	4.9 MV
Maximum input power	5 MW
Filling time	0.8 μ s
Operating temperature	40 °C

beam intensity, a limit is set. The image is 2D convoluted to only select a single beam area, discarding single high pixels outside the real beam. The result is an image in which only the beam is visible with the background set to zero.

The main parameters of the SITF are summarised in Table 3.1. The SITF was typically operated at the maximum charge available on the day of operation, ~ 200 pC. The momentum of the electron beam was kept constant at 200 MeV/c. This momentum was chosen instead of 250 MeV/c due to the limited peak voltage available when setting the accelerator structures A3 and A4 off-crest.

3.2.1 TDC Setup in the SITF

The transverse deflecting structure is installed at position $z = 42.7$ meters (see Figure 3.2). Specifications of the deflecting cavity can be found in Table 3.2. The electric field in the accelerator structure is an S-band standing wave. The electric fields are vertically orientated, perpendicular to the beam direction. The maximum power from the klystron is 5 MW, with a deflecting field of 9.8 MV/m.

The standard bunch length measurements are performed at screen C1 (see Figure 3.2) at $z = 57.0$ m. In this work the bunch length could not be measured in a non-dispersive section because of space charge effects and therefore the screen in the high energy spectrometer (C3)

Table 3.3 – Accelerator code summary, simulating the SITF with relevant parameters.

Parameter	Astra	Elegant	CSRtrack
Acceleration	✓	✓	X
Longitudinal space charge	✓	✓	✓
Transverse space charge	✓	X	✓
Optimisation tool	X	✓	X

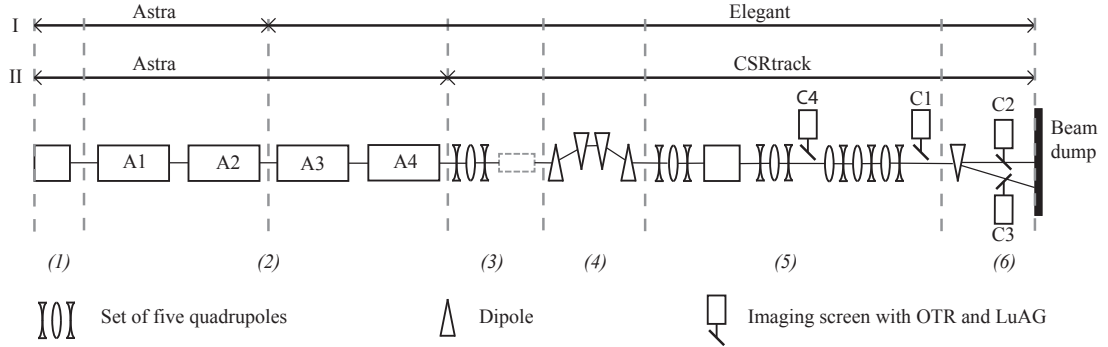


Figure 3.4 – Overview of the SwissFEL Injector Test Facility with the accelerator codes used in the indicated sections. Two simulation schemes are shown, I is the simulation scheme using Astra and Elegant and II used Astra and CSRtrack as simulation codes.

was used.

A high energy spectrometer is installed 14.8 m downstream the TDC ($z = 58$ m). The dispersive section consists of a single dipole with an effective length of 424 mm. The bending angle is 6 degrees. The field strength is 5.917 mT/A with a maximum current of 80 Amperes. At 200 MeV/c the calibration is 728.5 keV/mm on the screen in the spectrometer arm (camera C3 in Figure 3.2).

3.3 Simulations of the SITF

The SwissFEL will produce electron bunches in the sub-fs range. As seen from Table 3.1 the SITF was not designed to create bunch lengths below 190 fs. The electron bunches were compressed to sub-100 fs bunch lengths in order to develop corresponding diagnostics. This resulted in undesirable collective effects acting on the beam, limiting the bunch length and amending the longitudinal phase space.

In order to verify methods and effects seen in the longitudinal phase space, simulations of the injector were performed with several codes. Astra [42], Elegant [43] and CSRtrack [44] were used to simulate the beam transport. Table 3.3 summarises the different accelerator codes and their virtues considered for this project. Figure 3.4 shows the accelerator codes and where the respective accelerator codes were used for two simulation options.

In the first option Astra and Elegant were used. Astra (A Space charge TRacking Algorithm) is an algorithm designed to take space charges into account with low energy beams. The algorithm is invaluable at low momenta but lacks the flexibility at higher energies as well as 3D calculations in dispersive sections. The code Astra comes with a generator, which is used to generate a distribution of particles at the cathode surface. From this point onwards Astra was used from the gun to after the second accelerating structure, where the beam energy was 121.8 MeV. The spot size on the cathode was 0.275 mm, radially distributed. The bunch length at the cathode was Gaussian distributed with a standard deviation of 2.7 ps.

Elegant is an accelerator code used for particle tracking but lacks the ability to take transverse space charges into account. Elegant was used from the beginning of the third accelerating structure to the beam dump. This program was chosen instead of Astra because of its optimisation capabilities and the bunch compressor dynamics since Astra calculates the space charge forces on a cylindrical grid.

Similar to the experiment, the optics in the X-band section needed to be matched in order to satisfy the conditions such that the bunch length could be measured at the high energy spectrometer. In the simulation the quadrupoles after the bunch compressor were fixed. The optics were matched with the following conditions:

- The phase advance between the TDC and the screen C1 was set to 270 degrees. The phase advance to the high energy spectrometer is similar in that case.
- The Beta-functions should stay within 0.1 m and 200 m over the whole accelerator.
- The beta-function at the screen C1 is minimum in both the x and y direction, thus a focus in order to achieve the maximum resolution.
- The beta-function at the X-band accelerator structure is minimum in both the x and y direction

The variables to optimise were all quadrupoles in the X-band section. The dispersion and the horizontal tune were not optimised.

In the second option, both Astra and CSRtrack were used. This second option was used because of the space charge limitations in Elegant. Two accelerator structures were added to the Astra simulation, taking the Astra simulation up to the end of the X-band section. Because no optimisation toolbox is implemented in CSRtrack, the optics were taken from Elegant and implemented into CSRtrack. However, due to limitations in CSRtrack, the horizontal x (and vertical y) versus the position along the bunch s remains unchanged. This means that no phase advance is calculated by CSRtrack and thus that the focus at the high energy spectrometer and the screen C1 are wrong. Instead of implementing optics, the accelerator has also been simulated using no quadrupoles, only the bunch compressor dipoles, reducing the accelerator to a drift space with a bunch compressor. Hence both the beam size and the resolution at the screen C1 and the high energy spectrometer are large.

3.4 Linear compression in the SITF

The following section describes the procedure to perform linear compression to roughly 200 fs rms.

The accelerator is in a state such that the electron bunch is uncompressed and all accelerator structures are set on-crest. The bunch compressor is set to the required angle or R_{56} for the experiment. From this point onwards the R_{56} is held constant since is the focusing effect in the dipoles in the non-deflecting plane change the beta-functions. At this stage the optics are matched, i.e. for a long bunch. This is done because the emittance increases towards sub 100 fs long electron bunches due to space charge effects and cannot be measured with such short electron bunches.

The longitudinal phase space is observed at camera C3 by turning on the high energy spectrometer dipole and the TDC. The accelerator structures' phase of A3 and A4 are set off-crest. Due to the off-crest phase the energy of the electron beam is lower and needs to be compensated for by tuning the A3 and A4 power in the structures. The X-band RF phase is set to the valley (270 deg) by scanning the X-band phase and observing the centre of mass of the momentum at the high energy spectrometer. The X-band power and the A3 and A4 power are simultaneously increased until a linearised electron bunch is observed. The amount of compression at this stage depends on the off-crest phase in A3 and A4 and the R_{56} in the bunch compressor. After this process the bunch length was determined to be roughly 100 fs rms.

Figure 3.5 shows the experimental and simulated linearised longitudinal phase space. Images were recorded at camera C3 in Figure 3.2. The high energy spectrometer dipole was set to 27.8 A, resulting in a screen calibration of 0.73 MeV mm^{-1} . The temporal calibration with the TDC was 60.0 fs mm^{-1} . The longitudinal phase space is slightly non-linear. As discussed, this non-linearity comes from space charges in the gun area, the higher order components in the bunch compressor dipoles and the remaining curvature of the RF accelerator fields. These effects could not be compensated for in the SITF.

For the simulation as presented in Figure 3.5 b 0.1 million particles were used. Astra and Elegant were used for this simulation. The simulated longitudinal phase space was recorded at the high energy spectrometer (Corresponding to camera position C3). The simulated momentum space shows a break-up, this is likely due to the limited number of electrons used in the simulation and the limited bins to calculate the space charge forces. The experimentally obtained longitudinal profile in Figure 3.5 a shows break-up in the momentum domain, as indicated in the figure with two arrows. This can be explained by longitudinal space charge effects.

In order to prove that the momentum break-up originates from space charge effects, an extreme case must be considered such as non-linear compression. For the studies presented, the X-band RF was turned off, hence the longitudinal phase space shows the curvature of the electromagnetic fields of the S-band RF. The experimental beam parameters were 200

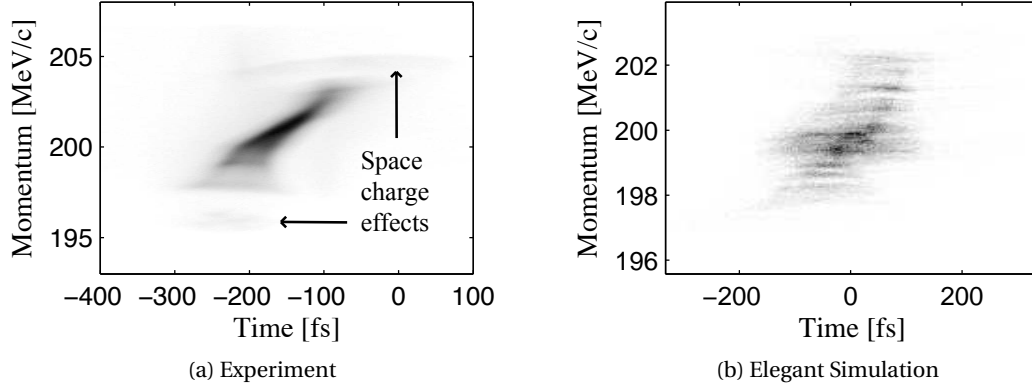


Figure 3.5 – The current density in the longitudinal phase space of (a) the experiment and (b) a simulation. Although the compression is variable, the bunch length and momentum space are of the same order. The filamentation seen in the simulation is an artefact due to the limited number of particles.

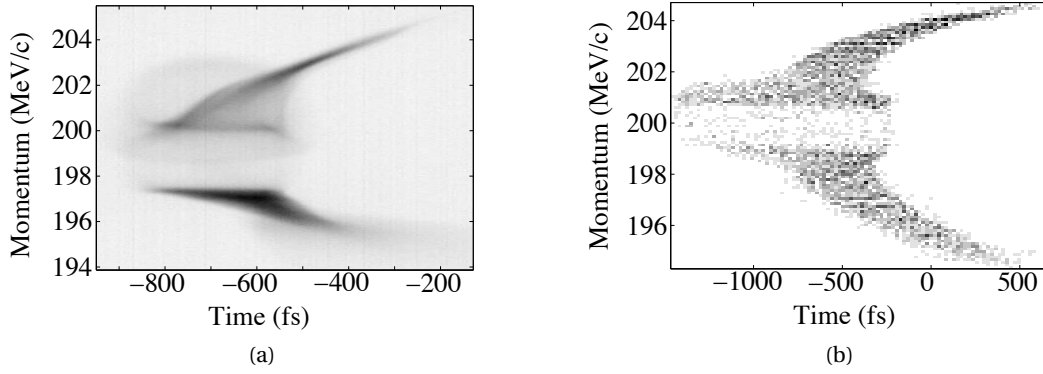


Figure 3.6 – Observed (a) and simulated (b) longitudinal phase space at camera C3, the simulation was performed with CSRtrack.

MeV/c and 115 pC. The bunch compressor and the momentum chirp were set such that the electron beam was fully compressed. The experimental longitudinal phase space at maximum compression is shown in Figure 3.6 (a). The imaging screen C3 in Figure 3.2, was used for both the simulations and the experiments. The experiment shows that energies are missing at the head of the bunch, representing an energy hole in the momentum space.

In order to understand the process, the simulated bunch compression was set off crest without X-band linearisation. The bunch compressor, FODO section and high energy spectrometer were simulated using CSRtrack (Option II in Figure 3.4). The result in Figure 3.6 b shows the CSRtrack simulation. With Astra the electron beam was simulated until the beginning of the X-band section. CSRtrack was used to simulate from here on until the spectrometer screen. The resulting longitudinal phase space corresponds very well with the experiments though as a result of the missing optics, the beam size at the high energy spectrometer dipole was large,

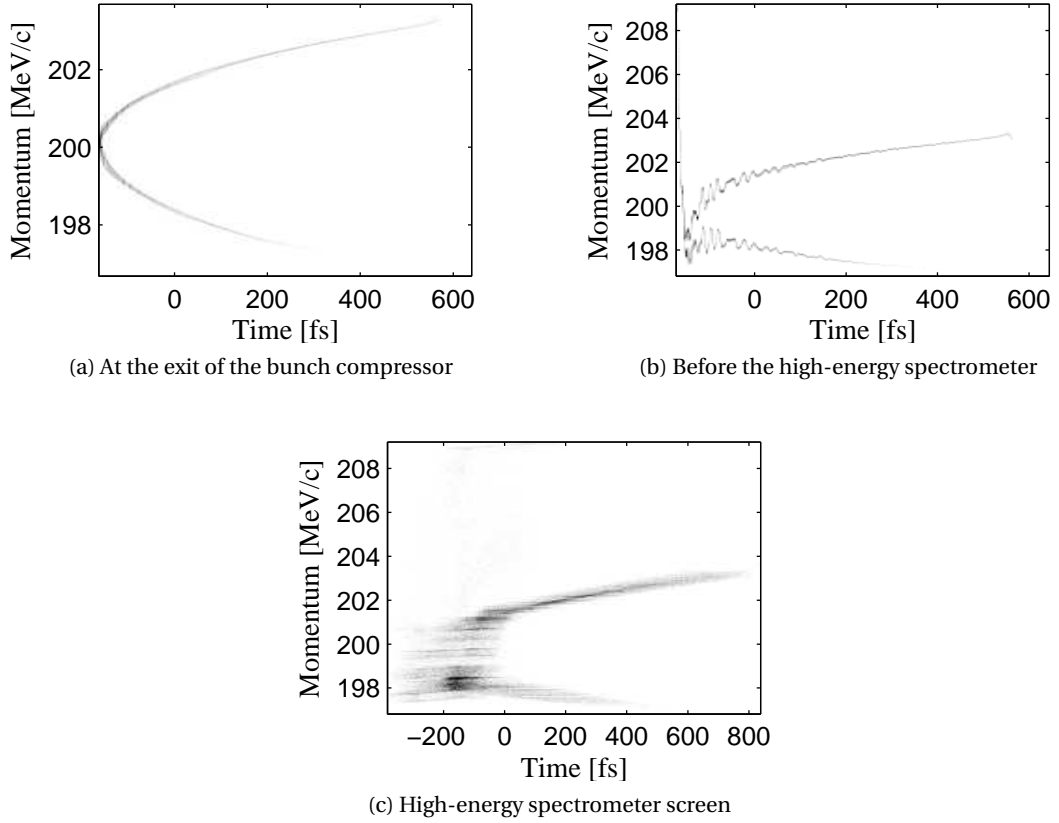


Figure 3.7 – Astra and Elegant simulation of the SITF, 20,000 particles, 200 pC.

which resulted in a time broadening in the simulations due to the path length difference.

Simulation option I (see Figure 3.4) was also used to simulate the longitudinal phase space on (longitudinal) space charge effects. The longitudinal phase space at different points in the injector are shown in the plot in Figure 3.7. After the bunch compressor the sinusoidal shape is perfectly imprinted onto the longitudinal phase space. However, as we enter the space charge dominated FODO-section, the very first electron in the bunch experiences all the longitudinal space charge force from all other particles. As a result the very first electrons (head of the bunch) increase in energy, as shown in Figure 3.7 (b). The fluctuations onto the profile after the head of the bunch is probably due to the limited number of particles in the simulation. The resulting momentum gap is not as profound as with the CSRtrack simulations due to the limited number of particles in the bunch and the possible absence of transverse space charge fields. Thus it can be concluded that the underlying effect of the gaps in the longitudinal phase space in Figure 3.5 are due to longitudinal space charge.

3.5 Generation of sub-100 fs electron bunches

3.5.1 X-band phase to reduce bunch length

For studies involving the bunch length, a single parameter was found to change the bunch length reliably below 100 fs. The fourth harmonic RF accelerator phase was set to a valley as discussed in section 3.2. Within a couple of degrees the curvature of the X-band can be treated in the same way.

Figure 3.8 shows the simulation of a linear compressed beam. The phase space was initially linearised around the X-band phase of 270 degrees as shown in Figure 3.8 (b). In the other diagrams only the X-band phase was adjusted. Simulations of the X-band section, the bunch compressor, the FODO section up until the high energy spectrometer reference screen, C2 were carried out with Elegant. In the simulations of the non-dispersive arm the longitudinal phase space is linearly compressed until the maximum compression at 271.25 degrees. The first two X-band phases show fluctuations of the longitudinal phase space profile. This is likely due to the limited number of particles simulated (0.1 million, limited due to the computation time). At the X-band phases of 271.25 and 272.0 degrees, it can be seen that the momentum spread increases considerably from 198 and 202 MeV to 175 and 225 MeV, in comparison to the X-band phases of 268 and 270 degrees.

The resulting rms bunch length versus the X-band phase is plotted in Figure 3.9. It can be assumed that the electron bunch is compressed linearly within 2 degrees on either side of the off-crest phase. The data in the figure shows the bunch length with and without longitudinal space charges. At long bunch lengths the space charge effects have no influence on the bunch length. However, at the shortest bunches, the longitudinal space charge increase the bunch length. Two longitudinal current profiles at the shortest bunch length can be seen in Figure 3.10. The bunch length without longitudinal space charge was 8.4 fs. With space charge effects the rms bunch length is 23.7 fs, though the shortest bunch length with longitudinal space charge is 19.5 fs at an X-band phase of 271 degrees.

3.5.2 Scrapers to reduce bunch length

As discussed in chapter 2, incoherent radiation from OTR contains bunch length information. However, the OTR intensity under sub 100 fs rms bunch length gives coherent OTR radiation, potentially overshadowing the incoherent domain. In order to achieve sub-100 fs electron bunches, without coherence effects, scrapers in the bunch compressor were employed to reduce bunch length.

The schematic of the principle of bunch length reduction is shown in Figure 3.11. Scrapers are copper rods that can be moved into the beam path. The scrapers are located in the middle of the bunch compressor and scrape electrons away in the dispersive (horizontal) direction. Due to the linear correlation between the momentum and longitudinal position within the

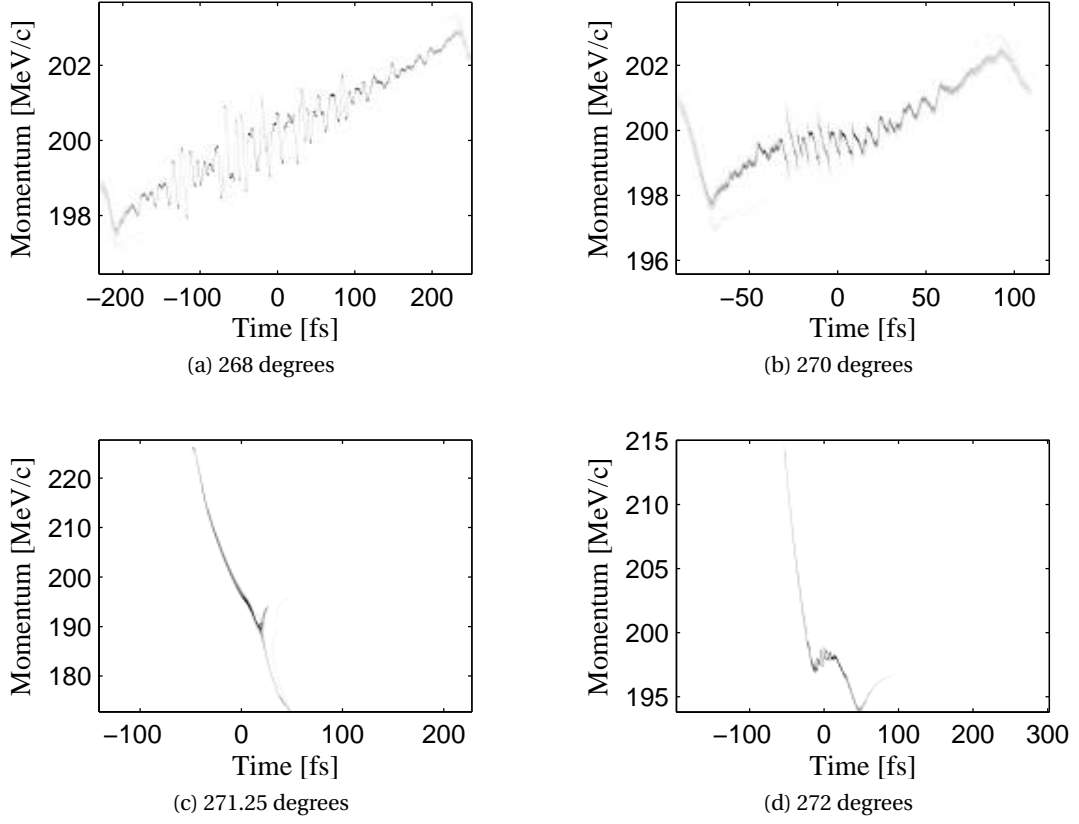


Figure 3.8 – Simulated longitudinal phase spaces of an X-band accelerator phase scan.

electron bunch, the longitudinal phase space is linear. A resulting longitudinal phase space is shown in Figure 3.12. The plot shows that the longitudinal phase space is still linearised. However, lobes can be seen, extending from the outer edges of the profile, as indicated with an arrow. The data in Figure 3.12 (b) is deliberately saturated to enhance the lobes.

The reason for the lobes towards lower and higher energies respectively is longitudinal space charge. By inserting the scrapers, a sharp edge on the current density is created, thus creating high space charge forces. The lobes at the head of the bunch experience all the space charge behind them, which leads to an increase in momentum. Similarly, the electrons at the tail experience all the electrons before and thus leads to a decrease in momentum.

3.6 Transverse space charge effects

When the electron bunch is compressed, the peak current of the bunch increases. An electron beam can be referred to either as an emittance-dominated beam or space charge-dominated beam. If the currents are low and the space charge effects can be neglected, the emittance of the beam remains the same. However, if a particle beam is in a space charge dominated

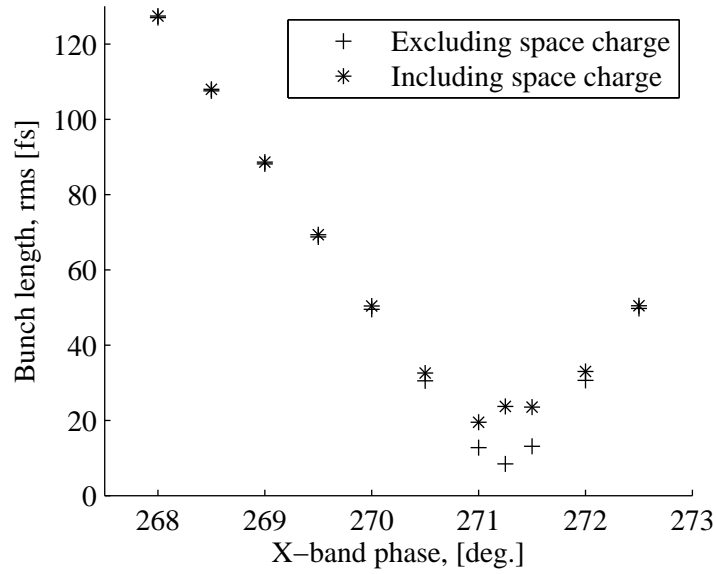


Figure 3.9 – The simulated bunch length versus X-band phase of an Elegant model excluding and including the longitudinal space charge effects.

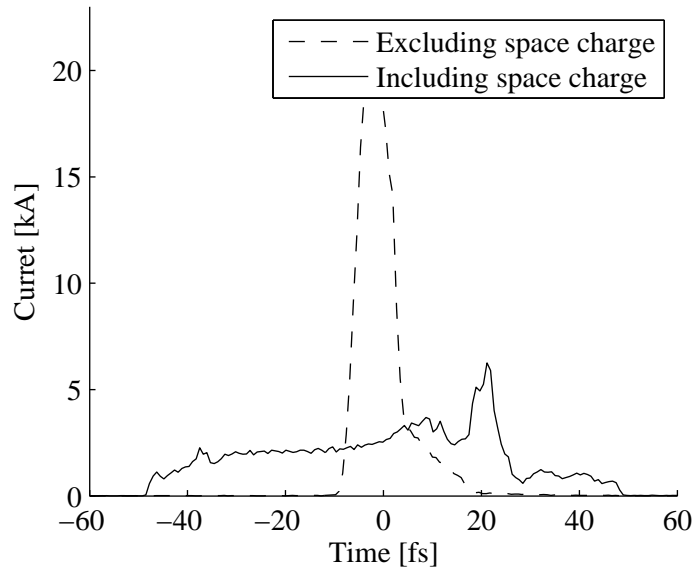


Figure 3.10 – Simulated current profiles at the shortest bunch length at an X-band phase of 271.25 in Figure 3.9.

section the space charge increases the emittance.

The beam is transversely Gaussian distributed at long bunch lengths. It becomes larger at smaller bunch lengths. The plot in Figure 3.14 shows the mean and rms standard error of 10 beam sizes recorded at the position C4 (see Figure 3.2). Firstly, the beam size increases with a

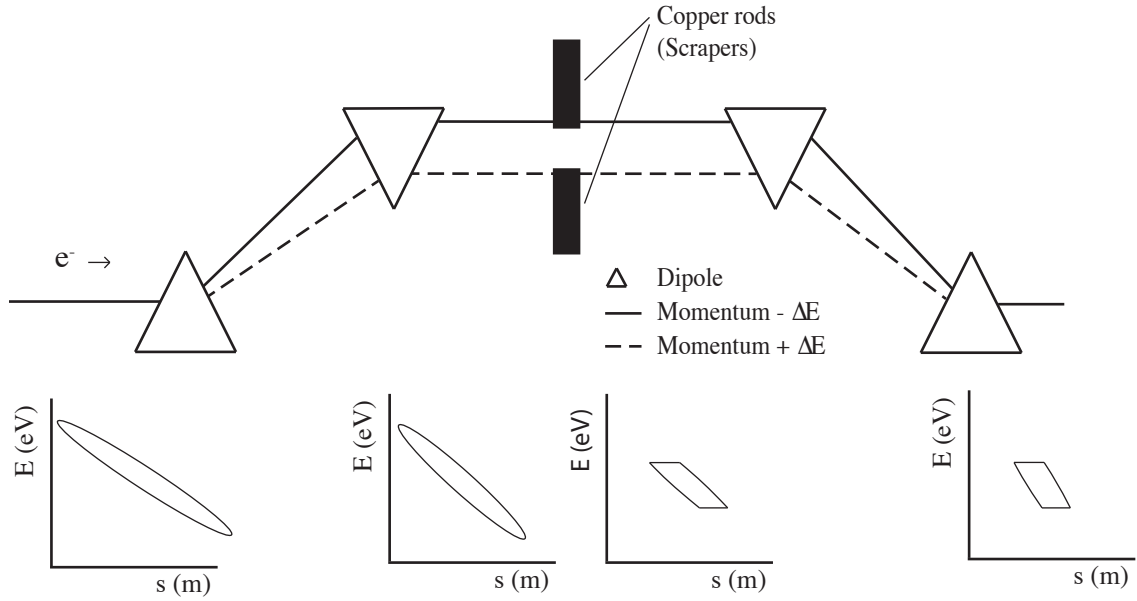


Figure 3.11 – Schematic of using the bunch compressor scrapers to reduce bunch length and charge.

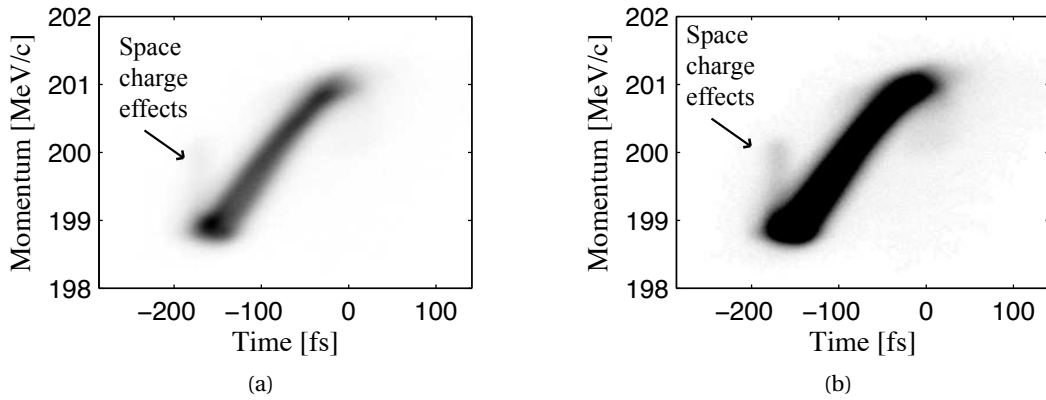


Figure 3.12 – Experimental charge density profile of (a) a compressed bunch with scrapers employed and (b) the same plot but the colour scheme amended to visualise the space charge effect.

factor 2 from the longest bunch length to the smallest bunch length. Secondly, the standard error increases towards higher X-band RF phases and thus to smaller bunch lengths.

The observed transverse beam profiles show that the beam does not only becomes larger but also breaks up, as shown in Figure 3.13. It can be seen together with the standard error of the data in Figure 3.14 that the transverse beam profile varies more at higher compressions. The cause of the variability of the transverse beam profile is likely due to the single particle content of the electron bunch, which varies from shot to shot. Both coherent synchrotron radiation as well as space charge effects may have caused this transverse beam size variability.

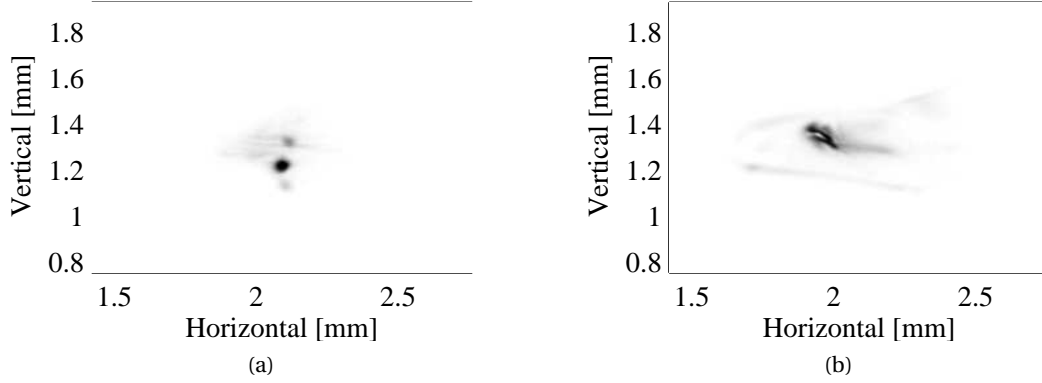


Figure 3.13 – The transverse charge distribution in a non-dispersive section of a (a) long electron bunch (X-band phase: 270.8 deg., roughly 110 fs rms) and (b) short bunch (X-band phase: 272.8 deg., roughly 25 fs rms). The transverse beam profile blows up as the bunch is compressed.

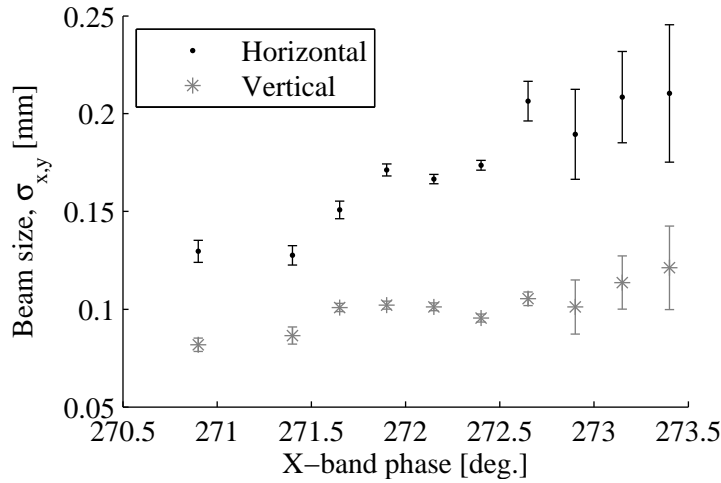


Figure 3.14 – The transverse beam size as a function of the X-band phase. The minimum bunch length is located at an X-band phase of 273.3 degrees.

3.7 Conclusions

In this chapter the theories needed to understand the bunch compression and the beam behaviour in longitudinal phase space were explained. The SITF and the main components were presented and identified for longitudinal compression. The simulations were briefly described and successfully applied to simulate the bunch compression as well as longitudinal space charge effects. The minimum bunch length is limited not by the R_{56} as explained in the theory but due to longitudinal space charge forces. The X-band phase was found to change the bunch length reliably with a linear longitudinal phase space within ± 2 degrees, providing a single parameter adjustment to change the bunch length. The bunch length could also be changed using the bunch compressor scrapers. Both the X-band phase and the scrapers have

been used to reduce bunch length in this thesis. Finally, due to transverse space charge effects, the transverse beam profile is enlarged towards smaller bunch lengths. The transverse beam profile is broken up and the intensity profile changes from shot to shot. The cause of the variability in the transverse profile was unknown, both coherent synchrotron radiation as well as space charge effects could have caused this variability.

4 Bunch Length Measurement in a Space Charge Dominated Beam Using a Transverse Deflecting Cavity

The Transverse Deflecting Cavity (TDC) is routinely used to measure bunch length and is considered a true and reliable tool for such measurements, as well as to evaluate the current profile. In the SITE the measurement of bunch length is routinely performed in the FODO section [45]. The electron beam is streaked onto a screen downstream of the TDC. The projected intensity on the vertical temporal axis is then recorded. The intrinsic (unstreaked) vertical beam size defines the resolution of the measurement, however if it is large and it changes along the electron bunch, this method fails.

This chapter proposes an analysis method to measure the bunch length in space charge dominated beams using the TDC in combination with the high energy spectrometer. The advantages are that the analysis method may be used with large intrinsic beam sizes at the screen and thus with sub 0.2 ps electron bunches. The concept of the proposed method is discussed in section 4.1. The screen calibration needed to label the longitudinal phase space including errors and jitter is discussed in section 4.2. The experimental procedure is then presented in section 4.3. This method was validated via simulations of the SITE, the procedure and results of which are presented in section 4.4. Following these calculations, the results from two experimental analyses are presented (section 4.5), proceeded by a discussion of the strengths and weaknesses of the measurement technique, especially considering the accessible resolution (section 4.6). This chapter is concluded with the main findings summarised in section 4.7.

4.1 Concept

A schematic of the concept of the bunch length measurement using the TDC in combination with the high energy spectrometer is shown in Figure 4.1. The intrinsic beam and the streaked beam at the high energy spectrometer are shown. The TDC streaks vertically in the SITE, thus the horizontal axis depicts the vertical placement of the bunch.

A single electron may have a vertical position y and a divergence of the reference particle of $y' =$

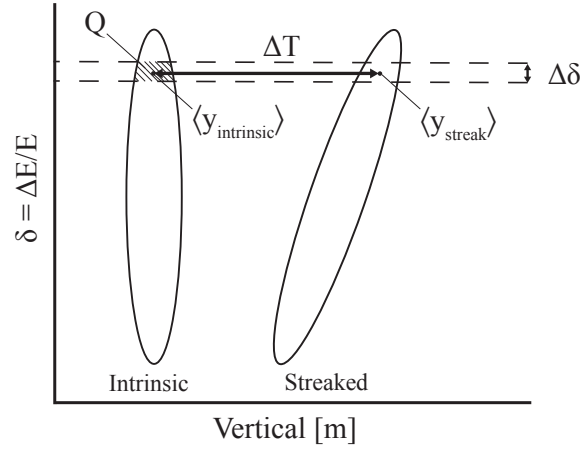


Figure 4.1 – High energy spectrometer, schematic depicting unstreaked (intrinsic) beam and the streaked beam, the charge Q , time ΔT , relative energy spread $\Delta\delta$ and the centre of masses $\langle y_{intrinsic} \rangle$ and $\langle y_{streak} \rangle$.

dy/ds . In the transverse phase space y, y' a phase advance of 90 degrees transfers the vertical divergence y' to y . Thus in order to optimise the TDC resolution, the phase advance from the TDC to the imaging screen must be set to 90 degrees or 270 degrees in order to optimise the angular to spatial component of the TDC. Due to the angular to spatial component (see chapter 3), the longitudinal position of the particle versus the vertical divergence t, y' at the TDC transfers to t, y at the high energy spectrometer. If the TDC is turned on, the RF gives an additional angular kick y'_{streak} depending on the position t within the electron bunch. At the high energy spectrometer the position at the screen becomes $t, y_{intrinsic} + y_{streak}$. Since the streak of the TDC depends on the longitudinal particle position within the bunch, the difference $y_{streak} - y_{intrinsic}$ holds the bunch length information.

In the following, a method is described that makes use of the dispersion on the spectrometer screen to improve the resolution. Firstly, the beam is sliced on the energy axis. In such a slice $\Delta\delta$, a charge Q and a centre of mass $\langle y \rangle$ are identified for both the streaked and intrinsic beam. The time difference ΔT is defined as:

$$\Delta T = (\langle y_{Streak} \rangle - \langle y_{intrinsic} \rangle) B \quad (4.1)$$

where B is the time calibration in the vertical direction in ps mm^{-1} . If the number of slices $\Delta\delta$ are increased, more measurements of ΔT are available. Depending on the intrinsic size of the beam, this may increase the resolution of the measurement. It will be shown that with charges Q appearing at times ΔT , a current profile may be reconstructed.

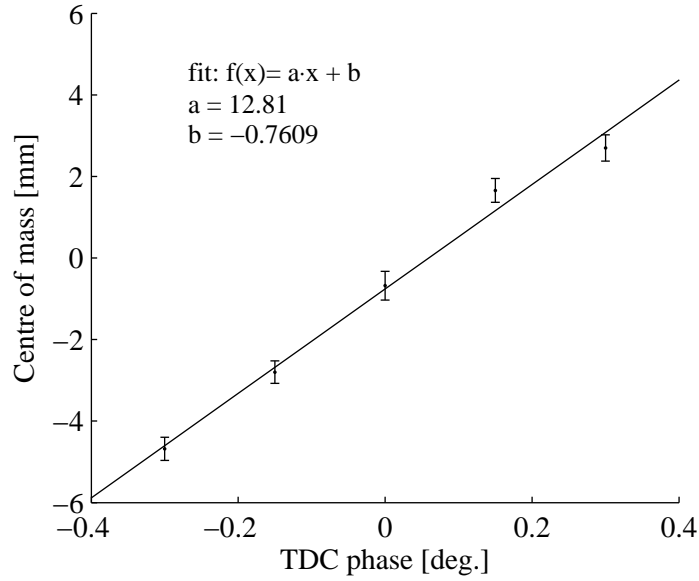


Figure 4.2 – Temporal calibration plot of the TDC deflector phase versus the deflection at screen C3 (F10D101).

4.2 Time calibration

The high energy spectrometer arm has an imaging system, which shows the horizontal versus the vertical current density distribution of the electron beam. In order to convert from the spatial domain to the momentum and temporal domain, the screen position must be calibrated.

The calibration of the momentum on the high energy spectrometer screen is straightforward. The beam is centred on the high energy spectrometer reference screen C2. With Equation 3.14 the magnetic field is calculated for a given momentum. The high energy spectrometer dipole is set such that the centre of the high energy spectrometer arm is 200 MeV/c.

Conversion to the temporal domain requires calibration using the TDC. Chapter 3 gives a short overview of the TDC, in which it was stated that the TDC was operated at the zero-crossing. The zero-crossing TDC phase is defined as the phase where the total centre of mass of the electron bunch is not deflected. Calibration of the time domain requires scanning of the TDC phase around the zero-crossing. The data and fit in Figure 4.2 show such a calibration. The phase was varied between ± 0.3 degrees in five steps with 25 images taken at each TDC phase. From each image the centre of mass was calculated in the vertical direction. The experimental data shows the centre of mass of each image versus the TDC phase and the error-bars represent the standard error. The TDC phase stability was 0.035 deg. rms.

The slope of the TDC around the zero-crossing may be considered constant. Thus the fit to the data is a linear function, which is in Figure 4.2 (12.81 ± 1.28) mm deg⁻¹. With the TDC

Chapter 4. Bunch Length Measurement in a Space Charge Dominated Beam Using a Transverse Deflecting Cavity

Table 4.1 – Arrival time jitter at screen C3. The mean jitter and the standard deviation of the jitter are taken at 5 different TDC phases

Date	Jitter
01.09.2013	(110.3 ± 11.6) fs
01.10.2013	(172.6 ± 40.3) fs
01.11.2013	(140.1 ± 52.1) fs

frequency of 3 GHz, the calibration is (13.83 ± 1.38) mm ps⁻¹.

The error bars on the data-points in Figure 4.2 indicates the temporal fluctuations present in the SITE. The jitter at the zero-crossing in the presented calibration is 1.72 mm rms, corresponding to 124.4 fs rms. The measured jitter coming from the TDC RF phase was 0.036 degrees rms, resulting in a temporal jitter of 33 fs rms. The the jitter from other sources becomes $\sqrt{124.4^2 - 33^2} = 119.5$ fs. These other sources may include the laser arrival time stability with the RF phase stability, the RF phase stability in respect with each other and the RF power stability leading to a momentum change and thus a travel distance through the bunch compressor. The analysis of such jitters is non-trivial and without synchronisation of the readout of instruments it is near to impossible to find the correlations to pin-point the jitter source.

To illustrate the difficulty and the variability of measurements, Table 4.1 lists the arrival time jitter recorded on three consecutive days. Measurement data sets as shown in Figure 4.2 were recorded on several dates. At each phase a jitter was calculated. The table shows the mean and standard deviation of the jitter, each acquired from five subsequent TDC phase measurements.

4.3 Analysis procedure

To retrieve the bunch length and current profile, three steps have to be performed. Firstly, the high energy spectrometer image must be recorded (camera C3 in Figure 3.2) for both the streaked and unstreaked beam. The image in Figure 4.3 shows the current density distribution of the intrinsic and of the streaked image. The vertical domain was calibrated as discussed in the previous section and resulted in (13.83 ± 1.38) mm ps⁻¹.

In a second step, the time and charge must be plotted against the momentum slices. The particle density distribution has finite size pixels. For every pixel column we can plot the intensity versus the momentum and determine the centre of mass $\langle y \rangle$ of the unstreaked and streaked slices. With Equation 4.1 the centre of mass of the streaked and unstreaked slices are subtracted and multiplied with the calibration factor, resulting in the time ΔT for every momentum slice (see Figure 4.4). If the bunch is linearly compressed a linear curve is expected. Additionally, the charge in every momentum slice is calculated and plotted in Figure 4.4. The total electron bunch charge was recorded by the BPMs, with the relative intensity in a slice

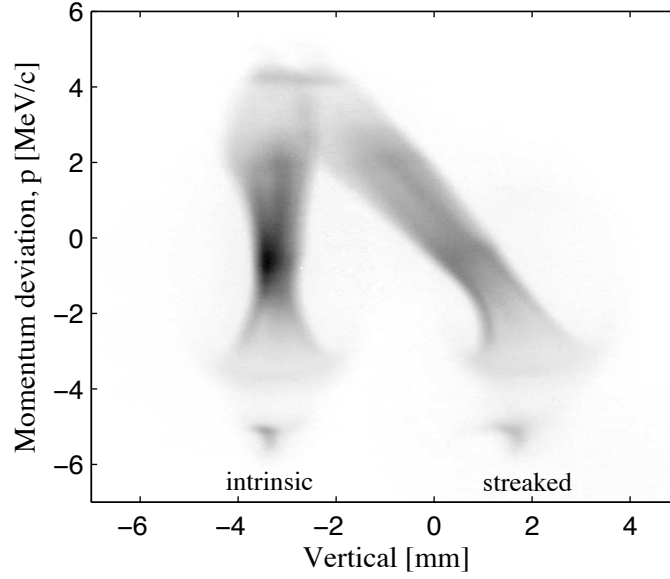


Figure 4.3 – The measured particle density distribution of a streaked and intrinsic beam at screen C3. All data presented in this section has been taken from this dataset.

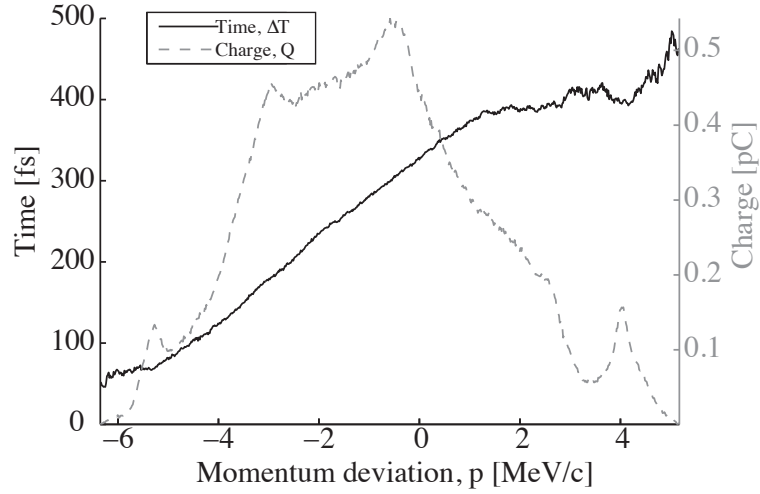


Figure 4.4 – The measured time ΔT versus momentum according to Equation 4.1 and the charge in every slice versus the momentum deviation.

compared to the total intensity, the charge per momentum slice could be calculated.

Finally, the charge as a function of time is plotted and the current profile deduced. The charge Q versus time ΔT of every momentum slice is plotted in Figure 4.5. Since the times ΔT are non-linearly distributed in the time domain, the data presented must be binned in equally spaced time bins, with the charges in those time bins added to each other. Charges under 5% of the maximum charge are omitted. The current profile of two bin-settings are shown in Figure 4.6. Due to the limited number of measurement points the noise on the current profile

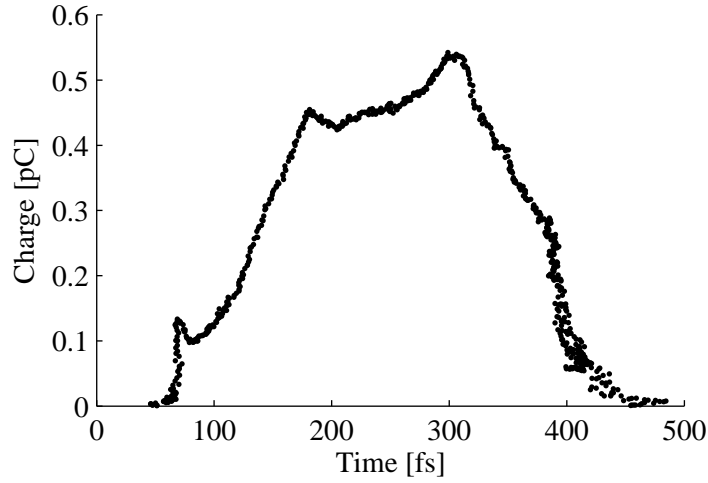


Figure 4.5 – The charge present in every slice versus the time ΔT .

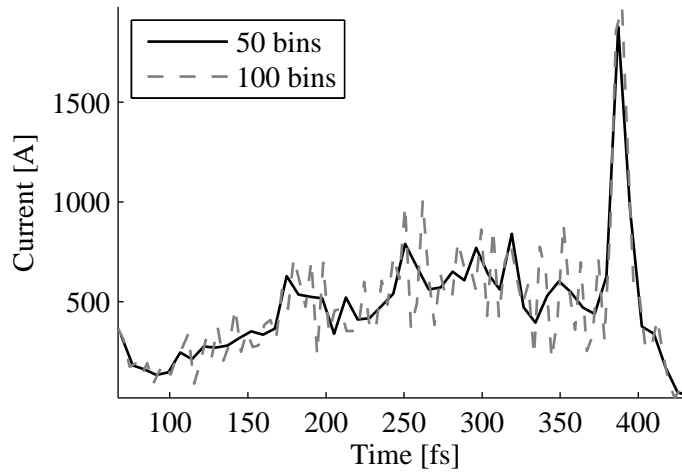


Figure 4.6 – The current profile of an electron bunch with different number of bins to illustrate the increase in noise. The data is the same as in Figure 4.5.

increases. The data also shows that the profile seen in Figure 4.5 has disappeared. The rms bunch length in Figure 4.6 is 92.3 fs. The mean and standard deviation of ten consecutive measurements was $90.7 \text{ fs} \pm 16.9 \text{ fs}$.

4.4 Simulations

Simulations were performed to validate the method and procedure. The simulations were performed with Astra and Elegant (option I, see chapter 3.3). For the simulations 100,000 macro-particles were used with a beam charge of 200 pC. The simulated accelerator was set-up with a bunch compressor angle of 5 degrees ($R_{56} = -69.3 \text{ mm}$). The S-band and X-band RF

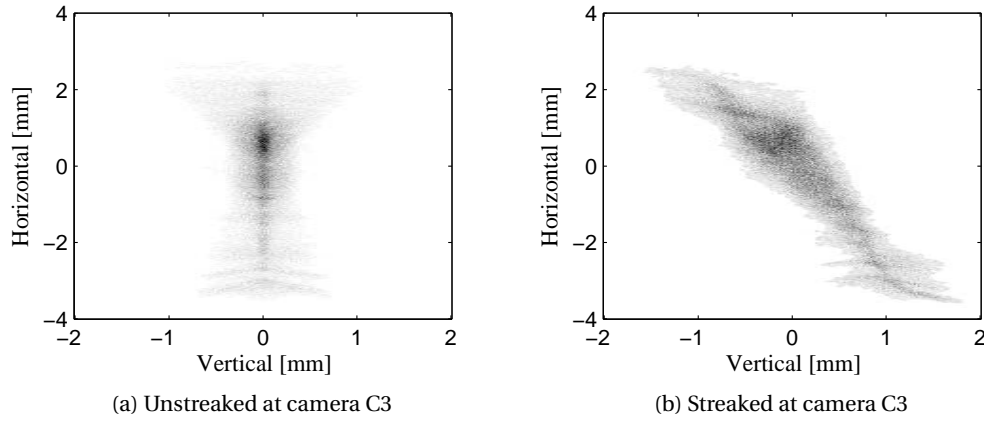


Figure 4.7 – Simulation of the high energy spectrometer (a) without and (b) with transverse deflecting cavity.

structure were set such that the longitudinal phase space was linearised.

The particle distribution on the simulated high energy spectrometer without transverse deflecting cavity can be seen in Figure 4.7 (a). The momentum axis is the dispersive direction which was uncalibrated. A TDC was defined in Elegant with the specifications as described in chapter 3. The current density distribution of the longitudinal phase space is shown in Figure 4.7 (b).

As described in section 4.3, Figure 4.8 is obtained by slicing the high energy spectrometer data and recording the vertical shift as well as the charge present in the slice. The vertical calibration was 11.48 mm ps^{-1} . The momentum versus time shows that the electron bunch is linearly compressed though a small curvature remains at the head and tail of the electron bunch. The momentum versus charge curve shows a broad peak at -1.2 mm . In the following paragraph it will be shown that the charge peak will shift and becomes less broad due to post-processing (binning), though will not disappear.

The streaked simulated image in the dispersive section in Figure 4.7 was 201 pixels by 501 pixels. The number of slices and thus the number of data points in Figure 4.9 is 388. The data in the figure indicates the bunch length ranges from -100 fs to 140 fs . The temporal bunch shape can be extracted by binning the charges in equal temporal bins. Fifty bins were used to calculate the current distribution from the proposed analysis, which is shown as a solid line in Figure 4.10. The simulations have also been carried out up until the spectrometer reference screen C2 (see Figure 3.2), where the temporal profile was extracted. It is shown in the Figure 4.10 as the dashed line. The rms bunch length obtained from the proposed method is 49.8 fs rms compared to 43.7 fs rms at the high energy spectrometer reference screen. However, care must be taken with charge spikes such as those evident in the simulation. Although the broad peak in the horizontal versus charge profile is less broad in the current profile, the effect is present and thus such detected spikes must be carefully interpreted.

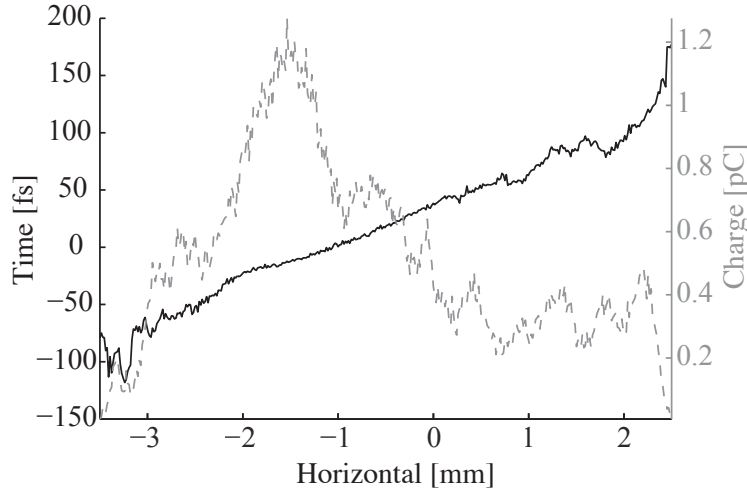


Figure 4.8 – Simulated time versus momentum and charge versus momentum.

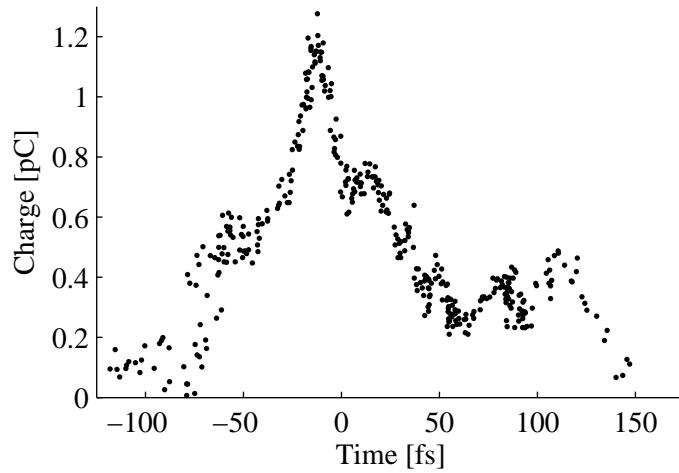


Figure 4.9 – Simulated charge profile

In conclusion, the rms bunch length of the proposed method and the bunch length in the non-dispersive section agree very well. The general current profile obtained with the proposed analysis at the high energy spectrometer is noisy in comparison to the real current profile in the non-dispersive section without TDC on.

4.5 Results

The results from two experimental measurements are presented to show the principle applied to the measurement of sub-100 fs electron bunches. In order to create the sub-100 fs bunches, the SITF was set-up for linear compression. Since the bunch length depends on the off-crest phase of the S-band RF structures, the X-band phase does not correspond to a specific bunch

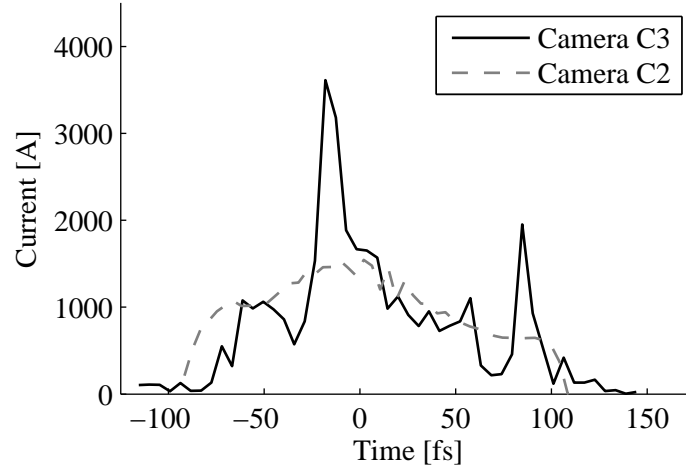


Figure 4.10 – The simulated current profile at the non-dispersive camera C2 and the current profile obtained with the proposed method in the high energy spectrometer, camera C3.

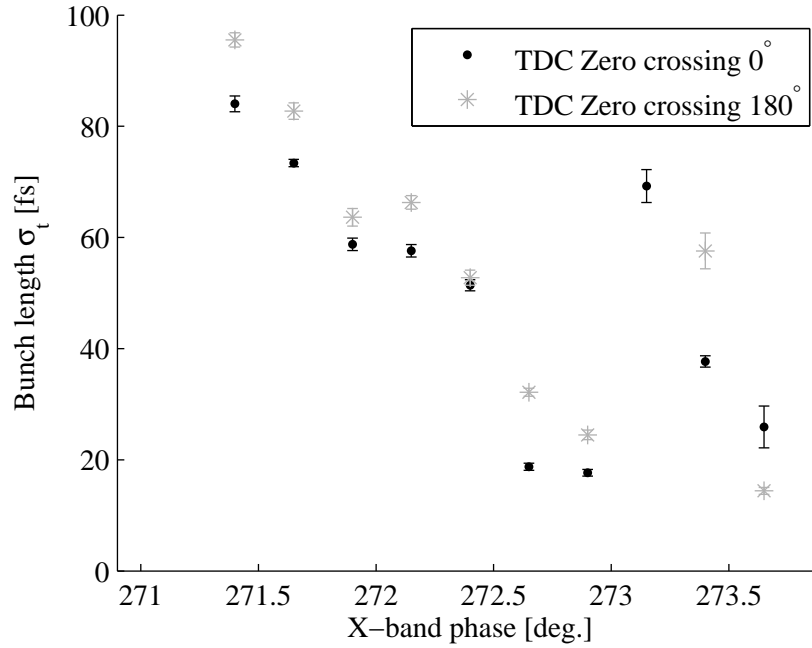


Figure 4.11 – The measured bunch length with the proposed method, using the TDC. Mean and standard error of 10 acquired bunch lengths are presented.

length. It was shown in chapter 3 that close to maximum compression, the X-band RF phase may be used to tune the bunch length. In the data of Figure 4.11, the X-band phase was scanned in 10 steps where the highest X-band phase was thought to be the shortest bunch length. In the presented data-set, the compression was varied approximately between 100 fs and 20 fs. The bunch length was measured at both zero crossings of the TDC phase. The bunch lengths at the phases 271.4 until 272.9 degrees are as expected. However, the bunch

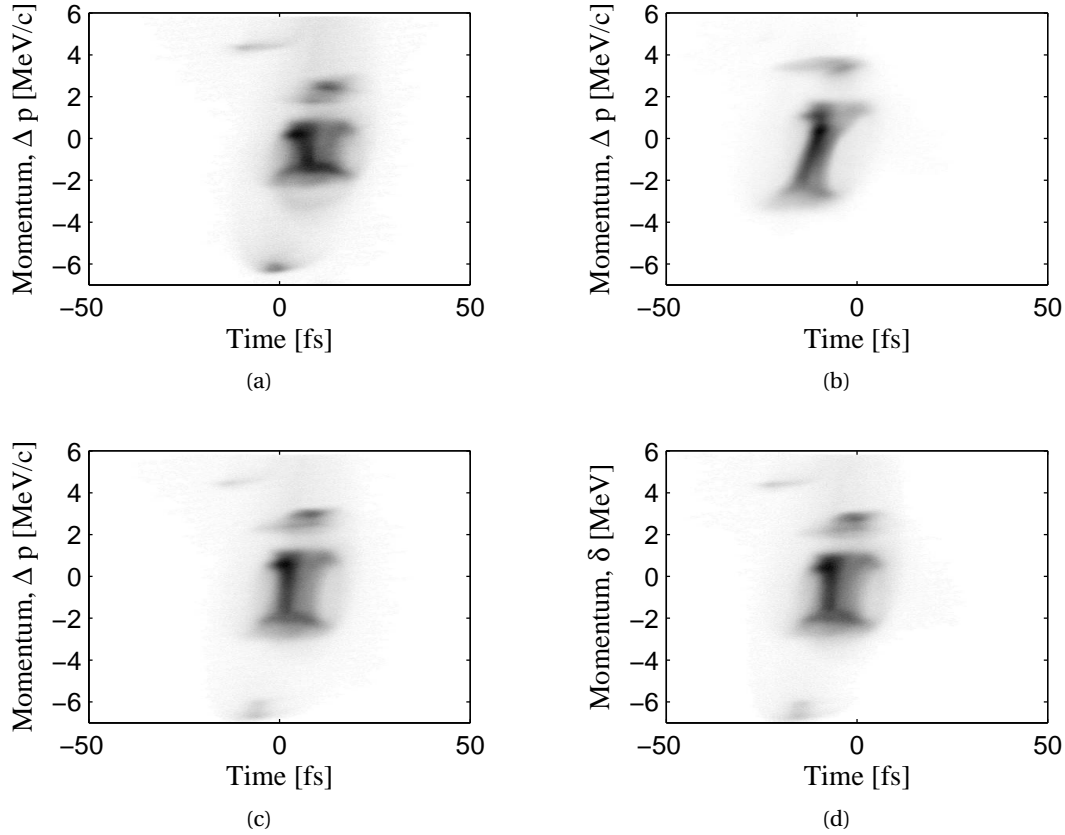


Figure 4.12 – Observed subsequent longitudinal phase space images showing the variability in the charge density on screen C3, disabling us to subtract the intrinsic from the streaked beam.

lengths at 272.9 until 273.7 are overestimated and have large error bars. The explanation lies in the variation of the longitudinal phase space of the intrinsic (non-streaked) longitudinal phase space. The longitudinal phase space varies from shot to shot, as can be seen in the longitudinal phase space images shown in Figure 4.12. Since the proposed method relies on comparing the streaked with the intrinsic image, the projected momentum space must have the same momentum versus charge profile. Due to space charge effects, this cannot be guaranteed, leading to an overestimation and large errors in the measured bunch length.

A solution to the problem is to assume the unstreaked beams' average ($\langle y_{intrinsic} \rangle$) in Figure 4.1) to be zero for all momentum slices. The result for $\Delta T = \langle y \rangle B$, in which the centre of mass $\langle y \rangle$ is calculated for both zero-crossings (0° and 180°) and the unstreaked (intrinsic) beam is shown in Figure 4.13. Firstly, it is observed that the overestimation and large error bars at the smallest bunch lengths have been corrected. Secondly, it can be seen that the bunch length obtained from the 180° zero crossing is systematically overestimated. Besides the streaked bunch lengths, the figure also shows the intrinsic bunch lengths, which is essentially the intrinsic $\delta, \langle y \rangle$ correlation at the high energy spectrometer screen. Because it is unknown how the intrinsic image is orientated and which correlations $\delta, \langle y \rangle$ are present in the longitudinal

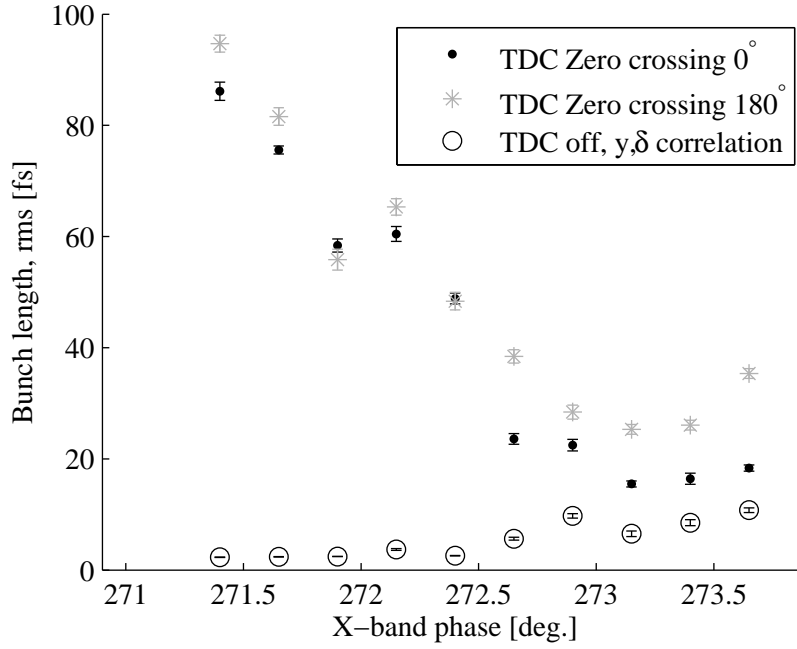


Figure 4.13 – The measured bunch length with the proposed method, using the TDC. Mean and standard error of 10 acquired bunch lengths. The same data as in Figure 4.11 is used.

phase space, the intrinsic beam size cannot be added or subtracted.

Bunch length simulations suggest that a linear curve of bunch length versus X-band phase is expected at both sides of the minimum bunch length, as confirmed by [46] and chapter 3, Figure 3.9. It was concluded that the minimum bunch length is limited by longitudinal space charge. A detailed scan of experimental determined TDC bunch length versus X-band phase may be seen in Figure 4.14 and 4.15. The difference between the figures is the TDC zero crossing implemented in each case. A change of TDC phase of 180 degrees means that the head and tail are kicked in opposite directions. The X-band RF phase was varied between 267.7 deg. and 274.2 deg. in 100 steps. The intrinsic beam size was not recorded, and therefore could not be added or subtracted to the streaked beam size. The $y_{intrinsic}$ was considered to be constant, i.e. zero.

The data in Figures 4.14 and 4.15 also include the simulations presented in chapter 3. At long bunch lengths the simulations fit well to the measured bunch length. However, at the shortest bunch lengths the TDC measurements do not agree with the simulated bunch length. It is unknown which measurement is correct since no other bunch length measurement is available to cross-check the results. The minimum bunch length is on the left hand side of the valley (roughly 270.5 deg.) after which a plateau follows. This feature occurs in both the simulations and in the experiments. The two experimental measurements show a disagreement at the smallest bunch length, for which three possible explanations are possible. Firstly, the electron beam may have a y,t correlation at the TDC meaning a y',t correlation at the high energy

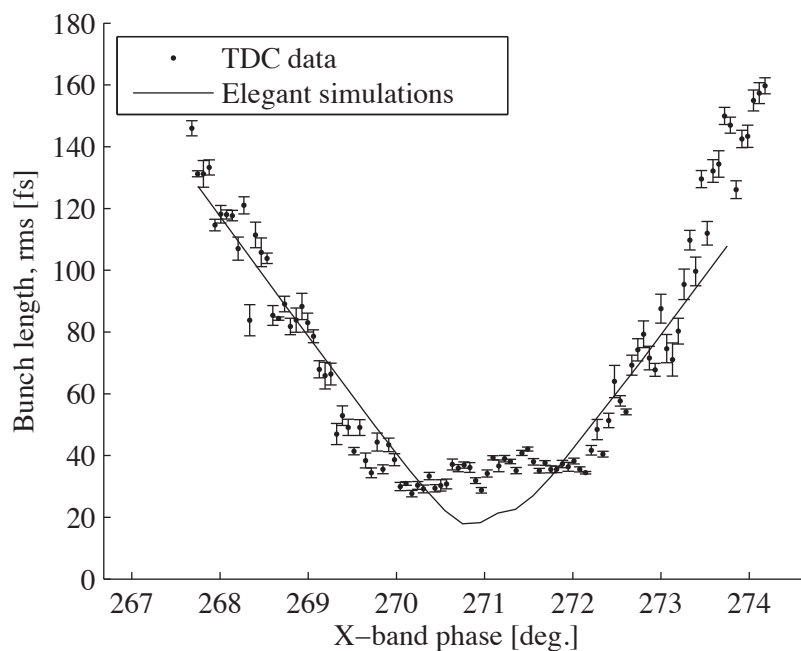


Figure 4.14 – The measured bunch length with the proposed method, using the TDC. Mean and standard error of 5 acquired bunch lengths, TDC 0° .

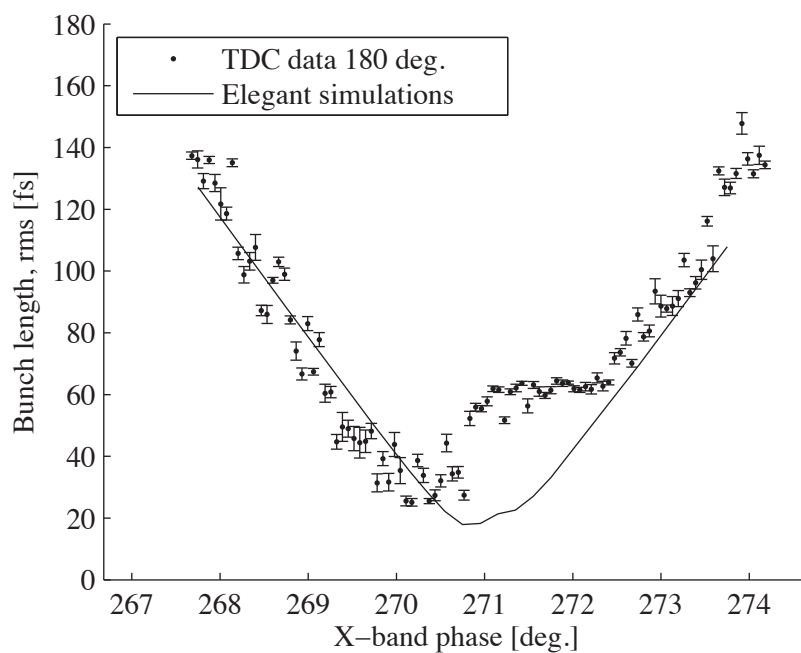


Figure 4.15 – The measured bunch length with the proposed method, using the TDC. Mean and standard error of 5 acquired bunch lengths, TDC 180° .

spectrometer [47]. The y, t correlation means that the electron beam enters the TDC with an angle. This angle may have been created by CSR in the last bunch compressor magnet or before the TDC. Secondly, this disparity may be removed by recording the intrinsic beam size. In the measurements, the intrinsic beam size was not recorded and thus could not be subtracted. Finally, other higher order effects from the TDC cannot be accounted for in the presented method, such as longitudinal fields in the TDC or other fields other than the fundamental mode.

The simulation performed (see Figure 4.10) estimated the rms bunch length well. The simulations show that a minimum bunch length of 19.5 fs is expected (see Figure 4.14 and 4.15). The minimum bunch lengths measured experimentally were 27.7 fs and 24.5 fs rms, depending on the TDC zero crossing used.

4.6 Discussion

4.6.1 Bunch length and resolution

Conceptually, the minimal bunch length that may be measured depends on how accurately the mean in a slice can be determined and the dispersive resolution. The schematic in Figure 4.16 shows the principle. The left hand schematic shows the high energy spectrometer with (solid line) and without (dashed line) TDC on. The right hand figure is obtained where the intensity in a slice is plotted versus the vertical position from both the streaked and intrinsic image. From both the streaked and intrinsic slice the mean (or in other words the centroid or centre of mass) $\langle y_{intrinsic} \rangle$ and $\langle y_{streaked} \rangle$ are calculated. With the centroid deflection the time ΔT can be calculated, according to Equation 4.1. In the presented analysis method, the slice's intensity width is neglected, thus assuming a similar intensity profile. The minimal detectable bunch length possible thus depends on how accurately the centroid can be determined and may be smaller than the intrinsic beam size. The rms temporal resolution of the measurement becomes:

$$\sigma_t = (\Delta T_{max} - \Delta T_{min}) \frac{\sigma_{\delta, slice}}{\sigma_{\delta, beam}}, \quad (4.2)$$

where $\Delta T_{max} - \Delta T_{min}$ is the spread in which the times ΔT occur, $\sigma_{\delta, slice}$ the intrinsic rms beam size in the dispersive direction (also called the betatronic beam size [48]) and $\sigma_{\delta, beam}$ the dispersive beam size in the magnetic spectrometer. In order to increase the resolution of the method, the resolution in the dispersive domain must be increased. This may be done by focussing in the dispersive direction to generate a smaller intrinsic beam size or increase the dispersive streak. Since the energy spread will cover a larger spot on the scintillator, the field of view of the camera must be enlarged. Since the momentum spread $\sigma_{\delta, beam}$ and the intrinsic beam size $\sigma_{\delta, slice}$ should remain similar towards smaller bunch lengths, the number

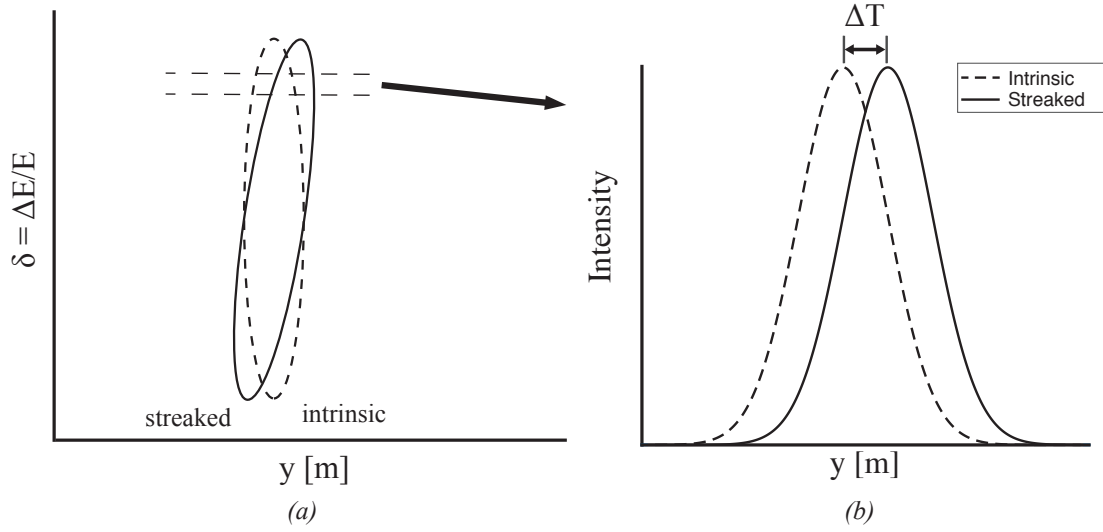


Figure 4.16 – Schematic of (a) the longitudinal phase space of a streaked and intrinsic electron beam and (b) a slice from the longitudinal phase space with the time ΔT indicated.

of measurements remains the same but occurs in a shorter period of time. This leads to an enhancement of the resolution towards smaller bunch lengths.

4.6.2 Advantages and disadvantages

In the proposed measurement the intrinsic beam size is omitted and the bunch length is directly measured. In the conventional method the projected bunch length may be deconvoluted with the intrinsic beam size to increase the accuracy. However, this method does not take the variation of the beam size along the bunch into account, i.e. the beam size in y has a correlation with both the momentum and the time domain (see e.g. Figure 4.3 where the beam size changes along the momentum axis). The method proposed in this chapter omits the beam size correlation along the electron bunch, allowing for a more accurate reconstruction of the bunch length.

Apart from omitting the beam size versus the momentum correlation, the proposed method also corrects for the y, δ correlation at the high energy spectrometer. Several authors have been addressing the problem of measuring a different bunch length at the other zero-crossing of the TDC (zero crossing + 180 deg.) [49]. The method described here removes the y, δ correlation because the intrinsic beam $y_{intrinsic}$ is subtracted. However, the y', t correlation, higher order effects and other modes in the TDC are not corrected for. For example a longitudinal field in the TDC may be present, accelerating part of the electron bunch and decelerating another part. The particle will thus end up in another slice, thereby giving incorrect results. The longitudinal phase space may also be non-linearly compressed. Although no results have been presented in this chapter, the method proposed is also applicable in non-linearly compressed beams.

A drawback of this proposed method is that a correlated energy spread is needed. The energy spread is required in order to enhance the number of measurement points. The beam should also not be present twice in a momentum slice $\Delta\delta$, e.g. the head and tail should not have the same energy.

It was also shown that the intrinsic beam size could not be subtracted in space charge dominated beams due to the large fluctuations present in the projected momentum spread at the high energy spectrometer. Although the intrinsic beam size could not be subtracted, the measurements were considered reliable due to the limited δ, y correlation in the intrinsic beam.

4.6.3 Side notes on the measurements, optics

Due to space charge effects the Beta-functions could not be matched at high compressions. For this reason the Beta-functions were matched with a long bunch (2.7 ps rms), after which the magnetic optics after the bunch compressor were unchanged during the remainder of the experiment. This procedure led to the discovery of the proposed analysis method, to omit the optics and be able to measure bunch length in a space charge dominated beam.

4.7 Conclusions

A bunch length method has been proposed and proven to measure bunch length in space charge dominated beams. This method was proven to be successful with simulations as well as with experiments. In simulations the bunch length at the high energy spectrometer with the proposed method was similar as the real bunch length in the non-dispersive section. The experimental data corresponds very well to that obtained from the simulations. The minimal bunch length from experiments and simulations are of the same order (19.5 fs in simulations to 24.5 fs in the experiment).

Although the method is promising, conditions such as a large correlated energy spread are required. The bunch length method is independent of the transverse beam size along the bunch and removes the y, δ correlation at the high energy spectrometer. The resolution depends on the intrinsic beam size and the streaked beam size in the dispersive direction. The resolution enhances as the bunch length becomes shorter.

If this method could be implemented, the power needed in the transverse deflecting cavities may be reduced, reducing cost as well as the harmonic mode, i.e. instead of X-band (12 GHz) a C-band (5.7 GHz) may be used.

5 Measurement of Optical Transition Radiation Spectrum

The second chapter of this thesis described how optical transition radiation (OTR) was generated. This chapter describes how the OTR light is transported out of the vacuum and analysed using an optical spectrometer. Firstly, the transport of the OTR radiation from the OTR foil into the optical fibre or onto the optical spectrometer reference camera is discussed. The second section discusses the optical spectrometer, in particular its characterisation and resolution. An experimentally obtained OTR spectrum is compared with a theoretical OTR spectrum in the third section. The signal as a function of charge for both incoherent and coherent spectrometer signals is described in the same section.

5.1 OTR radiation collection setup

All experiments presented were performed at the SwissFEL Injector Test Facility (SITF) [41]. The OTR spectrometer setup is located between the bunch compressor and the high energy spectrometer. Figure 5.1 shows a schematic of the SITF with the relevant equipment. The setup with which the OTR light is collected is located 7.3 m downstream of the bunch compressor and 13.4 m before the high energy spectrometer. A detailed schematic of camera C4 and the spectrometer is shown in Figure 5.2. A corresponding photograph of this setup is shown in Figure 5.3.

Optical transition radiation is generated on an aluminium coated silicon wafer (No. 1 Fig. 5.2) [50]. Due to the 45 degree angle of the wafer, the OTR radiation is emitted perpendicular to the beam direction in a narrow cone (see chapter 2). For the generation of OTR the thickness of the OTR foil is unimportant. However, due to the radiation loss downstream of the OTR foil, the wafer is chosen as thin as possible, with a thickness of 300 μm . The vertical and horizontal dimensions are 20 mm by 20 mm. Silicon was chosen because of its flat wafer properties creating a flat aluminium surface and thus a flat electromagnetic mirror.

The vacuum window in position no. 2 is a quartz SiO_2 vacuum window. The vacuum is of the order of 10^{-9} mbar, with the mirror setup positioned in ambient air. The transmission

Chapter 5. Measurement of Optical Transition Radiation Spectrum

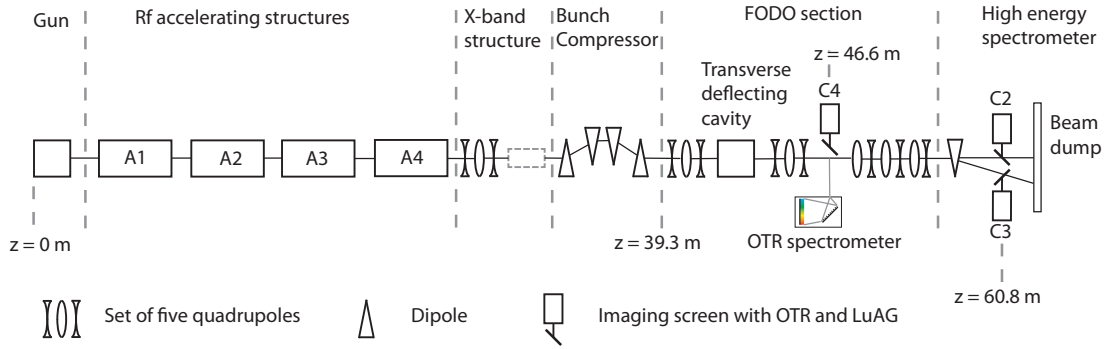


Figure 5.1 – Schematic overview of the SITE. The z positions are relative to the surface of the cathode in the gun.

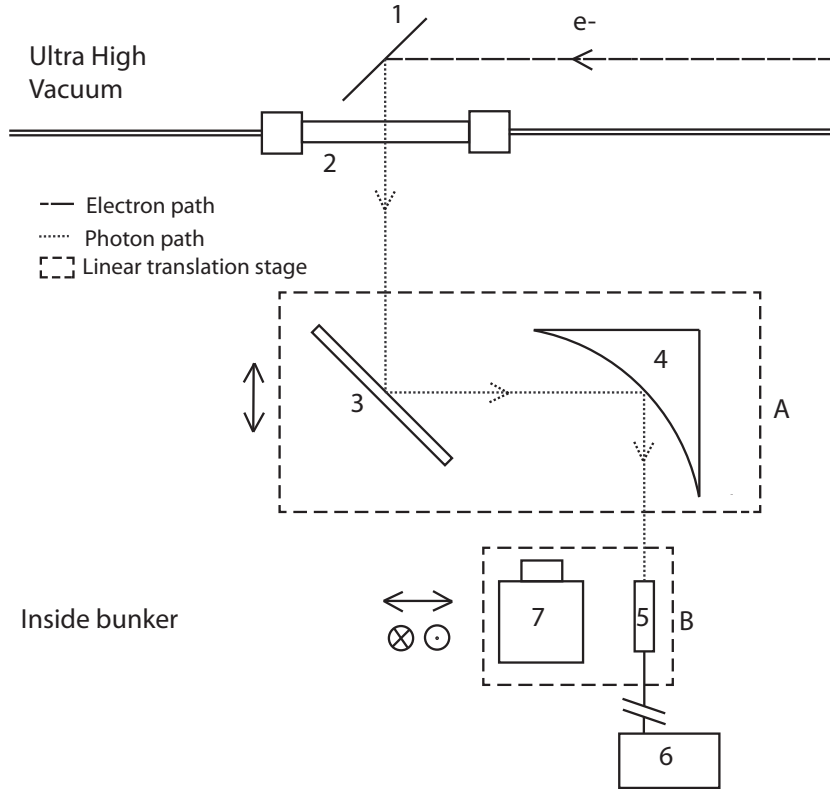


Figure 5.2 – Systematic overview of the optical part of the spectrometer setup. 1. OTR wafer, 2. Vacuum window, 3. Flat mirror, 4. Off-axis parabolic mirror, 5. Optical fibre, 6. Optical spectrometer, 7. Camera C4. A and B are linear translation stages to focus and align the camera. After the alignment has been verified with the camera, stage B is positioned to focus the beam into the optical fibre.

curve of the vacuum window is shown in Figure 5.4 [51]. The vacuum window is installed perpendicular to the beam direction.

Optics capable of a wide frequency bandwidth were chosen to guide the OTR light into the

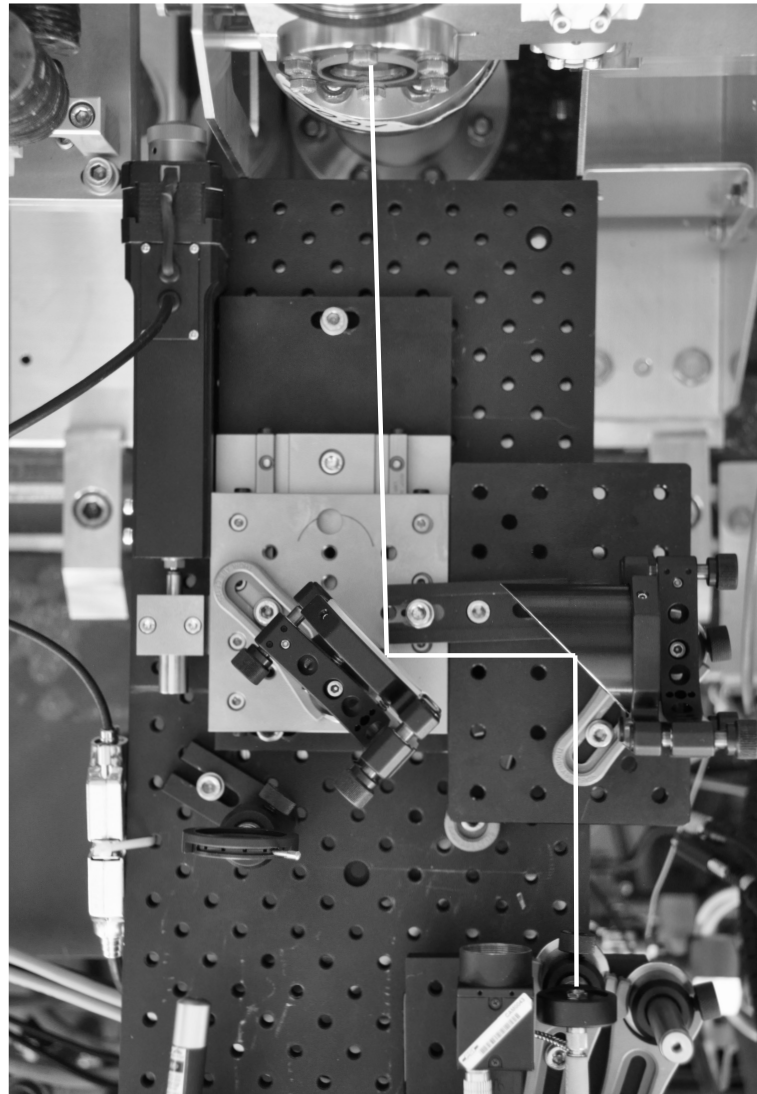


Figure 5.3 – Photo of the OTR radiation collection setup.

optical fibre. Mirrors were used instead of lenses to avoid chromaticity effects because of the wide spectral band range of the optical spectrometer. Figure 5.5 shows the reflectivity curve of the flat mirror and the off-axis parabolic mirror. The first mirror (No. 3) is a flat fused silica substrate, coated with a deep UV enhanced coating, the diameter of the mirror is 50 mm with a surface flatness of 63.3 nm. The focusing mirror (No. 4) is a off-axis parabolic mirror, the designed deflection angle is 90 degrees with a focal distance of 10.16 cm (4 inches) from the surface, assuming a parallel photon beam is coming in. The mirror surface is aluminium coated to reflect wavelengths down to 220 nm, the deviation from the design surface of the off-axis parabolic mirror is shown in Figure 5.6. The measurement was performed using a phase shifting interferometer (Zygo Verifire ATZ) which emits laser light at 633 nm. The reflected beam from the analysed mirror surface is returned to the apparatus and phase analysed using interferometry between the original and reflected beam. The thickness variation across the

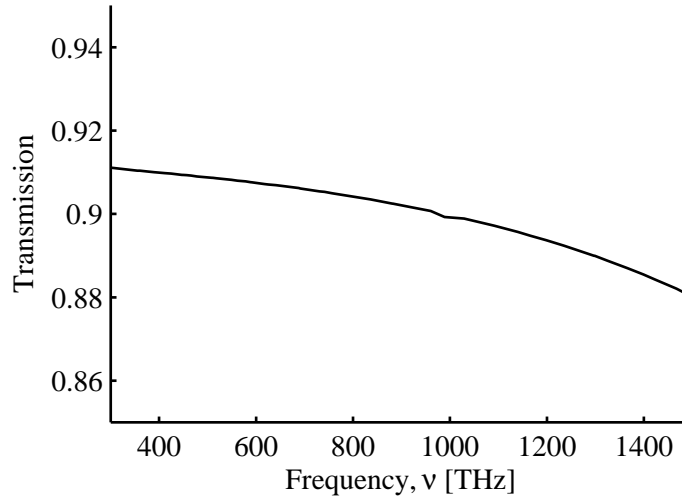


Figure 5.4 – Transmission curve of the silica vacuum window, taken from [51].

mirror surface is maximally 175.5 nm.

The light is focussed into a radiation hard optical fibre. The silica fibre diameter is 230 μm , two meters long with a stainless steel jacketing. The bare entrance of the fibre is thus 230 μm , with an angular acceptance of 22.8 degrees in ambient air. The optical fibre can be connected to the spectrometer using an SMA connector.

Three linear stages are installed to direct the OTR light into the optical fibre and camera. Translation stage A in Figure 5.2 is used to bring the beam into focus and is movable in one direction. Translation stage B is used to switch between the camera and the optical fibre. Translation stage B is also used for fine-tuning of the light onto the camera and fibre. Translation stage B consists of two linear translation stages which allow it to be moved vertically and horizontally, as indicated in Figure 5.2.

A Point Grey Flea camera, FL2-08S2M-C is installed at Position 5. The camera is mono-colour (i.e. black and white), with a Sony ICX204AL CCD detector. The pixels are 4.65 μm in both the horizontal and vertical directions. The number of these pixels is 1032×776 , resulting in a chip size of 5.8 mm horizontally and 4.92 mm vertically. The number of active pixels is 1024 by 768 due to the bad characteristics of the edge pixels. The analog to digital converter is 12 bit. The synchronisation is triggered by the master clock of the accelerator. In all experiments the integration time is set to 10 ms. Figure 5.7 shows the sensitivity curve of the CCD sensor [53].

Figure 5.8 shows the transverse photon distribution profile at the entrance of the optical fibre, taken with camera C4. The beam distribution shows a tail towards the right side of the peak. Off-axis parabolic mirrors are designed to focus a parallel beam onto the focal spot. Due to the origin of the radiation, which is optical transition radiation, the incoming photons are divergent (see chapter 2). The divergent beam creates an astigmatism that cannot be

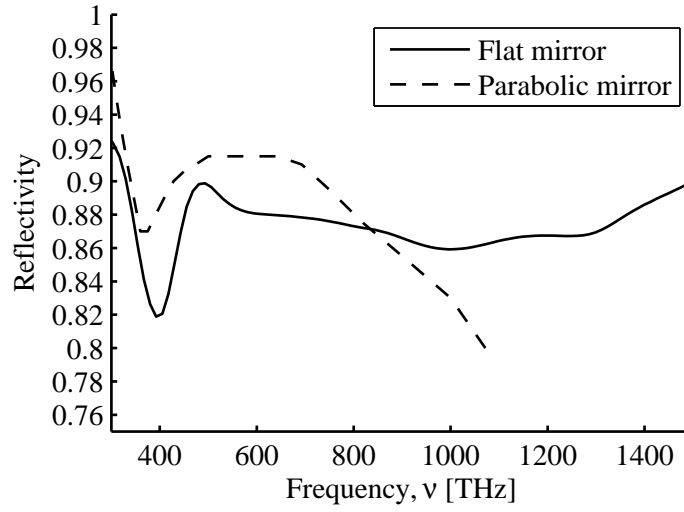


Figure 5.5 – Reflectivity curve of the flat mirror and the off-axis parabolic mirror, taken from [52]. No parabolic mirror data was available after 1100 THz.

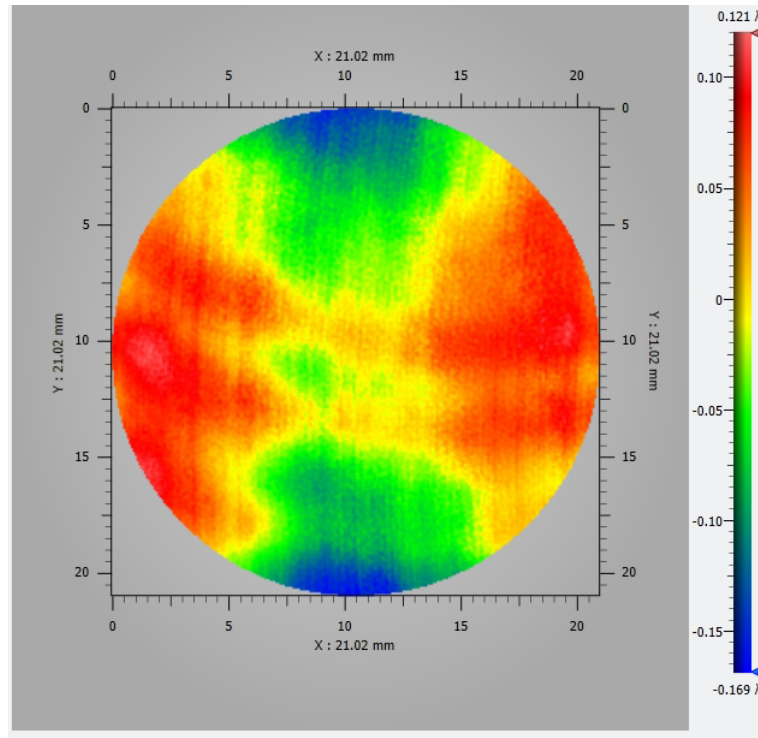


Figure 5.6 – Off-axis parabolic mirror flatness, analysis wavelength $\lambda = 633$ nm. Courtesy of V. Thominet.

removed. Contributing to the angular divergence is the fact that every electron creates an angular distribution with a maximum at $\frac{1}{\gamma}$. In the case of a divergent or convergent electron beam, the assembly of electrons introduces an additional divergence component.

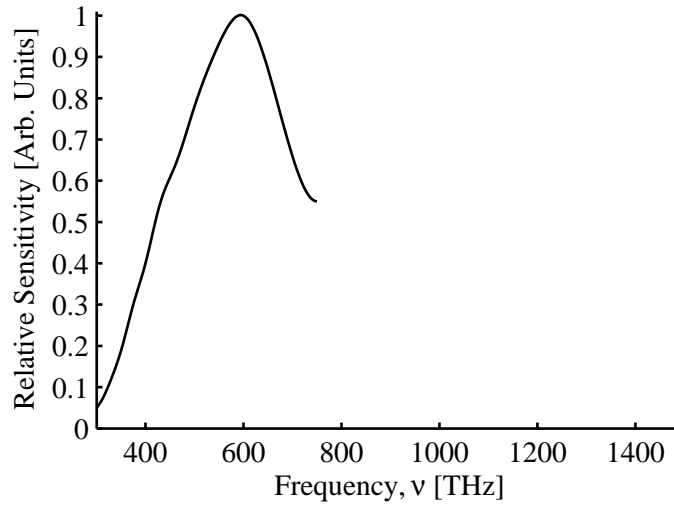


Figure 5.7 – Sensitivity of the ICX204AL CCD sensor [53]. Data was available from 300 THz to 750 THz. The curve does not include the micro-lenses mounted onto the CCD and the anti-reflective window.

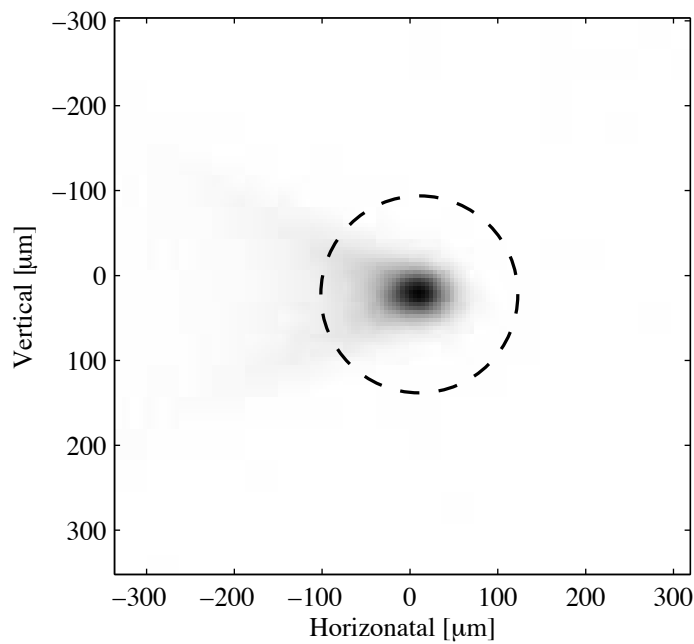


Figure 5.8 – OTR photon distribution profile at the entrance of the optical fibre, the dashed circle guides the eye to the entrance size of the optical fibre. The image was taken from an uncompressed 200 pC beam.

5.2 The QE65000 Spectrometer

The optical spectrometer used at Position 6 is an OceanOptics QE65000. The spectrometer was chosen for its high detector sensitivity (see Figure 5.10).

The optical bench design is a 4-f symmetric imaging system. Figure 5.9 shows a schematic of the imaging system. The focal length of the mirrors is 10.16 cm (4 inches), with $f_1 = f_2$. Both mirrors are aluminium coated, for the best reflectivity over the whole spectral range. The magnification of the object to the imaging plane is one. The slit, which is imaged onto the CCD (Charged Coupled Device), is $100\ \mu\text{m}$ wide. The grating, located at the Fourier plane of the imaging system, has $300\ \text{lines mm}^{-1}$. The resulting spectral range is 316 THz (950 nm) to 1500 THz (200 nm).

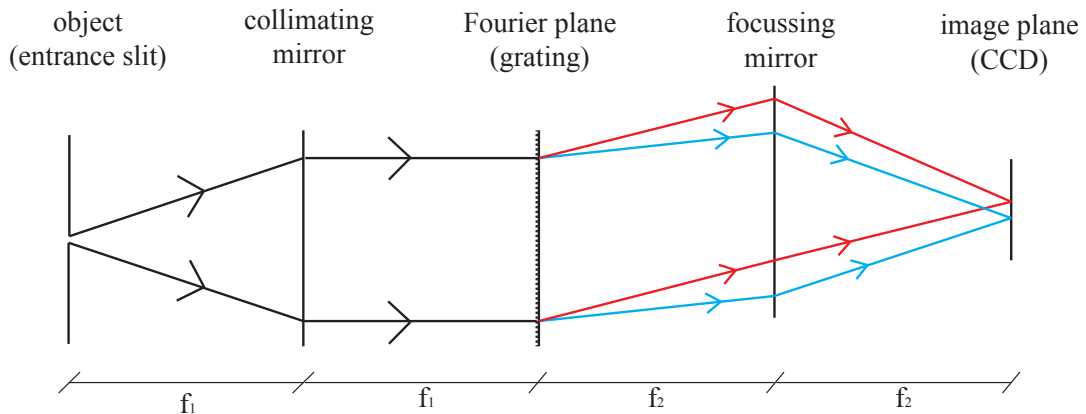


Figure 5.9 – The free space part of the optical spectrometer which is enclosed in a box. The grating is installed in a reflective geometry.

The CCD is a Hamamatsu S7031-1006 Full Frame Transfer (FFT) CCD. The FFT means that all charge collected by the CCD is transferred in the dead time of the detector, i.e. non-integrating window. The pixel size is $24.6\ \mu\text{m}$ with 1044 pixels horizontally in the dispersive direction and 64 pixels in the vertical direction. The effective area is 1024 pixels by 58 pixels. The detector sensitivity is 0.02 femto-joule per count at 250 nm. Before the detector a patented interference filter mounted on a wafer is installed [54]. The filter is used to eliminate second order effects from the spectrum.

The $100\ \mu\text{m}$ slit gives a resolution of 3.44 nm FWHM at the detector, corresponding to 1.46 nm rms. The dark noise is 2.5 counts rms, which is significant since the signals presented are weak. The minimal integration time is 8 ms. Using the external trigger the minimal time between triggers is 19.1 ms, thus should be able to store data at 10 Hz. However, due to the additional time needed to transmit the data from the spectrometer to the computer, the maximum data storing rate of the optical spectrometer is limited to 5 Hz.

5.2.1 Radiometric calibration

In order to determine the absolute number of photons or energy, an absolute energy per unit area, $\text{J THz}^{-1} \text{cm}^{-2}$ at a certain point must be known. Given a certain area and spectral band in the spectrometer, every spectral pixel can be labelled with a joule per count.

Chapter 5. Measurement of Optical Transition Radiation Spectrum

The light source DH-2000-CAL is calibrated in the spectral domain of the QE65000. The calibration source consists of two pre-calibrated light bulbs, a Deuterium and Halogen light source respectively. The calibration curve spans the frequency domain of 286 THz (1050 nm) to 1364 THz (220 nm). The spectrometer covers the 316 THz (950 nm) to 1500 THz (200 nm) domain, thus we lose 136 THz because of unavailability of the calibration curve in the ultra-violet domain. The loss in spectral data is not considered critical because the resolution of the spectrometer is larger in the infra-red domain (see next section).

The calibration source DH-2000-CAL comes with an SMA output. The calibration is dependent on the input of the optical fibre. A change of the optical fibre will correspondingly change the calibration. Figure 5.10 shows the calibration curve for the QE65000 spectrometer together with a 230 μm radiation hard optical fibre.

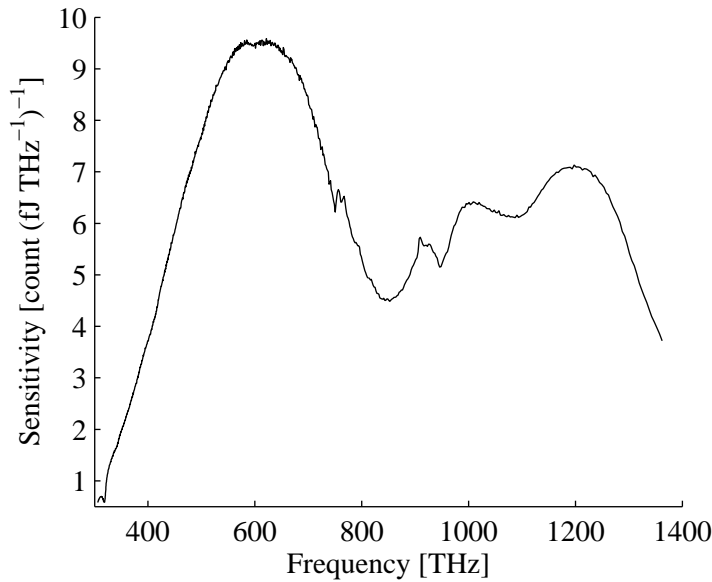


Figure 5.10 – Sensitivity of the QE65000 spectrograph. Radiation source: DH 2000.

5.2.2 Spectrometer resolution

The spectrometer's bins are linearly spaced in the wavelength domain. The resolution of the spectrometer is 3.3 nm FWHM (1.46 nm standard deviation). The spectral resolution in the frequency domain is given by:

$$d\nu = \frac{c}{\lambda^2} d\lambda \quad (5.1)$$

where c is the speed of light in vacuum, λ the central frequency of the bin and $d\lambda$ the spectral resolution. Figure 5.11 shows the resolution versus frequency. The resolving power is highest

in the infra-red (400 THz) domain and decreases with the square of the frequency. In the wavelength domain the bins are linearly distributed. Hence in the frequency domain, the bins were linearly distributed by interpolation of the signal. The accuracy of the interpolation depends on the original bin size and the interpolated bin size. The spectrometer resolution $\Delta\nu$ at 316 THz is 0.26 THz, the total range of the spectrometer is 316 THz to 1500 THz. In order to avoid data loss at low frequencies the $\Delta\nu$ was chosen to be 0.13 THz, resulting in a minimum number of interpolation points of 11,600 over a frequency range of 1184 THz. In Matlab a piecewise cubic interpolation was used with a number of 20,000 points.

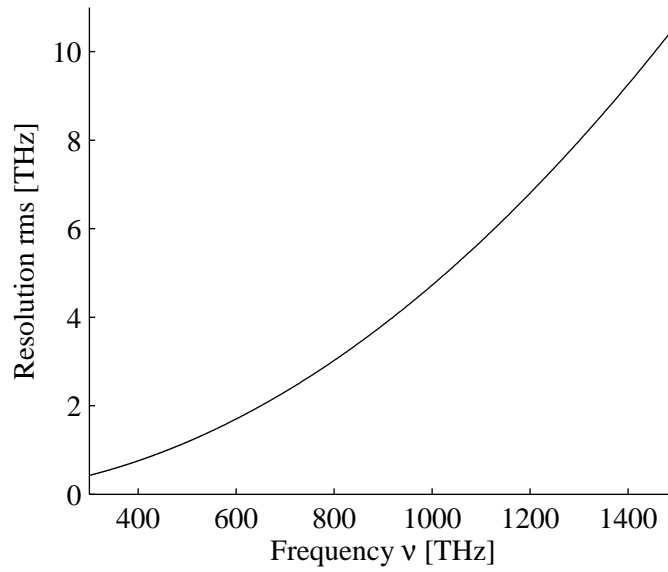


Figure 5.11 – Spectrometer resolution according to Equation 5.1

5.3 Incoherent and coherent spectra

Acquiring spectra with the optical spectrometer required the accelerator to be set similarly to the normal setup (see sections 3.4 and 3.5). Hence, the accelerator was firstly setup such that the longitudinal phase space could be measured as described in chapter 4. In order to focus the electron beam onto the OTR foil at camera C4, all quadrupoles in the FODO section are cycled (demagnetised) and set to zero. The transverse beam size at camera C4 (Figure 5.1) is reduced using the first three quadrupoles in the FODO section.

5.3.1 Incoherent radiation

The single particle spectral response of optical transition radiation is independent of frequency (Equation 2.14). The equation is valid for a long bunch in which the observed visible light shows no coherence effect.

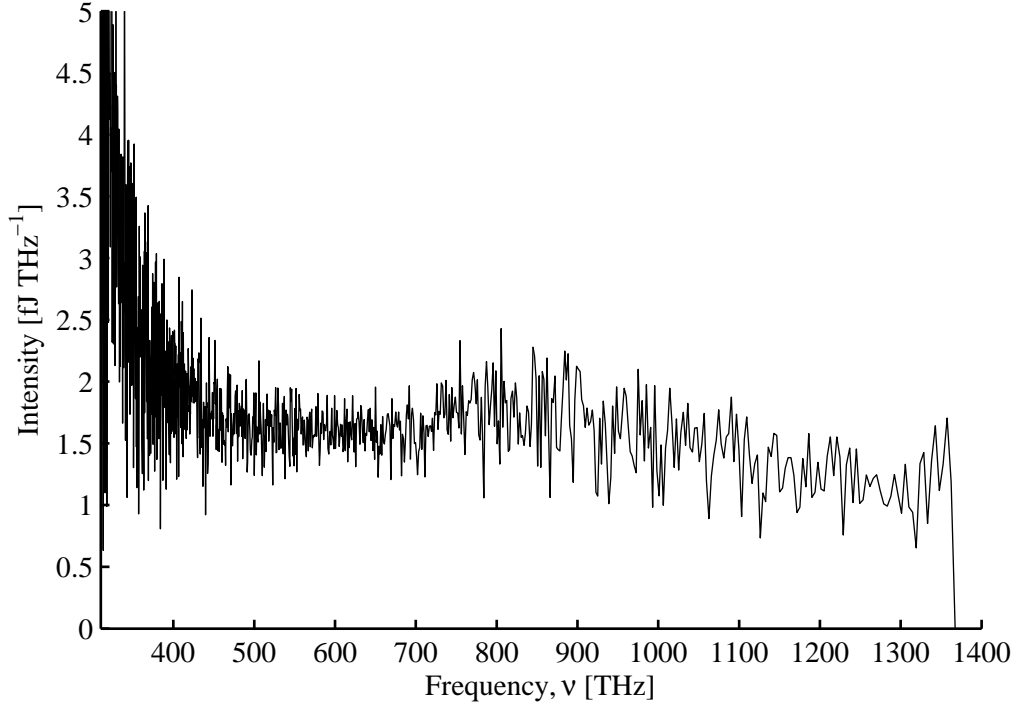


Figure 5.12 – Single shot spectrum from an uncompressed bunch, 105 pC.

A single shot OTR spectrum is shown in Fig. 5.12. The OTR spectrum is flat as expected from OTR theory, i.e. no dependence on the frequency or wavelength. Since the detector has a low sensitivity towards long wavelengths, the signal to noise ratio decreases towards lower frequencies (see Figure 5.10). Correspondingly, the spectral resolution becomes higher towards lower frequencies as shown in Figure 5.11.

The expected OTR intensity per frequency is given by Equation 2.14. The calculated intensity is 1.9 fJ THz^{-1} of a 200 MeV and 105 pC electron beam. Taking into account the vacuum window and the mirror reflectivity as presented in the previous sections, the corrected intensity is 1.4 fJ THz^{-1} .

The spectral power, as described in chapter 2 of OTR may be described as:

$$\frac{dP(\omega)}{d\omega} = \left| \frac{dW}{d\omega} \right|^2 [N + (N^2 - N)F(\omega)] \quad (5.2)$$

If the bunch length is long and thus no coherence is present at the detected frequency, the

form factor becomes zero and hence the above equation reduces to:

$$\frac{dP(\omega)}{d\omega} = \left| \frac{dW}{d\omega} \right|^2 N \quad (5.3)$$

In which the radiated intensity is linearly proportional to the charge. The linearity of the spectral intensity on the charge can be seen in Figure 5.13. The charge was varied using scrapers in the bunch compressor. This method was preferred over others since the method using the scrapers does not amend the β -functions. The charge was measured using BPMs, which are in turn calibrated to ICTs and Faraday cups. The BPM used for the charge measurements is the second BPM after the bunch compressor. The error on the charge measurement was not included in the plot since the standard error on the charge measurement was 50 fC.

Besides the spectra, the OTR intensity on camera C4 was also measured. The underestimated spectral intensity measurement at 108 pC is likely an alignment failure of the photon beam on the optical fibre or a failure in the scraper values written to the motors. Both the intensity data from the camera and the optical spectrometer are proportional to the charge.

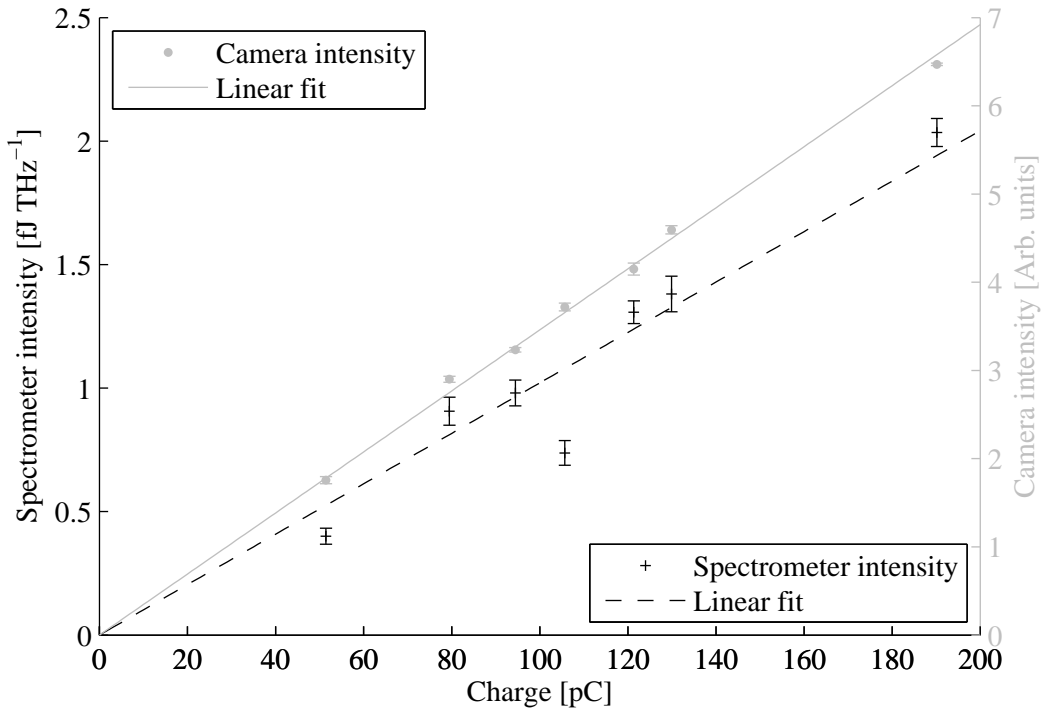


Figure 5.13 – Spectral intensity versus charge at 600 THz (500 nm) of incoherent spectra for a compressed bunch. The solid and dashed lines guide the eye to a linear fit of the data. The error bars show the standard error. Bunch charge was reduced using scrapers in the bunch compressor.

5.3.2 Coherent radiation

Under longitudinal compression, the spectra show a coherence effect in the low frequency domain of the spectra. The data in Figure 5.14 is an example of a coherence effect observed under such compression. In comparison to the spectra of the uncompressed bunches, an increase in spectral intensity is observed towards lower frequencies. In order to prove the spectral increase is a coherence effect, the spectral intensity must be monitored as a function of charge.

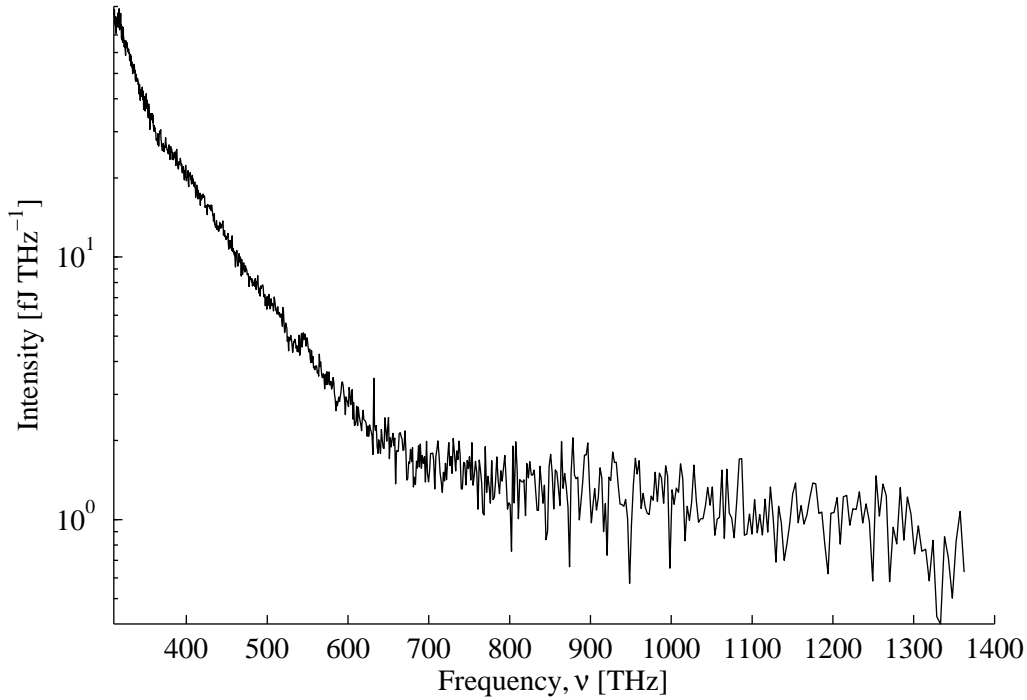


Figure 5.14 – Single shot spectrum from a compressed bunch.

In incoherent transition radiation the collected radiation intensity is proportional to the number of electrons. It is proportional to the square of the number of electrons in coherent OTR. However, the spectra acquired in our measurements are not fully coherent and also not fully incoherent. Rewriting Equation 2.22 gives:

$$\frac{dP(\omega)}{d\omega} \propto (1 - |F(\omega)|^2)N + |F(\omega)|^2 N^2 \quad (5.4)$$

It is thus expected that the power as a function of the current (or number of electrons N) follows a second order polynomial. The charge dependence was measured at screen C4. Charge reduction can be established by modifying the transverse radius of the laser profile on the cathode. By reducing the diameter of the laser the same transverse space charge density is

present. However, there is a coupling between the transverse beam size at the cathode and the bunch length measured at the high energy spectrometer. Therefore the bunch length was compensated by the X-band phase. OTR was collected with the camera as well as with the optical spectrometer. Figure 5.15 shows the measured BPM charge versus camera intensity and spectral intensity.

The camera integrates the intensity over the spectral range from 400 THz to 750 THz whereas the spectrometer's intensity was recorded at a frequency of 375 THz. The data in Figure 5.15 shows that the measured intensity with the camera and the optical spectrometer agree very well. Moreover, the second order polynomial fit agrees well with the measured data. For both fits, the offset was set to zero, thus only a linear and a quadratic component were used, in accordance with Equation 5.4.

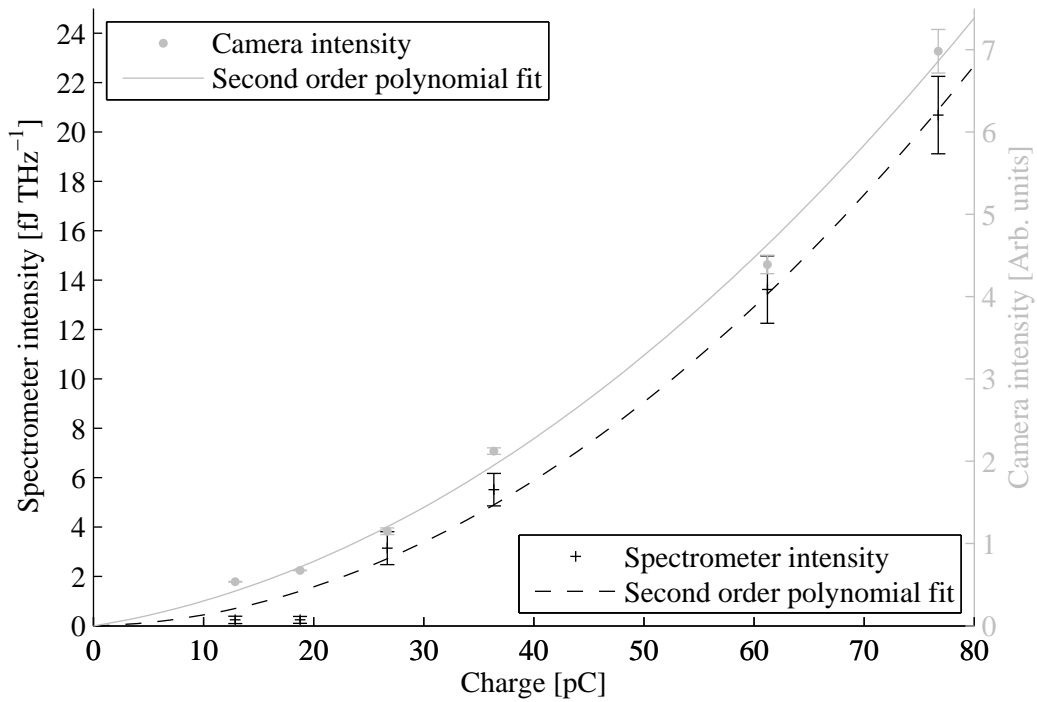


Figure 5.15 – Charge scan of Optical Transition Radiation at the entrance of the optical fibre. Taken with the camera positioned at Position 7 (Figure 5.2). The analysed spectrometer frequency was 375 THz

It was impossible to use the scrapers in the bunch compressor to reduce the charge, as was performed with the incoherent radiation. The reason lies in the origin of the coherence effect. In order for the radiation to reach the visible radiation domain, the bunches must be either very short or the electron bunch must feature spikes or a modulation on the temporal profile. Experiments suggest that the coherent radiation comes from a substructure on the bunch rather than a single spike or spikes. The reason why the scrapers could not be used to reduce bunch length was that if the space charge dominated sections were removed from the profile, with the scrapers in the bunch compressor, the coherence effect disappeared or partly

disappeared.

Ratner *et al.* observed a similar gain in a visible frequency domain [55, 56]. The spectral gain was caused by microbunching originating from a linear achromat. A perfect linear achromat is a bending system consisting of quadrupoles and dipoles after which no residual dispersion is present in the beam. Longitudinal space charge starting from shot noise was established as the cause of the microbunching. In our case longitudinal space charge effects cannot be neglected, as was discussed in chapter 3.

Although synchrotron radiation in the bunch compressor has been included in the Elegant simulations, no effects have been observed that suggest the involvement of Coherent Synchrotron Radiation (CSR) in the microbunching. However, it was concluded by Derbenev *et. al* [57] that CSR may have an effect on the radial emittance. Because the emittance was blown up towards high compressions CSR may have played an important role in the bunch compressor chicane. Moreover, Derbenev *et. al* recognised the fact that the net electron energy loss due to synchrotron radiation is a reduction of the average momentum of the electron bunch. Space charge effects, on the other hand, should not change the average momentum but increase the energy spread as a whole.

In order to test if CSR effects are acting on the electron beam, the centre of mass momentum at the high energy spectrometer was recorded. The data in Figure 5.16 shows the centre of mass momentum versus the X-band phase. The momentum difference between the minimum and maximum in the curves is 0.25 MeV and 0.25 MeV for the 0 degrees TDC phase and 180 degrees phase case, respectively. If in the SITF the X-band reduces the momentum with roughly 50 MeV, the change in 3 degrees RF phase is 0.07 MeV. Thus the RF phase of the X-band cannot account for all momentum loss and it is likely that synchrotron radiation has a pronounced influence on the electron bunch.

5.4 Conclusions

In conclusion, the setup has been characterised with reference to the components used to guide the light from the OTR radiator into the optical fibre. The spectrometer has been characterised and the resolution as well as absolute intensity has been established.

Two types of spectra were recognised, namely the incoherent and coherent spectra. The spectra were analysed on the charge dependence. The incoherent spectra were linearly dependent on the charge and showed a flat spectrum as expected by OTR theory. The coherent spectra showed a quadratic dependence. Longitudinal space charge has been proven to have an effect on the bunch length and is a strong candidate for causing the microbunching effect. However, coherent synchrotron radiation has been recognised as a possible source to create additional fluctuations on the current profile as well as an emittance increase. It has not been established which of the two, or if both, caused the microbunching as seen in the spectra. It has been proven however, that both synchrotron radiation and space charge effects are

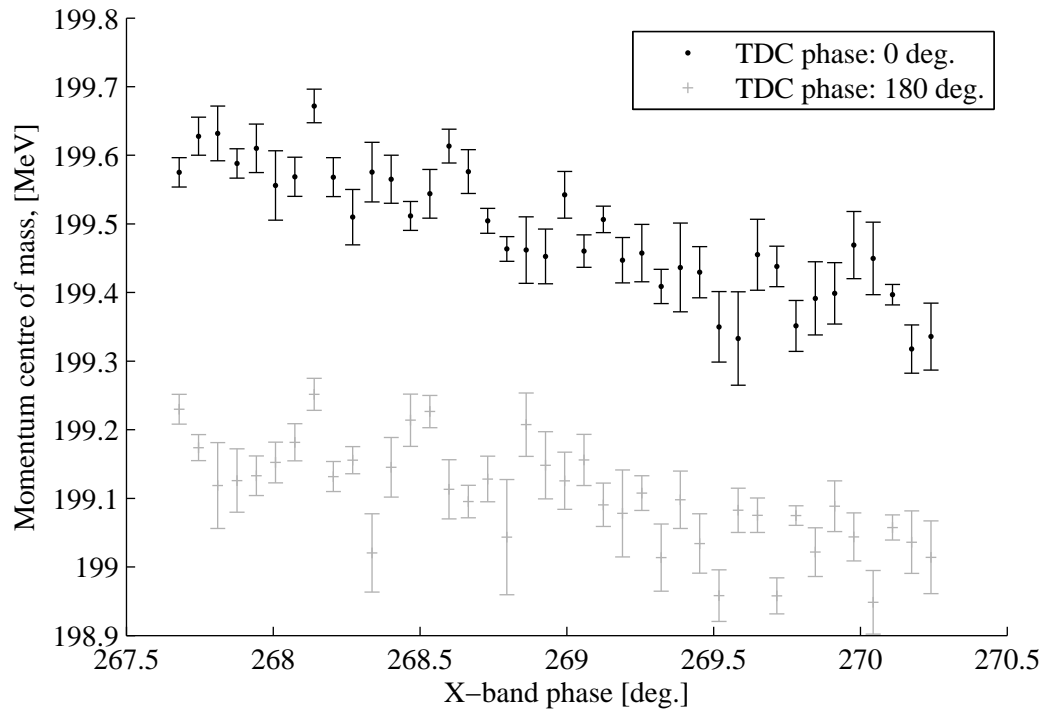


Figure 5.16 – Centre of mass of the electron beam versus the X-band phase. The energy loss suggests that CSR is present.

present.

6 Bunch Length Measurement using Spectral Fluctuations

Bunch length may be measured using optical transition radiation. Baseline diagnostics for SwissFEL uses radiation in the THz domain, detected by Schottky diodes. In this chapter, it is demonstrated that the visible spectrum of OTR contains information on bunch length, as predicted theoretically (see chapter 2).

Section 5.3.2 showed that the gain observed in the spectra is due to a coherence effect. The coherence effect gives rise to spectral fluctuations. The gain is highest in the infrared and reduces as the observed frequency increases. Figure 6.1 shows the spectral intensity of two highly compressed electron bunches. The difference between the data curves is the X-band RF phase and is thus correlated to the bunch length. Both curves feature a sub - 100 fs bunch length with spectral fluctuations, which change with the X-band RF phase. On all data-curves, the fluctuations increase as the bunch length is reduced for all measured spectra. The fluctuations are variant under repetition, which means that the fluctuations' minima and maxima appear at a different frequencies for each electron bunch. This chapter focuses on the methods required for the measurement of bunch length using fluctuations observed in the spectra. The origin of the fluctuations is discussed in Appendix C.

In order to relate the fluctuations to the bunch length, the fluctuations observed in the spectra must be quantified. In particular, the width of the fluctuations' oscillations must be measured. The correlation theory presented in chapter 2 is used to quantify the bunch length dependence. The theory is applied via one of two methods, namely multiple spectral correlation (multiple shot) or single spectrum correlation (single shot). In the following two sections of this chapter, the spectra are analysed according to both methods.

The data in this chapter was recorded on two separate dates and are referred to throughout as **Dataset I** and **Dataset II**. Both data sets were acquired according to the same procedures outlined in chapter 3 but with different X-band RF structure phases and therefore different bunch lengths. Thus, it should be noted that the X-band RF phases of the data sets may not be compared to each other.

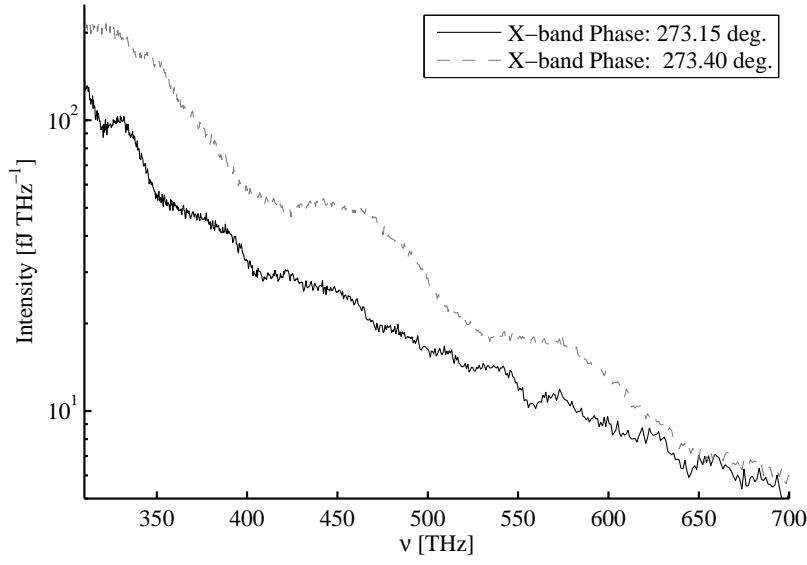


Figure 6.1 – **Dataset I**. Single shot spectral response of OTR, of two bunch lengths. The bunch length was varied using the X-band phase.

6.1 Multiple shot bunch length measurement

In Figure 6.2 the intensity at the central frequency $\nu_c = 310$ THz is plotted versus the intensity at $\nu_c + \Delta\nu = 320$ THz for 500 consecutive shots. The linear correlation between I_{ν_c} and $I_{\nu_c + \Delta\nu}$ of all spectra is calculated from the data according to Equation 2.42.

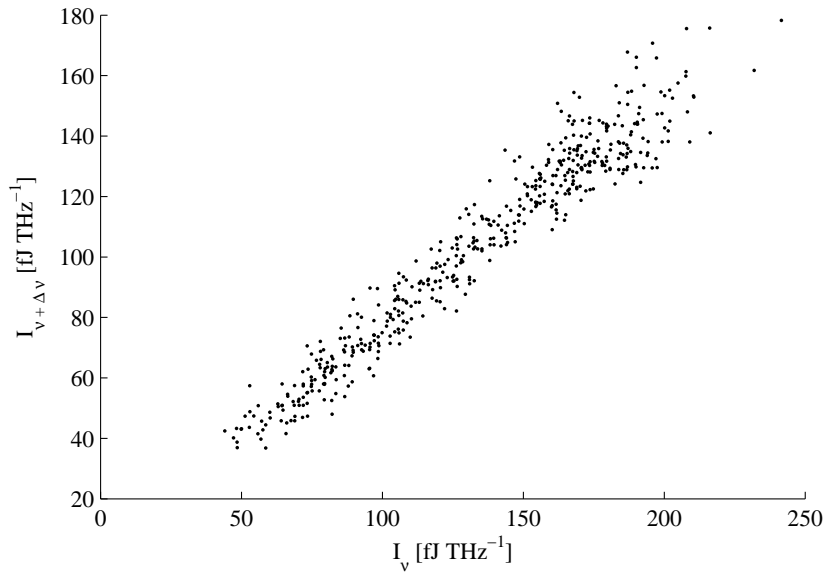


Figure 6.2 – **Dataset I**. Distribution plot of the intensity at $\nu = 310$ THz, $\Delta\nu = 10$ THz of 500 subsequent spectra.

The correlation is calculated for each $\nu_c + \Delta\nu$ where ν_c is fixed. Figure 6.3 shows the correlation versus the frequency shift $\Delta\nu$ for three bunch lengths. At first, the central frequency is correlated to itself, i.e. the correlation is 1. As $\Delta\nu$ increases, the correlation tails off but never falls below an offset. The offset is due to the fact that the coherent domain is fluctuating as a whole, i.e. all frequencies increase and decrease at the same time.

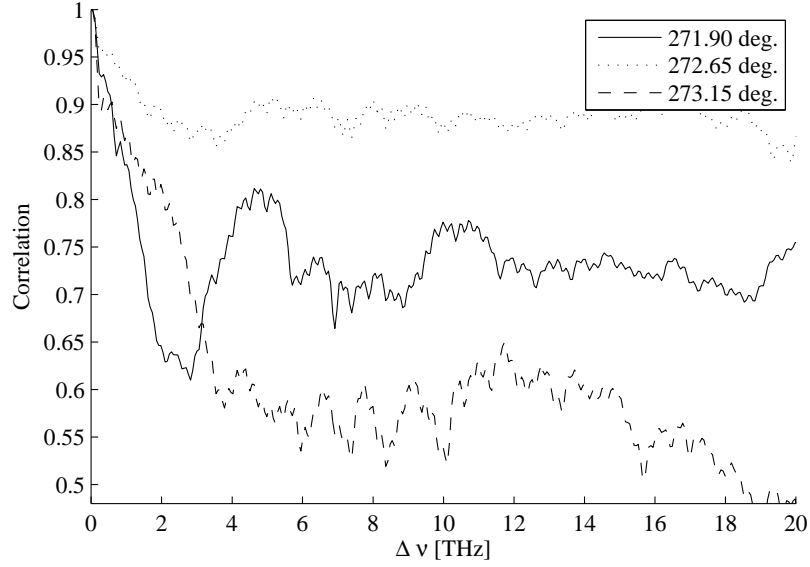


Figure 6.3 – **Dataset I.** Multiple shot correlation plot of three set X-band phases, the central frequency was 310 THz, 500 spectra were used to obtain this plot.

Bunch length information is stored in the width of the correlation peak immediately following $C=1$ (correlation equal to 1). In order to obtain the FWHM or the rms size of the peak in the correlation plot, the first valley encountered is recorded. A valley is defined as a minimum which does not decrease further for at least 2.17 THz. A value of 2.17 THz was chosen such that small fluctuations on the correlation plot did not trigger a minimum. The noise on the correlation plot reduces significantly if more spectra are used for analysis. All spectra presented in this section have therefore been divided by the integration over the whole spectrum to reduce most of the correlation offset.

The X-band phase is varied to change bunch length as discussed in chapter 3.1.1. An X-band scan obtained from the analysis of 1000 spectra is presented in Figure 6.4 (star markers) along with the bunch length measurements with the TDC (grey dot markers). The correlation width is plotted versus X-band phase and shows an increase in correlation width as the X-band phase is increased. In comparing the correlation width data with the TDC data, the correlation width increases as the bunch length decreases. The use of 1000 spectra was required to increase statistics, reducing the noise on the correlation plot and allowing for a more accurate measure of the first minimum. As can be seen in the figure the multiple shot bunch length correlates well to the measured fluctuations.

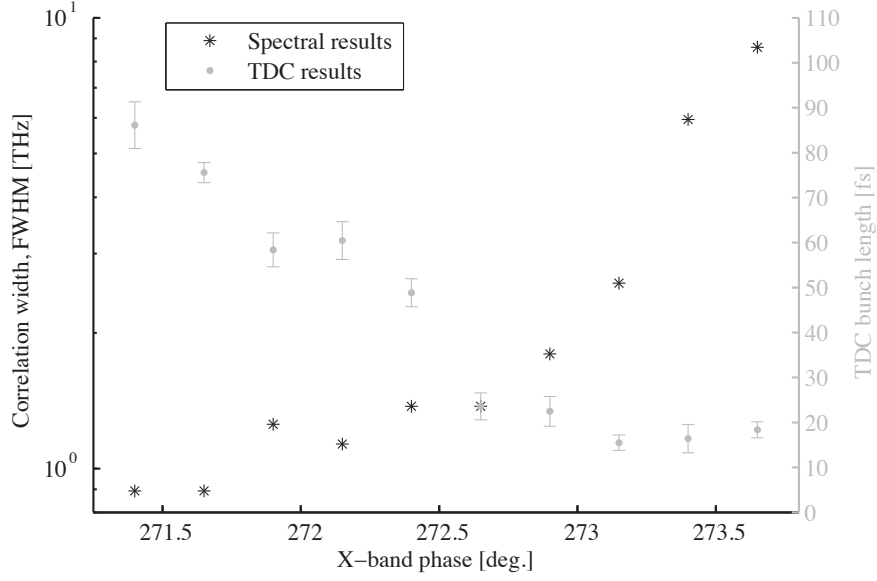


Figure 6.4 – **Dataset I**. Correlation width versus set X-band phase, the error bars are the rms spread of the measurements. The X-band phase is related to bunch length. The star marker represents the correlation width measurement and the dots the bunch length measurements.

6.2 Single shot bunch length measurement

In the previous section multiple spectra were used to calculate a single correlation of I_ν versus $I_\nu + I_{\Delta\nu}$, in which I_ν and $I_{\Delta\nu}$ were fixed and multiple spectra were used to build up statistics. However, the spectral data may be used more efficiently by calculating the correlation width with a single spectrum and thus more time efficiently.

A single correlation may be calculated using one spectrum by fixing $\Delta\nu$ and varying ν . This method is valid since the width of the fluctuations is not expected to change with frequency. The whole spectral range is used for a single bunch length measurement. A single shot correlation plot is presented in Figure 6.5. The data in the figure shows a greater linear correlation between I_ν and $I_{\nu+\Delta\nu}$ with respect to the correlation plot seen in Figure 6.2. This is due to the contribution of the coherence effect at lower frequencies i.e. large intensity differences exist between the infra-red and the ultra-violet ranges.

6.2.1 Single sided compression

The extended linear correlation observed in the single shot correlation plot (Figure 6.6) is uncorrelated to bunch length. This is evident in the offset of the data from three different single shot correlation measurements in Figure 6.6. The plots indicate the shift $\Delta\nu$ versus the correlation for each measurement. The single shot measurement method requires less data and is additionally less noisy than the multiple shot measurement. The correlation plot indicates that the data has several minima at larger shifts $\Delta\nu$. The multiple minima are due to

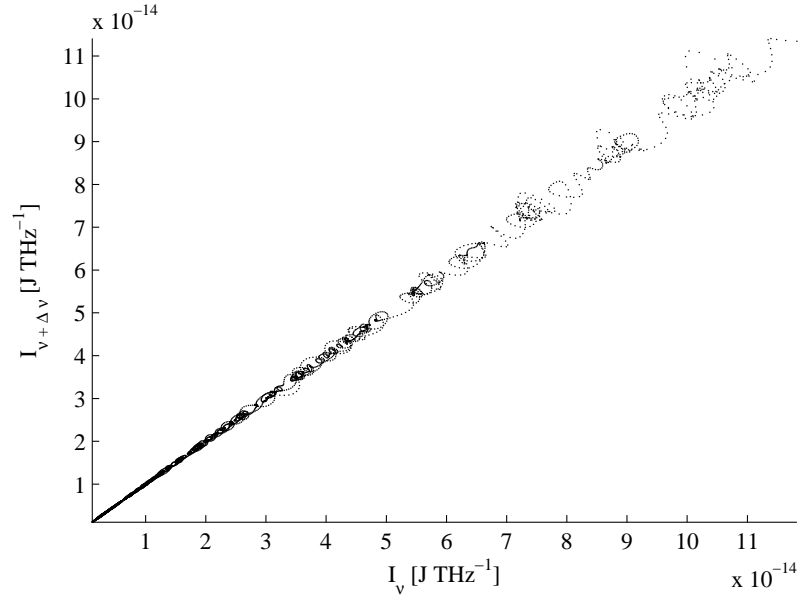


Figure 6.5 – **Dataset I**. Single shot distribution plot. X-band phase is 282.75 deg. Δv was fixed at 0.3 THz and v was varied.

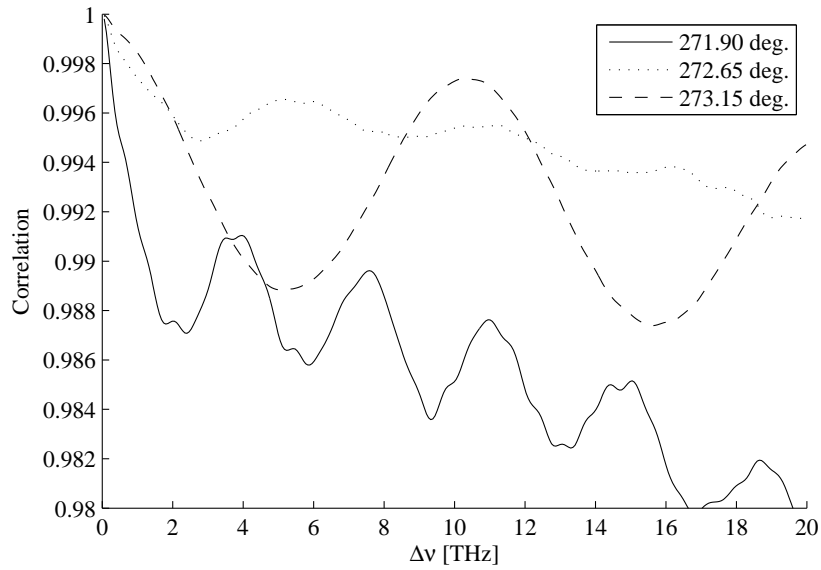


Figure 6.6 – **Dataset I**. Single shot correlation plot of three set X-band phases.

the repetition of fluctuations seen in recorded spectra. Figure 6.7 presents an example of a spectrum with such fluctuations. As in the previous section, a minimum is defined for a point where there is no further decrease of the correlation for at least 2.17 THz. Using the minimum and the corresponding correlation value the FWHM was extracted from the data.

The data in Figure 6.8 shows the correlation width versus the X-band phase (black circle

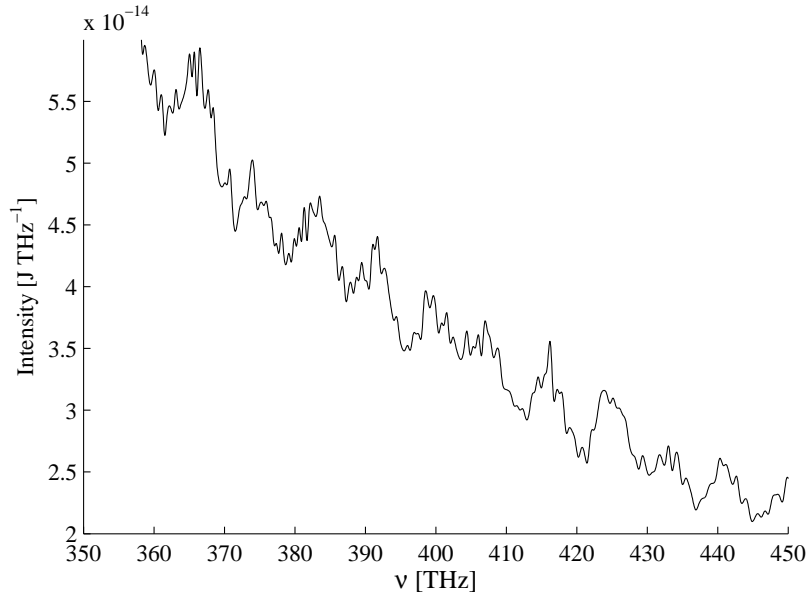


Figure 6.7 – **Dataset I**. Single shot OTR spectrum from a compressed bunch, detailed view. The third harmonic cavity phase was 282.75 deg. Fluctuations can be seen in the spectrum.

markers) and the TDC bunch length (grey dots). Fifty spectra were used to calculate the mean and rms error bars. The data shows that the correlation width error increases considerably towards smaller bunch lengths but depends greatly on the TDC bunch length.

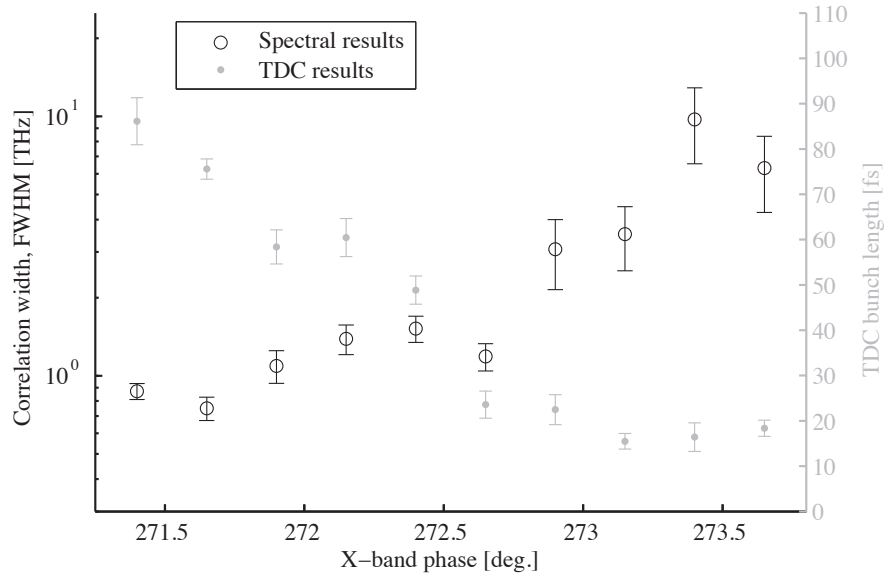


Figure 6.8 – **Dataset I**. The correlation width versus set X-band phase and the TDC bunch length versus set X-band phase. The circles represent the correlation width measurements, the dots represent the TDC bunch length measurement. The stability of the X-band phase was 0.18 degrees rms.

6.2.2 Compression and over-compression

In order to increase the resolution of the measurements in the X-band domain in single shot mode, a detailed X-band scan was performed. In this second dataset (Dataset II), the bunch was shortened via compression and over-compressed. An over-compressed beam means that such a chirp is applied to the beam that the head and tail in the bunch compressor swap places, i.e. the head becomes the tail and vice versa. In comparison to Dataset I, which had 10 X-band phases, the X-band phase range for Dataset II was divided across 100 X-band phases. Per X-band phase, 35 spectra were recorded instead of 1000. At every X-band phase the mean correlation width and the rms error was calculated. The measured X-band phase stability was 0.18 degrees rms. The data in Figure 6.9 shows the single shot fluctuation method's correlation width (black stars) and the bunch length measured with the TDC (grey dots). The same TDC data was presented in chapter 4. The bunch length as measured ranged from 140 fs down to 22 fs.

If the bunch length is long no spectral fluctuations are present. As the bunch length is reduced below 70 fs, spectral fluctuations start to appear. These spectral fluctuations' width depend on bunch length. At the minimum bunch length, both the TDC and spectral curve show a plateau ranging a similar X-band phase.

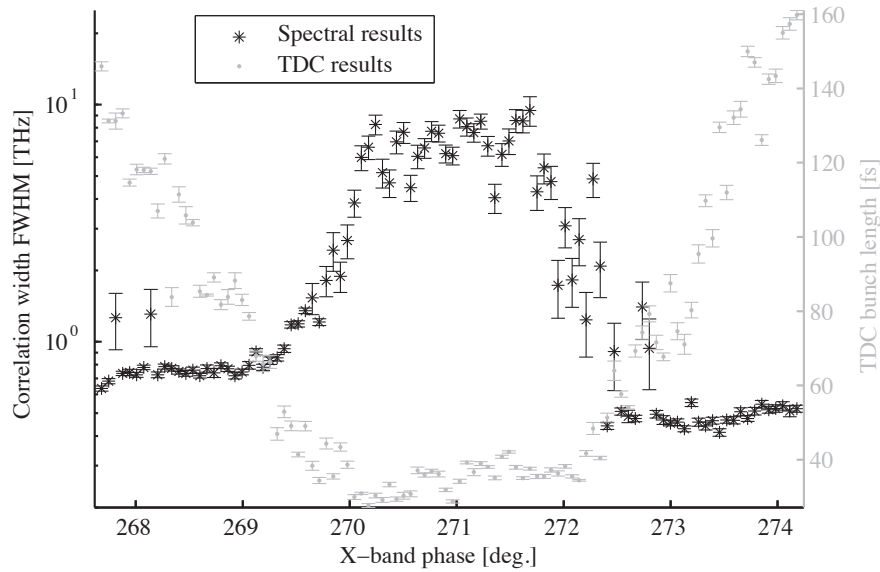


Figure 6.9 – **Dataset II**. Correlation width versus set X-band phase (grey dots) and TDC bunch length versus the X-band phase (black stars). The spectral measurement is sensitive below 70 fs rms.

6.3 Conclusions

The coherent domain contains information that strongly depends on the bunch length in the form of fluctuations onto the coherent domain. The width of these fluctuations is dependent

Chapter 6. Bunch Length Measurement using Spectral Fluctuations

on bunch length. It was shown that two methods could be used to extract the fluctuations' width, namely the multiple shot correlation method and the single shot correlation method. The correlation width obtained from the fluctuations correspond very well to the bunch length as obtained from the TDC measurements.

7 Outlook, SwissFEL Implementation

Both the TDC measurements and the spectral measurements presented in this thesis may be used in the SwissFEL to measure the bunch length. The schematic in Figure 7.1 shows the SwissFEL layout with both the proposed TDC and spectral measurement locations.

The bunch length after the second bunch compressor (BC2) depends on the user operation. Three modes are summarised in Table 7.1.

Table 7.1 – Key design parameters of the SwissFEL accelerator according to simulations by B. Beutner. The difference in rms values from chapter 1 originate from the calculation method, all currents below 100 A were set to zero.

Parameter	Long pulse	Short Pulse	Ultra-short Pulse
Bunch charge (pC)	200	10	10
Initial bunch length at the gun (fs rms)	2600	1574	1574
Bunch length, after BC2 (fs rms)	19.3	1.6	1.0
Bunch length, before undulator (fs rms)	19.3	1.6	0.6

7.1 TDC implementation

In the introduction to this thesis it was stated that the measurement of bunch length becomes more difficult as the bunch length becomes shorter. In SwissFEL the TDC power requirements

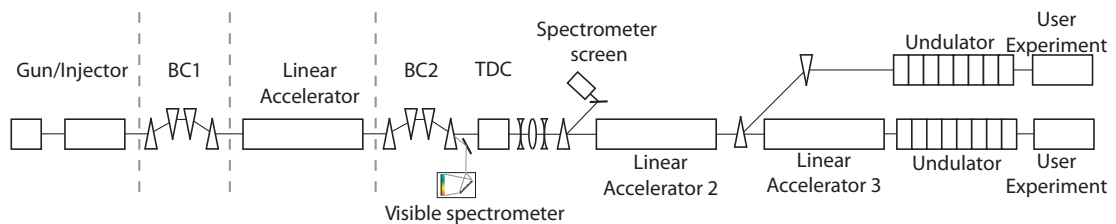


Figure 7.1 – Overview of the SwissFEL with the proposed methods included.

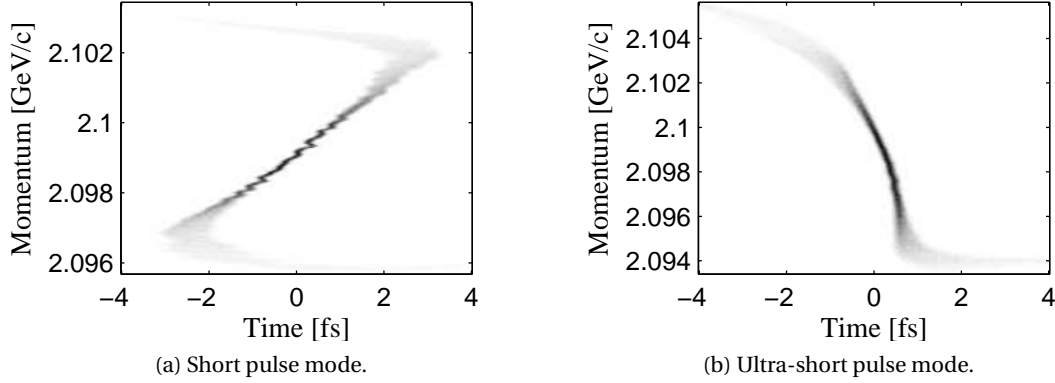


Figure 7.2 – The longitudinal phase space after BC2. Courtesy of B. Beutner.

become large because of the increased momentum of the particles (see Equation 3.11). Higher order harmonic cavities have been produced and successfully demonstrated but are challenging to fabricate because of surface requirements [16]. The novel analysis method presented in this thesis, compared to the conventional TDC method, shows that less power is needed in the TDC structure to measure the same bunch length.

In order for the analysis method to work in SwissFEL, the electron bunch must feature an energy chirp. Such conditions are reached immediately after the second bunch compressor (BC2). The data in Figure 7.2 (a) and (b) shows the longitudinal phase space after the second bunch compressor from the short pulse mode and the ultra-short pulse mode, respectively. The data shows a clear correlation between the time and momentum due to the momentum chirp onto the electron bunch. More importantly, the analysis method presented requires that the electron bunch does not cross a momentum slice twice, i.e. two parts of the electron bunch do not have the same momentum, which is confirmed in Figure 7.2.

Experimentally, the method requires a TDC, magnetic optics to provide the focus onto the screen, a phase advance, and a dipole to establish a spectrometer arm. Although the TDC requirements are reduced for the proposed method, the centre of mass of the electron bunch in a momentum slice must change relative to other slices. The intrinsic beam size in the dispersive direction must be chosen as small as possible to obtain the smallest resolution. The optics between the TDC and the imaging screen require a phase advance to optimise the R_{12} component of the transfer matrix and provides a focus onto the spectrometer screen.

The method presented can measure bunch length at the SwissFEL. The longitudinal phase space present at the BC2 is suitable for the method. Moreover, cost as well as TDC requirements can be reduced with the proposed method.

7.2 Spectral implementation

The spectral method implementation as presented in this thesis is non-trivial. Simulations of the longitudinal profile show that the spectral response of any radiation after the second bunch compressor is likely to be dominated by coherent radiation in the visible domain. The data in the Figures 7.3 (a) - (f) show the current profiles and the frequency responses of the long pulse mode, short pulse mode and the ultra-short pulse mode after BC2 at the SwissFEL. The spectra show that the incoherent domain cannot be used since the coherent domain stretches into the visible domain, overpowering the incoherent spectrum. However, the spectral responses still show features that may be used to measure bunch length.

Firstly, the electron bunches are of similar length or shorter in SwissFEL than in the SITE. Secondly, the momentum of the particles are much larger. The space charge forces scale with the inverse square of the momentum, thus very short spikes are possible on the electron bunch. The result is that the frequency response of the current profile stretches into the visible domain as presented in the aforementioned figures. The bunch lengths of the long pulse, the short pulse mode and the ultra-short pulse mode are 19.3 fs, 1.6 fs and 1.0 fs as presented in Table 7.1. In the ultra-short pulse mode, the bunch is compressed further before the undulators in an additional compressor stage (not shown in Figure 7.1). Because of the different charges used in the simulations, the spectral intensity values between the 200 pC and the other simulated spectral responses (both 10 pC) may not be compared.

On the current profile of the long pulse mode two features can be observed: Firstly, the general current profile shows a step function both at the head of the bunch and at the tail of the bunch. Secondly, a modulation is observed onto the current profile. Both features can be seen back in the spectral response: The general current profile's effect lies in the fast modulation in the spectral response (25 THz peak to peak) whereas the broad spectral modulation (roughly 300 THz range) represents the fast modulation on the current profile. To monitor the bunch length, the 25 THz peak to peak modulation must be monitored and may give feedback on the bunch length.

In the short pulse mode, the general current profile is a step function. Superimposed on the step function modulations are located. It can be seen in the spectral response that the bunch length information is stored, similar to the long pulse mode, in the modulation of the spectral response. In the ultra-short pulse mode, the coherence effect is clearly dominated by the bunch length. The bunch length can be directly observed from the coherence over the spectral domain.

To retrieve the bunch shape information the phase of the spectral radiation is needed. The Kramers-Kronig relation may be used to retrieve the spectral phase. However, the Kramers-Kronig phase retrieval is non-trivial, examples may be found in [25, 26].

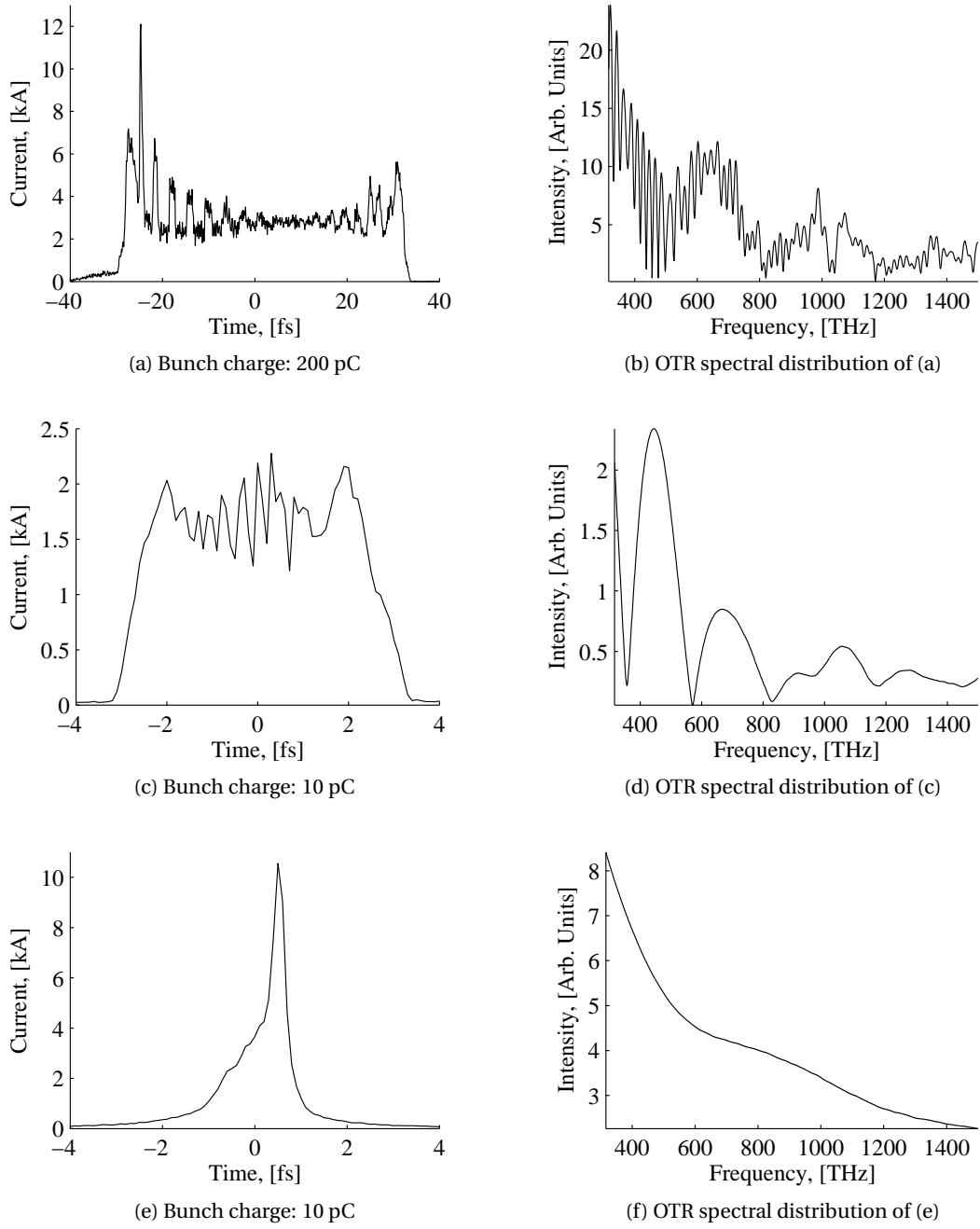


Figure 7.3 – Current distribution (a, c, e) and frequency response (b, d, f) of the long pulse mode (a,b), the short pulse mode (c, d) and the ultra-short pulse mode (e, f). Data for the current profiles obtained from B. Beutner.

8 Conclusions

The aim of this thesis was to develop and test a method to measure the electron bunch length from femtosecond electron bunches using visible light from optical transition radiation. The study included a reference bunch length method to verify the spectral measurement proposed, which was chosen to be the Transverse Deflecting Cavity (TDC). A first step was made towards measuring fs electron bunches with both a spectral method and the TDC. The findings are summarised in this chapter.

With the use of an optical spectrometer it is possible to resolve the spectra coming from optical transition radiation. Transition radiation holds bunch length information in the form of fluctuations in the emitted radiation. The information may be extracted in two ways. Firstly, it was shown that the fluctuations in the Fourier transform of the measured transition radiation spectrum contain bunch length information. Secondly, a correlation theory may be applied to the optical transition radiation spectrum to extract bunch length information.

The bunch length at the SITF was reduced to the minimal bunch length possible. Because the SITF was not built for the optimised production of femto-second bunch lengths, undesired effects were observed due to longitudinal and transverse space charge effects. The longitudinal space charge effects had the most prominent effect on the longitudinal electron bunch profile and was understood through simulations.

The TDC was used as a reference bunch length method but could not be used in the conventional way because of the large and broken-up transverse beam sizes. A novel method has been proposed to measure bunch length in a space charge dominated beam in which the transverse intrinsic beam size is large. The method has been proven to be successful in simulations as well as experimentally. The experimental data corresponds very well to that acquired from the simulations. Moreover, the minimal bunch length from experiments and simulations are of the same order, 19.5 fs to 24.5 fs respectively. Although the method is promising, a primary condition is that the correlated energy spread must be large and the bunch length must be measured in a magnetic spectrometer. The method is independent of the transverse beam size along the bunch and removes the vertical-relative energy spread (y, δ) correlation at the high

energy spectrometer. Due to the phase advance this corresponds to the (y', δ) correlation at the TDC. The method proposed may increase the current profile resolution and may enhance towards shorter bunch lengths. The minimal bunch length measured with the TDC was 24.5 fs and 27.7 fs using two zero-crossings. If it could be implemented, the power needed in the transverse deflecting cavity may also be reduced, reducing cost as well as the manufacturing requirements.

The spectral setup to collect the OTR radiation into an optical spectrometer has been characterised with particular reference to the components used to guide the light from the OTR radiator into the optical fibre and the spectrometer itself. Two types of spectra were recognised, namely incoherent and coherent spectra. These were analysed with reference to their charge dependence. The incoherent spectra were linearly dependent on the charge and showed a flat spectrum as expected from OTR theory. The coherent spectra showed a quadratic dependence on charge. Longitudinal space charge has been proven to have an effect on the bunch length in both simulations and experiments. Experiments suggests that synchrotron radiation is also affecting the beam and has a notable effect on the electron bunches.

The OTR spectra contain information that strongly depends on the bunch length in the form of fluctuations. Despite the dependence on bunch length, the origin of the fluctuations are unknown. The correlation theory was used to extract the bunch length dependence. Because this method may be used to measure bunch length in the future SwissFEL, the results were compared to the TDC bunch length. In comparison to the TDC data, the method becomes sensitive below a bunch length of 70 fs rms.

A Measurement of Fluctuations at the Swiss Light Source

The Swiss Light Source (SLS) is a 2.4 GeV electron synchrotron located at PSI. To measure the bunch length at such a facility, the measurement of spectral fluctuation was proposed in the visible domain [29]. The method relies on fluctuations as introduced in chapter 2 but differs in that the fluctuations observed are due to the limited bandpass filter.

The method employs a narrow spectral band filter and is based on the variance under repetition from the incoherent radiation spectrum. Statistics have to be built up in order to calculate the variance in the incoherent spectrum domain. Bunch length is related to the variance via the following expression [29, 58]:

$$\delta^2 = \frac{\sigma_I^2}{\langle I \rangle^2} = \frac{1}{\sqrt{(1 + 4\sigma_\omega^2 \sigma_\tau^2) T}} \quad (\text{A.1})$$

In which δ is the relative intensity fluctuation, σ_I the standard deviation of the pulse intensity, $\langle I \rangle$ the mean pulse intensity, σ_ω the filter bandwidth in Hz and σ_τ the longitudinal electron pulse length. T represents the fluctuations due to beam transverse sizes. Assuming an infinitely small beam and beam divergence this term approaches one. Equation A.1 shows that shorter bunches give larger fluctuations, provided that the same spectral band filter is used. This equation is valid as long as no coherent radiation is present.

The experimental setup employs bending magnet synchrotron radiation from the diagnostics beamline at the Swiss Light Source (see Figure A.1). The energy selection uses the angular frequency dependence to select the visible light from the synchrotron radiation. The transfer line, which is under vacuum, consists of several mirrors and lenses to focus the beam onto the streak camera. After the vacuum window a flip mirror directs the light to either the streak camera or the avalanche photodiode (APD) setup. The APD setup consists of a spectral band filter of 3 nm full width half maximum, a set of optical density filters and a lens to focus the light on the APD. The APD in question is the C30902SH. The APD is connected to a 6 GHz digital oscilloscope (LeCroy Wave Master 8620A) which directly records the fluctuations.

Appendix A. Measurement of Fluctuations at the Swiss Light Source

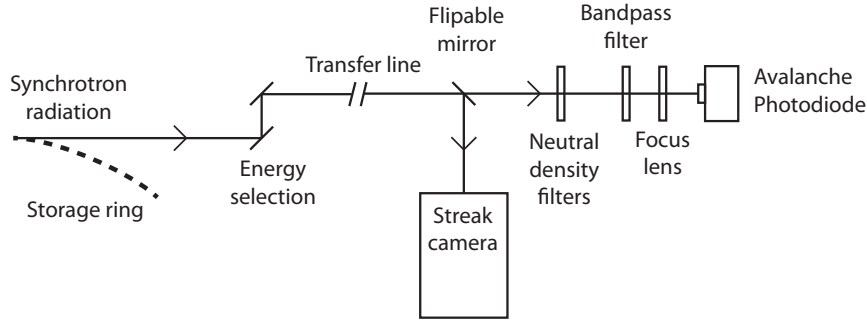


Figure A.1 – Experimental setup of the fluctuation setup at the SLS.

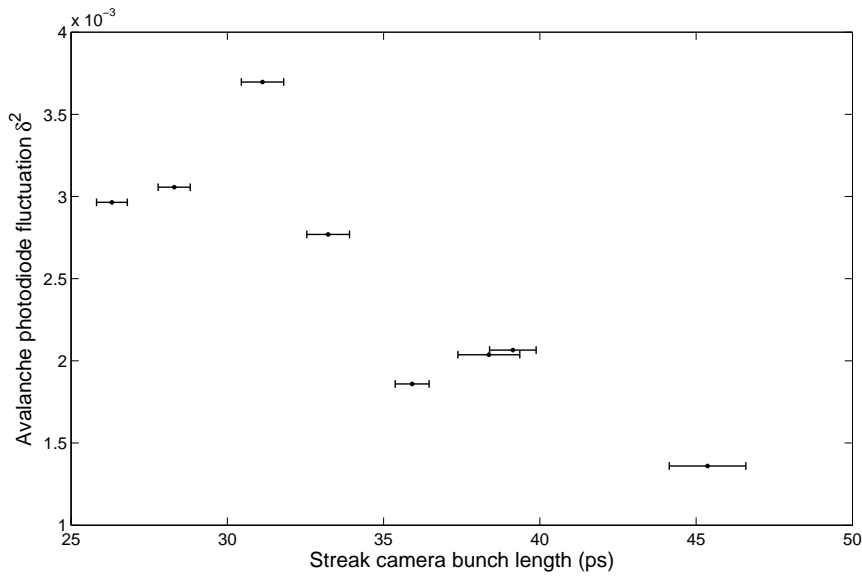


Figure A.2 – Photon statistics measurement, in collaboration with Egger: [27].

Figure A.2 shows the fluctuation of the avalanche photodiode versus bunch length measured by the streak camera. In a streak camera fast varying electric fields deflect electrons that are generated by the synchrotron radiation onto a scintillator. By imaging the streaked electron beam on the scintillator, the bunch length is deduced. The APD fluctuations have been calculated via:

$$\delta^2 = \frac{\sigma_{meas}^2 - \sigma_{noise}^2}{(\mu_{meas} - \mu_{noise})^2} \approx \frac{\sigma_{meas}^2}{\mu_{meas}^2} \quad (A.2)$$

In the limit $\sigma_{meas} \gg \sigma_{noise}$ and $\mu_{meas} \gg \mu_{noise}$ Equation A.2 can be reduced to two terms. Per bunch length 10,000 signals have been recorded, divided across 100 bins, from these we have obtained the standard deviations σ and averages μ of the Gaussian distribution from which the fluctuations are recorded as shown in Figure A.2. Similarly the noise has been recorded

from which the standard deviation and average are calculated. The fluctuations have been plotted against the bunch length measured with the streak camera. In a streak camera electric fields are used to deflect electrons such that the electrons, created by the visible synchrotron radiation on a photocathode, are streaked across a scintillator. The light generated at the scintillator is then imaged onto a CCD camera. From these images, the rms bunch length was extracted. The error bars in the streak camera bunch length indicate the standard deviation of 15 successive bunches.

In Figure A.2 a correlation can be seen between the streak camera bunch length and the detected fluctuations with the APD. The bunch length may be calculated from the fluctuations using Equation A.1 but result in bunch length overestimation. In order to correct for the overestimation, fluctuations from the synchrotron, APD and oscilloscope need to be taken into account. Moreover, accelerator settings must be altered to change the bunch length and hence the stability. As the bunch length becomes shorter, the synchrotron may feature instabilities in the transverse profile. The measurements presented in this appendix may have suffered from electron beam instabilities and thus for future measurements, the transverse beam position and profile must be monitored. Moreover, the transverse profile coupled into the APD must be monitored to ensure the fluctuations are indeed not transverse fluctuations originating from the beamline.

In summary, a bunch length method was tested following the principle described in chapter 2. As the bunch length is decreased, the fluctuations are expected to increase due to the limited bandpass filter. The fluctuation bunch length method at the SLS has detected APD fluctuations that depend on bunch length.

B Bunch Length Measurement of Incoherent Spectra at the SwissFEL Injector Test Facility

In chapter 2 it was shown that the fluctuation in the Fourier transform of the measured spectrum is the autocorrelation of the temporal profile (see Equation 2.37). Experimentally, the OTR spectrum must be recorded a number of times in order to build up statistics. Moreover, the spectrum needs to be incoherent. The minimum bunch length at which the spectrum was fully incoherent was roughly 100 fs rms. Further compression, either with the third and fourth accelerating structures or with the bunch compressor, gives a coherence effect in the spectrum, as described in the previous chapter. In this section incoherent spectra are considered measured with the optical spectrometer as described in chapter 5.

From the maximum compression at which no coherence was present, the scrapers were used to reduce the bunch length further. The process by which bunch length is reduced using scrapers in the bunch compressor is described in chapter 3. As discussed, electrons are lost as the bunch becomes shorter. The signal to noise ratio at 509 THz as a function of charge is shown in Figure B.1. Due to the dark noise of 2.5 rms counts and the limited analog to digital conversion in the spectrometer, the signal to noise ratio as a function of the detection frequency (see Figure B.2) has a similar data profile as the sensitivity curve of the optical spectrometer (see Figure 5.10). The signal to noise ratio was calculated over the whole spectral domain, with a charge of 130 pC.

In order to retrieve the bunch length, incoherent spectra (see e.g. chapter 5, Figure 5.12) are interpolated with 20,000 points in order to linearise the frequency bins. The Fourier transform is calculated, transforming the spectra from the frequency domain to the τ domain. 500 spectra were used to calculate the fluctuations σ_Γ according to Equations 2.30 and 2.37.

The experimental results of the fluctuations in the τ domain are shown in Figure B.3 for two bunch lengths. The τ domain spanned from 0 fs to 8300 fs. Bunch length information is expected to be stored in the 0 fs to 200 fs domain, however the data in the figure shows no bunch length information, which would have been apparent via an increase or decrease of signal. Further measurements at different charges and thus different bunch lengths were performed, but did not present any bunch length information. An important aspect of the non-

Appendix B. Bunch Length Measurement of Incoherent Spectra at the SwissFEL Injector Test Facility

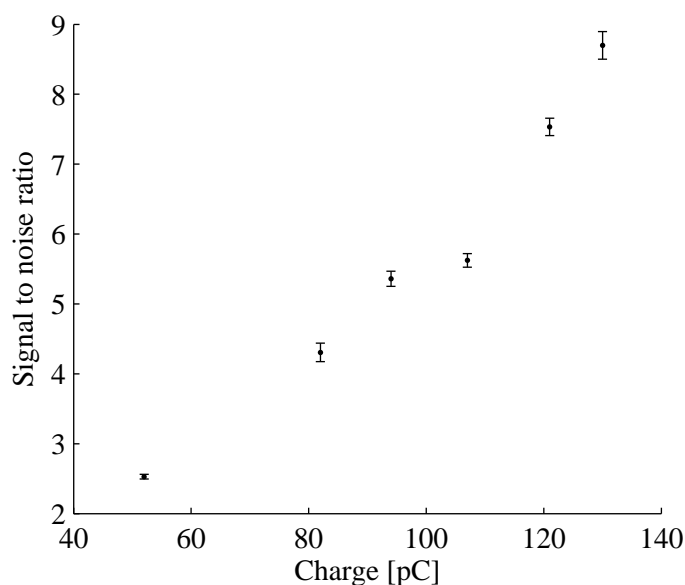


Figure B.1 – The QE65000 signal to noise ratio of a varying charge in the accelerator

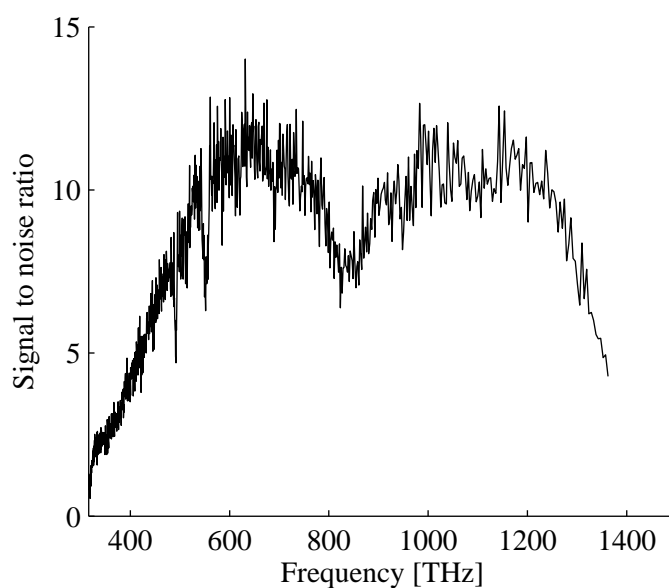


Figure B.2 – The QE65000 signal to noise ratio versus the frequency with an electron bunch charge of 130 pC.

visibility of fluctuations is the low signal to noise ratio of the signal. The varying resolution across the spectrometer, due to linear distribution of the spectral bins in the wavelength domain, also contributes to the lack of visibility of these fluctuations. The resolution at 316 THz is 0.3 THz rms, increasing to 5.1 THz rms at 1400 THz (see Figure 5.11).

In order to increase the signal to noise ratio, there must be an increase in the signal, or of the

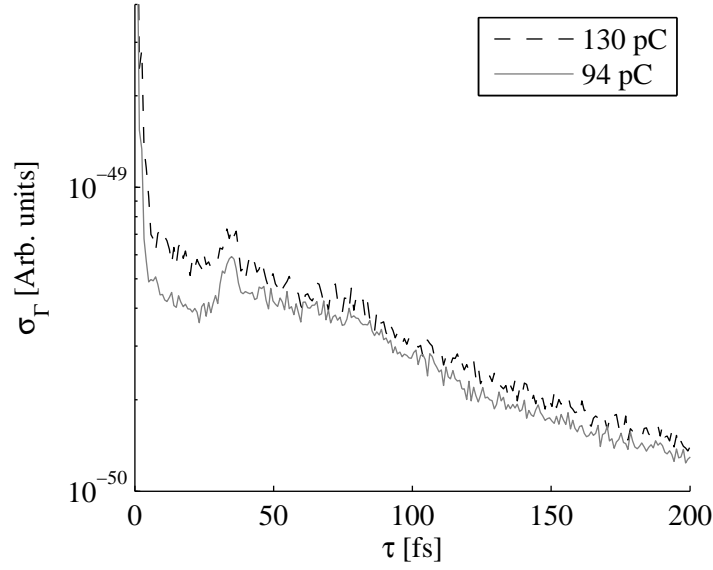


Figure B.3 – The experimental autocorrelation (τ domain) or the temporal profile, the bunch length was varied using the scrapers in the bunch compressor.

sensitivity of the detector. The OTR signal may be enhanced by increasing the charge and the momentum of the particle beam. Firstly, the signal scales linearly with the charge of the electron bunch in the accelerator. Secondly, by increasing the momentum, the space charge effects as presented in chapter 4 will decrease, allowing us to go to shorter electron bunches. The OTR signal scales with the Lorentz factor via the natural logarithm of γ . Increasing the momentum from 200 MeV to 5800 MeV, which is the momentum of the electron beam at SwissFEL, the gain in OTR intensity is a factor of 1.5.

Other radiation processes than optical transition radiation are available such as edge radiation or synchrotron radiation. Edge radiation is generated due to the fields leaking out of the dipole. These fields focus the beam perpendicular to the beam direction of travel and deflection orientation. Since the focusing effect accelerates the beam, the electron bunch radiates, thereby allowing for the extensive characterisation of particle beams [49, 59, 60]. The signal (or power of the synchrotron radiation) increases with the square of the particle energy, enabling a larger increase in intensity in respect with OTR radiation. The signal increases by a factor of 841 with an increase of energy from that of the SITF to that of the SwissFEL, assuming that the same magnet strength is used.

Currently, the optical spectrometer used for this experiment is one of the most sensitive spectrometers available commercially. Hence it is easier to gain a factor of two in signal than to reduce the signal to noise ratio by a factor of two. Avalanche Photo-Diodes (APDs) are available to detect single photons in order to increase the signal. In the current setup, replacing the optical spectrometer with an APD may give a higher signal, however the visibility is then limited to a single frequency. The optical spectrometer gives invaluable information over

Appendix B. Bunch Length Measurement of Incoherent Spectra at the SwissFEL Injector Test Facility

the whole frequency range, establishing the characteristics of both incoherent and coherent spectra. The use of an APD detector retains great potential for future measurements due to the availability of single photon counting and the possibility of higher signal to noise ratio.

In conclusion, the fluctuation method of measuring the bunch length by means of the fully incoherent spectrum was unsuccessful. The low signal to noise ratio was considered a limiting factor as well as the low signal intensity of optical transition radiation.

C Hypothesis: Origin of the Spectral Fluctuations

In chapter 5 it was discussed that the coherent radiation stretches into the visible domain and originates from a substructure onto the electron bunch. The outlook in chapter 7 underlines this with the aid of simulations. This appendix explores a possible explanations for the fluctuations as observed in chapter 6, namely the fluctuations due to bunch length.

The fluctuations observed in chapter 6 may originate from the bunch length information. The following section explains the principle behind the hypothesis.

The simulated current profile and corresponding spectral OTR response are shown in Figure C.1. The shown current profile and spectral response are from the shortest simulated current profile in the SITF. Although the current profile shows a sharp rise in current at the head and tail, the spectral response does not feature a strong coherence in the visible domain. The spectral response shows a slight increase in intensities at the lowest frequencies.

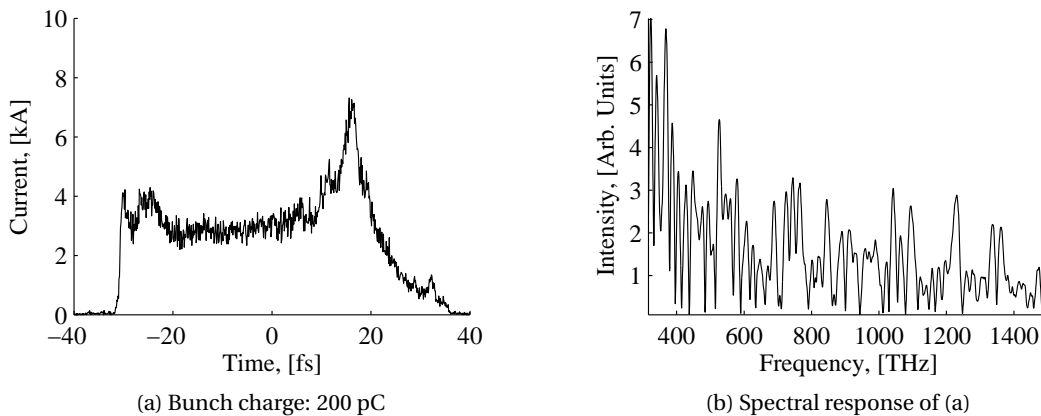


Figure C.1 – (a) Current profile and (b) spectral response of a simulated electron bunch at the position of the optical spectrometer at the SITF

In SwissFEL the simulated spectral response of the long pulse mode is dominated by the intra-bunch current fluctuations (see chapter 7). Since the bunch length in the SITF is similar

Appendix C. Hypothesis: Origin of the Spectral Fluctuations

to the long pulse mode in SwissFEL, the fluctuations as observed on our spectra are likely due to a substructure within the bunch rather than from the general current profile.

It was also observed that the coherent domain stretches roughly to 700 THz and does not extend to higher frequencies if the bunch length becomes shorter. This is another indication that the coherent radiation we observe are due to current fluctuations within the bunch. As the bunch is compressed more particles take part in the coherent process, resulting in a higher spectral intensity towards the infra-red domain, this indicates that the microbunching is more pronounced. Thus, the fluctuations in the spectra may originate from the micro-bunching in the current profile.

D Observation of Interference Patterns from Optical Transition Radiation at the SITF

At the strongest bunch compressions (roughly 20 fs rms) interference patterns were observed. This appendix reports briefly on these observations.

A 10 nm FWHM bandpass filter at 633 nm was inserted between the off-axis parabolic mirror and the camera (see Figure 5.2 for the setup without filters). The OTR pattern was observed at the position of the entrance of the optical fibre. In order to compare the image with bandpass filter with an image over the whole spectral domain, an optical density filter was inserted before the camera against over-exposure. The optical density filter had a transmitted light at 633 nm of 1 percent. The optical density filter and bandpass filter were positioned a couple of millimetres in front of the camera. The filters were positioned on an angle in order to rule out interference due to scattering inside the filters.

Figure D.1 shows the subsequent images of the spatial OTR distribution as coupled into the optical fibre with an optical density filter mounted before the camera. The images shown in Figure D.2 were acquired consecutively at the same position but the optical density filter was replaced by the aforementioned bandpass filter. In comparing the images with and without the bandpass filter, those acquired with the bandpass filter show an interference pattern.

The interference patterns shown in the graphs are a result of interference of coherent light. A possible explanation of the interference pattern is given by Wartski *et al.* [17]. Wartski generated OTR on an aluminium coated mylar foil with a 35 MeV to 72 MeV electron beam. By collecting the OTR radiation onto a camera with the aid of lenses, the double foil configuration showed interference patterns. The interference patterns observed in his experiment may explain the interference patterns in our experiment by the aluminium coated waver we used in our experiments.

Appendix D. Observation of Interference Patterns from Optical Transition Radiation at the SITF

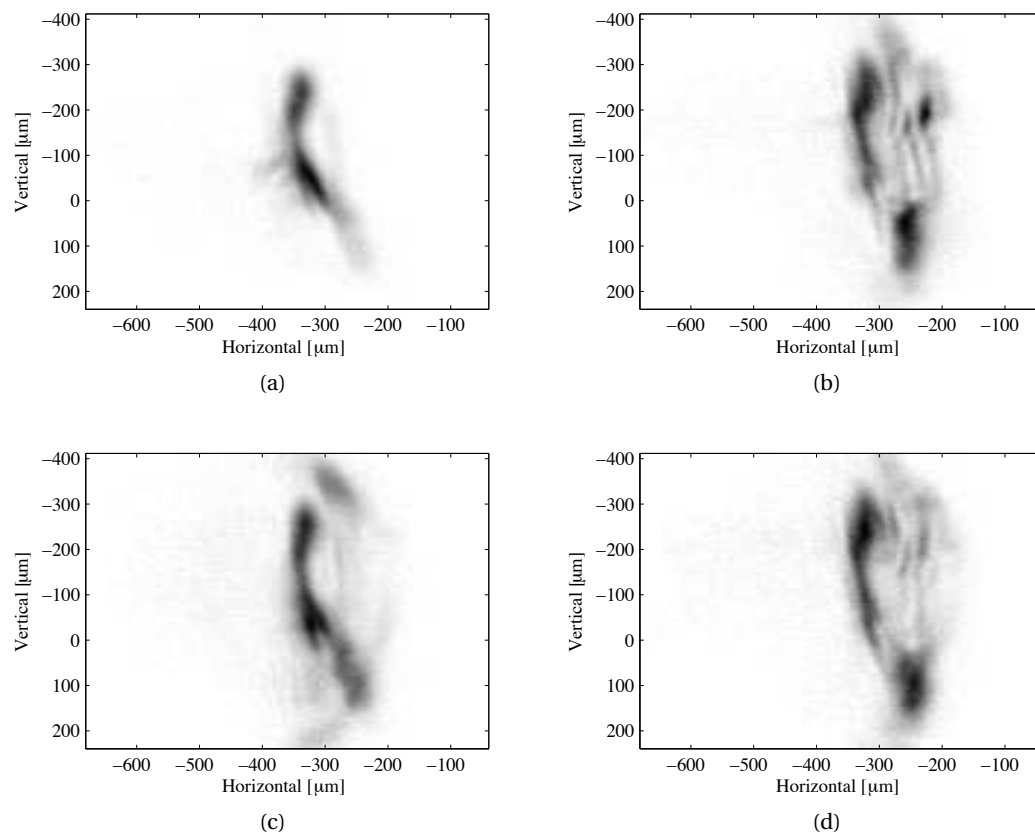


Figure D.1 – The OTR radiation as coupled into the optical fibre with camera C4 (See Figure 5.1). The images were taken subsequently, an optical density filter with an transmission of 0.01 was mounted in front of the camera to reduce the intensity.

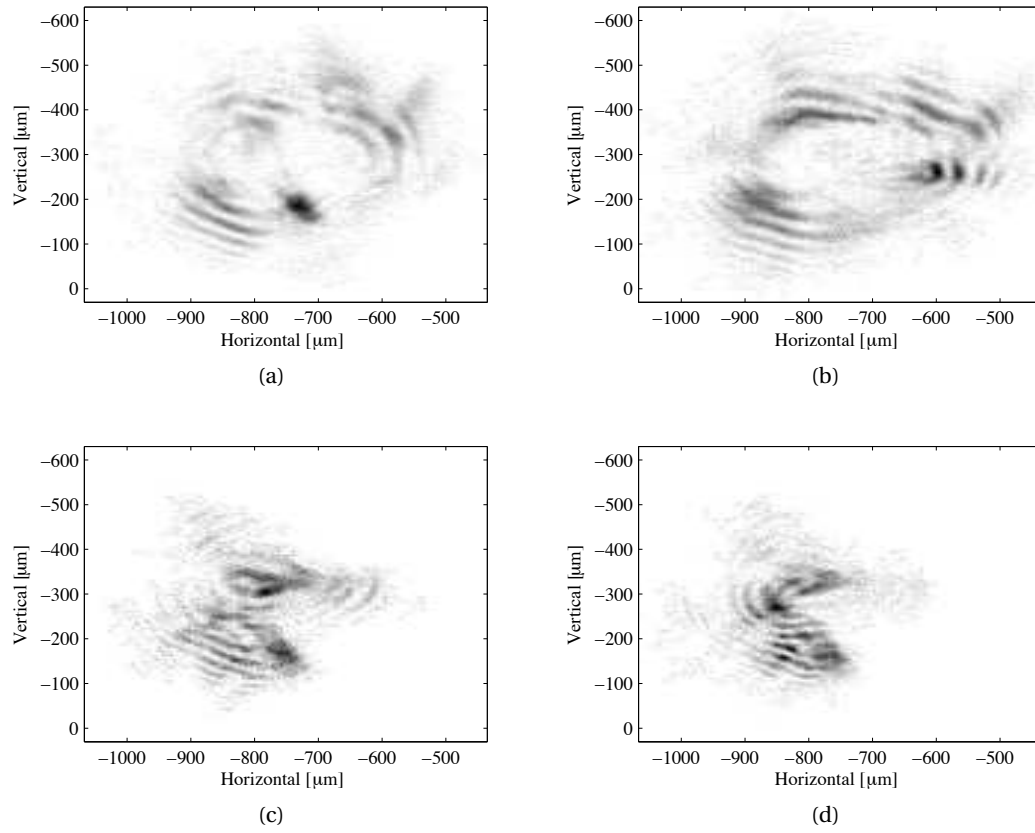


Figure D.2 – The OTR radiation as coupled into the optical fibre with camera C4 (See Figure 5.1). The images were taken subsequently, an optical bandpass filter of 10 nm FWHM at 633 nm mounted in front of the camera.

E Spike Removal from Spectra

Random spikes are superimposed onto the spectral data. It was found that the spikes as observed in Figure E.1, obstruct data analysis. The spikes were therefore removed. The spikes only occur when the beam is on, and do not carry bunch length information.

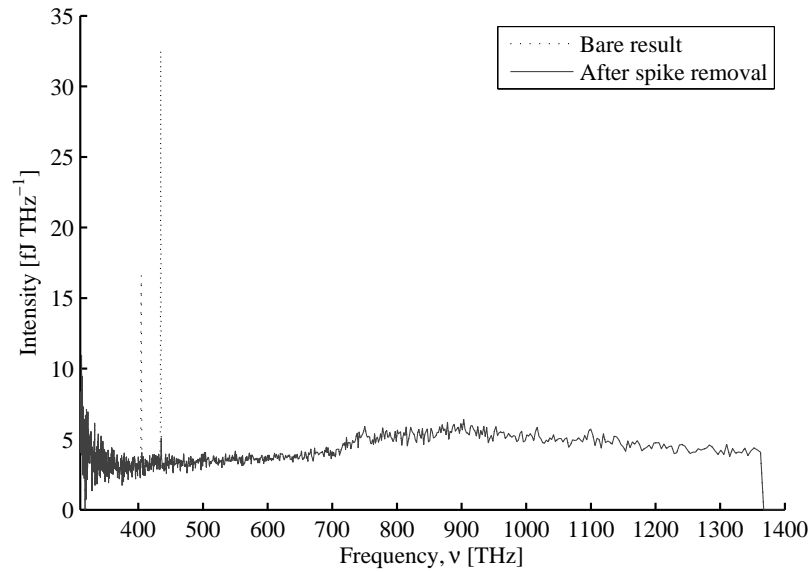


Figure E.1 – Removal of spikes example in an uncompressed bunch.

The spectrum is firstly divided into 10 domains in order to correct for the different signal to noise ratio domains of the spectrometer. Secondly the standard deviation σ and the mean μ of the intensity is calculated for each domain. All data points outside the range $\mu + 5\sigma$ are overwritten to take the value μ . 5σ corresponds to an confidence interval of $(1 - 2.9E-7)$. The process was repeated five times in order to remove all spikes in the spectrum. Due to the high confidence level the spikes could be removed accurately without altering other data.

F Software Code to Determine the Bunch Length with the TDC

```
1 clear all
2 close all
3
4 %This program reconstructs the longitudinal time profile of the bunch.
5 for u = 1:2
6     % Load the streaked and unstreaked image.
7     if u == 1
8         Data = importdata('X:/intranet/FIN/Data/FIN250-Phase3X/2013-11-01/DAQ
9                             20131101T151024.h5')
10        elseif u == 2
11            Data = importdata('X:/intranet/FIN/Data/FIN250-Phase3X/2013-11-01/DAQBL
12                                20131101T144948.h5')
13        end
14    for p = 1:length(Data.entry1.F10D101_DSCR10_CCAM2.CameraData(1,1,1,:))
15        i
16        calibration_time = 10.72; %mm/ps
17        Momentum_cal = 0.7284823; %keV/mm
18        Bunch_charge = 200; %pC
19
20        for k = 1:5
21
22            % Subtract background
23            img_raw = Data.entry1.F10D101_DSCR10_CCAM2.CameraData(:, :, k, p);
24            bgr = Data.entry1.F10D101_DSCR10_CCAM2.MultipleBackgroundImages(:, :, p);
25            img = double(img_raw) - bgr;
26            PixelsizeY = Data.entry1.F10D101_DSCR10_CCAM2.PixelSizeY;
27            PixelsizeX = Data.entry1.F10D101_DSCR10_CCAM2.PixelSizeX;
28
29            % get_ROI by Minjie Yan sets the background to zero, get_ROI(image,1 or
30            0,background noise level)
31            img_reduced(:, :) = get_ROI(img, 1, 5);
32
33            jj = 0;
34
35            %The for-loop calculates the Mean and Rms of the longitudinal phase space
36            . The slice is taken in the momentum space. The Mean and Rms are in
37            temporal space. The intensity is the integrated intensity of the slice
38            in momentum space.
39            for j = 1:length(img_reduced(1,:))
40                if length(find(img_reduced(:, j) > 0)) > 2
41                    [Mean(j) Rms(j)] = rms(1:length(img_reduced(:, j)), img_reduced(:, j)
```

Appendix F. Software Code to Determine the Bunch Length with the TDC

```

    ');
    Intensity(j) = sum(img_reduced(:,j));
elseif length(find(img_reduced(:,j) > 0)) <= 2
    Mean(j) = 0;
    Rms(j) = 0;
    Intensity(j) = 0;
end
end

%Plot the deviation of the streaked to the unstreaked and the intensity
of the slice versus the slice number
delta = linspace(-length(Mean)/2-0.5,length(Mean)/2-0.5,length(Mean)).*
    PixelsizeX*Momentum_cal;
time = (Mean).*PixelsizeY./calibration_time*1E3;
charge = (Intensity(:)./sum(Intensity(:)).*Bunch_charge)';
Mean_sub = Mean;

%In order to filter out the lower intensity, which do not contribute to
the current profile we set an offset of 5 per cent of the maximum
intensity.
limit_intensity = find(Intensity > 0.05 * max(Intensity));
Intensity_limit = Intensity(limit_intensity);
Min = min(Mean_sub(limit_intensity));
Max = max(Mean_sub(limit_intensity));

%The number of bins in the current profile
nbins = 50;
range = linspace(Min,Max,nbins);

%Sort the charges into equal time bins
for i = 1:nbins-1
    B = find(Mean_sub(limit_intensity) > range(i) & range(i+1) > Mean_sub
        (limit_intensity));
    I(i) = sum(Intensity_limit(B))./length(B);
    if sum(Intensity_limit(B)) == 0
        I(i) = 0; %I(i-1);
    end
    X(i) = (range(i) + range(i+1))/2;
end

XXXX = X*PixelsizeY/calibration_time;
W = (I./sum(I)*Bunch_charge)./(XXXX(2)-XXXX(1));

[MEAN(k,p,u) RMS(k,p,u)] = rms(XXXX.*1E3,W)

end
end
end

Phase = Data.entry1.FINXB_Phase.SetpointValues;

%Plot the result
errorbar(Phase+56.68+270,(mean(RMS(:,:),1))+mean(RMS(:,:),2))./2,(std(RMS(:,:),1))
    ./length(std(RMS(:,:),1)') + std(RMS(:,:),2))./length(std(RMS(:,:),2)'))./2,'
    linestyle','none','marker','.', 'markersize',10,'color',[0 0 0],'displayname','
    TDC Zero crossing 0~{\circ}')
```

G Software Code to Determine the Bunch Length Using Spectral Fluctuations

```

1 clear all
2 close all
3 %Calculate the single spectrum correlation
4 %running_mean_width = 100;
5
6 Correlation_width = 2500;
7
8 for k = 1:11
9     if k == 1
10         file = 'XB_2815_deg';
11         Phase(k) = 281.5;
12     elseif k == 2
13         file = 'XB_2820_deg';
14         Phase(k) = 282.0;
15     .
16     .
17     .
18 end
19
20 Correlation_width_half = round(Correlation_width/2);
21 for j = 1:50
22     % Load the data.
23     Data = importdata(['Y:\SITF_COTR_Experiments\2013-09-01\' file '\' file
24         sprintf('%0.5d',j-1) '.txt']);
25
26     % multiply with the calibration file and convert the the frequency domain
27     .
28     data_x = Data.data(:,1);
29     data_y = Data.data(:,2);
30     [x,y] = QE65000_calibration_win(data_x,data_y);
31     [nu1 dIdnu1] = lambda2freq_Domain(x(1:end-24)*1E-9,y(1:end-24));
32
33     % Remove the spikes in the spectra.
34     Spikeless1 = remove_spike(dIdnu1);
35     nu = nu1(1:end);
36     Spikeless = Spikeless1(1:end);
37
38     % Linearise the frequency bins.
39     xi = linspace(min(nu),max(nu),2E4);
40     yi = interp1(nu,Spikeless,xi,'pchip');
41     yii = yi;

```

Appendix G. Software Code to Determine the Bunch Length Using Spectral Fluctuations

```
41      % Calculate the correlation between two variables X and Y.
42      for i = 1:Correlation_width
43          ii = i;
44          Delta_nu(i) = xi(1+i) - xi(1);
45          X = yii(300:end-Correlation_width);
46          Y = yii(ii + 300:end-Correlation_width+ii);
47
48          Correlation(i) = correlation(X,Y);
49      end
50
51
52      Delta_nu_interpl = Delta_nu;
53      Correlation_interpl(:,j,k) = Correlation;
54
55      % Find the first minimum in the correlation plot.
56      i = 0;
57      FLAG_ = 0;
58      while FLAG_ < 1
59          i = i+1;
60          if Correlation_interpl(i,j,k) < Correlation_interpl(i + 1,j,k)
61              if Correlation_interpl(i,j,k) < Correlation_interpl(i + 2,j,k)
62                  if Correlation_interpl(i,j,k) < Correlation_interpl(i + 3,j,k)
63                      if Correlation_interpl(i,j,k) < Correlation_interpl(i +
64                          4,j,k)
65                          if Correlation_interpl(i,j,k) < Correlation_interpl(i
66                              + 5,j,k)
67                              FLAG_ = 1;
68                              Delta_nu_interpl_min(j) = Delta_nu_interpl(i);
69                              Correlation_interpl_min = Correlation_interpl(i,j
70                                  ,k);
71                              end
72                          end
73                      end
74                  end
75              end
76          end
77
78          % Extract the FWHM
79          FWHM_limit = Correlation_interpl_min + (1-Correlation_interpl_min)/2;
80          FWHM_min = max(find(Correlation_interpl(:,j,k) < FWHM_limit));
81          FWHM_max = min(find(Correlation_interpl(:,j,k) < FWHM_limit));
82          FWHM(k,j) = Delta_nu_interpl(FWHM_max);
83      end
84
85      % FWHM in THz and plot the data.
86      FWHM = FWHM./1E12;
87      Correlation_FWHM_mean = mean(FWHM')
88      Correlation_FWHM_std = std(FWHM');
89
90      %Plot the result
91      errorbar(Phase, Correlation_FWHM_mean, Correlation_FWHM_std);
```

Bibliography

- [1] C. F. Varley. On the Discharge of Electricity. *The Royal Society*, Jan. 1871.
- [2] M. Pluecker. On the Action of the Magnet Upon the Electrical Discharge in Rarefield Gases. *Philosophical Magazine*, 16(105), 1858.
- [3] W. K. H. Panofsky. The Evolution of Particle Accelerators and Colliders. *SLAC Publication*, pages 36 – 44, Spring 1997.
- [4] J. J. Thomson and F. R. S. Cavendish. Cathode Rays. *The London, Edinburgh and Dublin Philosophical Magazine and Journal of Science*, 1897.
- [5] G. A. Schott. On the Electron Theory of Matter and on Radiation. *Philosophical Magazine*, 13(74):189 – 213, 1907.
- [6] J. P. Blewett. Radiation Losses in the Induction Electron Accelerator. *Physical Review*, 69(3 – 4), 1946.
- [7] J. P. Gordon, H. J. Zeiger, and C. H. Townes. The Maser - New Type of Microwave Amplifier, Frequency Standard and Spectrometer. *Physical Review*, 99(4):1264 – 1274, 1955.
- [8] B. Patterson. Ultrafast Phenomena at the Nanoscale: Science Opportunities at the SwissFEL X-ray Laser. *PSI Bericht*, 09-10, 2009.
- [9] R. Ganter. SwissFEL Conceptual Design Report. *PSI Bericht*, V19, 10-04, 2011.
- [10] H. Wiedemann. *Particle Accelerator Physics*. Springer-Verlag, third edition, 2007.
- [11] G. Berden, W. A. Gillespie, S. P. Jamison, E. A. Knabbe, A. M. MacLeod, A. F. G. van de Meer, P. J. Phillips, H. Schlarb, B. Schmidt, P. Schmueser, and B. Steffen. Benchmarking of Electro-Optic Monitors for Femtosecond Electron Bunches. *Physical Review Letters*, 99(16):164801, 2007.
- [12] S. E. Korbly, A. S. Kesar, R. J. Temkin, and J. H. Brownell. Measurement of Sub-Picosecond Bunch Lengths Using Coherent Smith-Purcell Radiation. *Physical Review Special Topics, Accelerators and Beams*, 9(2):022802, 2006.

Bibliography

- [13] D Xiang, X. F. Yang, W. H. Huang, C. X. Tang, Y. Z. Lin, W. H. Li, Q. Pan, and M. Li. Experimental Characterization of Sub-Picosecond Electron Bunch Length with Coherent Diffraction Radiation. *Chinese Physical Letters*, 25(7):2440–2443, 2008.
- [14] P. Muggli, M. J. Hogan, C. D. Barnes, D. Walz, P. Krejcik, R. H. Siemann, H. Schlarb, and R. Ischebeck. Coherent Transition Radiation to Measure the SLAC Electron Bunch Length. *Proceedings of 2005 Particle Accelerator Conference, Knoxville, Tennessee*, pages 4102–4104, 2005.
- [15] M. Röhrs, C. Gerth, H. Schlarb, B. Schmidt, and P. Schmuser. Time Resolved Electron Beam Phase Space Tomography at a Soft X-ray Free Electron Laser. *Physical Review Special Topics, Accelerators and Beams*, 12(5):050704, 2009.
- [16] P. Krejcik, F. J. Decker, Y. Ding, J. Frisch, Z. Huang, J. Lewandowski, H. Loos, J. Turner, M. H. Wang, J. Wang, J. Welch, and C. Behrens. Commissioning the New LCLS X-Band Transverse Deflecting Cavity with Femtosecond Resolution. *Proceedings of IBIC 2013, Oxford, UK, TUAL2:308*, 2013.
- [17] L. Wartski, S. Roland, J. Lasalle, M. Bolore, and G. Filippi. Interference Phenomenon in Optical Transition Radiation and its Application to Particle Beam Diagnostics and Multiple Scattering Measurements. *Journal of Applied Physics*, 46(8):3644 – 3653, 1975.
- [18] M. L. Ter-Mikaelian. *High Energy Electromagnetic Processes in Condensed Media*, page 200. Wiley-Interscience, 1971.
- [19] H. Wiedemann. *Particle Accelerator Physics*. Springer-Verlag, second edition, 1993.
- [20] F. G. Bass and V. M. Yakovenko. Theory of Radiation from a Charge Passing Through an Electrically Inhomogeneous Medium. *Soviet Physics Uspekhi*, 8(3):189–230, 1965.
- [21] M. L. ter Mikaelian. *High Energy Electromagnetic Processes in Condensed Media*. Number 29. John Wiley and Sons, 1972.
- [22] A. P. Potylitsyn, M. I. Ryazanov, M. N. Strikhanov, and A. A. Tishchenko. *Diffraction Radiation from Relativistic Particles*, volume 239. Springer Berlin Heidelberg, 2009.
- [23] Plasma oscillation. retrieved: Oct. 2014. http://en.wikipedia.org/wiki/Plasma_oscillation.
- [24] C. J. Hirschmugl, M. Sagurton, and G. P. Williams. Multiparticle Coherence Calculations for Synchrotron-Radiation Emission. *Physical Review A*, 44(2):1316 – 1320, 1991.
- [25] S. Wesch, B. Schmidt, C. Behrens, H. D. Hashemi, and P. Schmuser. A Multi-Channel THz and Infrared Spectrometer for Femtosecond Electron Bunch Diagnostics by Single-Shot Spectroscopy of Coherent Radiation. *Nuclear Instruments and Methods in Physics Research A*, 665:40 – 47, 2011.

-
- [26] C. Behrens, N. Gerasimova, C. Gerth, E. A. Schmidt, B. Schneidmiller, S. Serkez, S. Wesch, and M. V. Yurkov. Constraints on Photon Pulse Duration from Longitudinal Electron Beam Diagnostics at a Soft X-ray Free Electron Laser. *Physical Review Special Topics, Accelerators and Beams*, 15:030707, 2012.
- [27] D. Egger. Notes on Measuring the Bunch Length at SITF/SwissFEL with Incoherent SR. *Internal notes, PSI*, 2011.
- [28] V. Sajaev. Measurement of Bunch Length Using Spectral Analysis of Incoherent Radiation Fluctuations. *Beam Instrumentation Workshop, 2004. US department of Energy, Contract No. W-31-109-ENG-38*.
- [29] F. Sannibale, G. V. Stupakov, M. S. Zolotarev, D. Filippetto, and L. Jägerhofer. Absolute Bunch Length Measurements by Incoherent Radiation Fluctuation Analysis. 2009.
- [30] M. S. Zolotarev and G. V. Stupakov. Spectral Fluctuations of Incoherent Radiation and Measurement of Longitudinal Bunch Profile. *Particle Accelerator Conderence*, pages 2180 – 2182, 1997.
- [31] P. Catravas, W. P. Leemans, J. S. Wurtele, M. S. Zolotarev, M. Babzien, I. Ben-Zvi, Z. Segalov, X. J. Wang, and V. Yakimenko. Measurement of Electron-Beam Bunch Length and Emit-tance Using Shot Noise Driven Fluctuations in Incoherent Radiation. *Physical Review Letters*, 82(26):5261–5264, 1999.
- [32] A. A. Lutman, Y. Ding, Y. Feng, Z. Huang, M. Messerschmidt, J. Wu, and J. Krzywinski. Femtosecond X-ray Free Electron Laser Pulse Duration Measurement from Spectral Correlation Function. *Physical Review Special Topics - Accelerators and Beams*, 15(3):030705, 2012.
- [33] D. C. Montgomery and Runger G. C. *Applied Statistics and Probability for Engineers*. J. Wiley & Sons, 2007.
- [34] R. J. Serfling. *Approximation Theorems of Mathematical Statistics*. J. Wiley & Sons, 2008.
- [35] M. Schreck and P. Wesolowski. Analytical Bunch Compression Studies for FLUTE. *physics.acc-ph*, 2014.
- [36] B. Beutner. *Measurement and Analysis of Coherent Synchrotron Radiation Effects at FLASH*. DESY, 2007.
- [37] M. Reiser. *Theory and Design of Charged Particle Beams*. John Wiley and Sons, 1994.
- [38] P. Emma, J. Frisch, and P. Krejcik. A Transverse Deflecting Structure for Bunch Length and Phase Space Diagnostics. *SLAC publication, LCLS-TN-00-12*, 2000.
- [39] C. P. Hauri and R. Ganter. Gun Laser Systems for the SwissFEL Project. *Proceedings of FEL 2009, Liverpool, UK*, MOPC63:157 – 160, 2009.

Bibliography

- [40] M. Yan. *Suppression of COTR in Electron Beam Imaging Diagnostics at FLASH*. Universitaet and DESY Hamburg, 2011.
- [41] M. Pedrozzi. SwissFEL Injector Conceptual Design Report, Accelerator Test Facility for SwissFEL. *PSI Bericht*, 10-05, 2010.
- [42] K. Floettmann. Astra (A Space charge TRacking Algorithm). DESY, 2011.
- [43] M. Borland. Elegant: A Flexible SDDS-Compliant Code for Accelerator Simulations. Advanced Photon Source LS-287, Sept. 2000.
- [44] M. Dohlus and T. Limberg. CSRtrack Version 1.2. DESY.
- [45] T. Schietinger, M. Aiba, S. Bettoni, B. Beutner, M. Divall, K. Doshekenov, Y. C. Du, M. Guetg, C. P. Hauri, R. Ischebeck, F. Le Pimpec, N. Milas, G. L. Orlandi, M. Pedrozzi, P. Peier, E. Prat, S. Reiche, B. Smit, A. Trisorio, and C. Vicario. Progress Report on the SwissFEL Injector Test Facility. *Proceedings of IPAC 2012, New Orleans, USA*, (TUPPP065), 2012.
- [46] P. Emma, C. Behrens, and H. Loos. Fast, Absolute Bunch Length Measurements in a Linac Using an Improved RF Zero-Phasing Method. *34th International Free Electron Laser Conference, FEL 2012, Japan*, 2012.
- [47] H. Loos. Reconstruction of a filamentary phase space from two projections.
- [48] E. Prat and M. Aiba. General and efficient dispersion-based measurement of beam slice parameters. *Physical Review Special Topics - Accelerators and Beams*, 17(3):032801, 2014.
- [49] H. Loos, T. Borden, P. Emma, J. Frisch, and J. Wu. Relative Bunch Length Monitor for the Linac Coherent Light Source (LCLS) Using Coherent Edge Radiation. *Proceedings of PAC07, Albuquerque, New Mexico, USA*, FRPMS071:4189–4191, 2007.
- [50] R. Ischebeck, B. Beutner, B. Steffen, and V. Schlott. Screen Monitor Design for the SwissFEL. *Proceedings of DIPAC09, Basel, Switzerland*, TUPD45:405–407, 2009.
- [51] E. D. Palik and G. Ghosh. *Handbook of Optical Constants of Solids*. Academic Press, 2nd edition, 1998.
- [52] Edmund Optics. Reflectivity Curves NT48-569 and NT47-107. www.edmundoptics.com, Accessed on 08-03-2014.
- [53] SONY. *Sony ICX204AL Diagonal 6mm (Type 1/3) Progressive Scan CCD Image Sensor with Square Pixel for B/W Cameras*.
- [54] P. E. Buchsbaum and H. J. Morris. Method for Making Monolithic Patterned Dichroic Filter Detector Arrays for Spectroscopic Imaging, 2000.
- [55] R. Akre, D. Dowell, P. Emma, J. Frisch, S. Gilevich, G. Hays, Ph. Hering, R. Iverson, C. Limborg-Deprey, H. Loos, A. Miahnahri, J. Schmerge, J. Turner, J. Welch, W. White, and J. Wu. Commissioning the Linac Coherent Light Source Injector. *Physical Review Special Topics, Accelerators and Beams*, 11(8):030703, 2008.

- [56] D. Ratner, A. Chao, and Z. Huang. Three Dimensional Analysis of Longitudinal Space Charge Microbunching Starting from Shot Noise. *Proceedings of FEL08, Gyeongju, Korea*, pages 338–341, 2008.
- [57] Y. S. Derbenev, J. Rossbach, E. L. Saldin, and V. D. Shiltsev. Microbunch Radiative Tail-Head Interaction. *TESLA FEL-Report 1995-05*.
- [58] C. A. Thomas, I. Martin, and G. Rehm. Bunch Length Measurement from Power Fluctuation at Diamond. *Proceedings of DIPAC2011, Hamburg, Germany*, 2011.
- [59] G. Andonian, A. Cook, M. Dunning, E. Hemsing, G. Marcus, A. Murokh, S. Reiche, D. Schiller, J. B. Rosenzweig, M. Babzien, K. Kutsche, and V. Yakimenko. Observation of Coherent Terahertz Edge Radiation from Compressed Electron Beams. *Physical Review Special Topics - Accelerators and Beams*, 12:030701, 2009.
- [60] A. S. Mueller, Y. L. Mathis, I. Birkel, B. Gasharova, C. J. Hirschmugl, E. Huttel, D. A. Moss, R. Rossmanith, and P. Wesolowski. Far Infrared Coherent Synchrotron Edge Radiation at ANKA. *Synchrotron Radiation News*, 19(3):18 – 24, 2006.

Curriculum Vitae

Personal Details

Full Name:	Bennie Smit
Born:	28th November, 1985 in Enschede, The Netherlands
Citizen of:	The Netherlands

Education

1999 - 2005	Bonhoeffer College Enschede, The Netherlands
2005 - 2009	B.Eng. Applied Physics Saxion University of Applied Science, Enschede, The Netherlands Thesis project: <i>Laser Induced Breakdown Spectroscopy</i>
2009 - 2010	M.Sc. Medical Physics University of Aberdeen, United Kingdom Masters Thesis: <i>Field Margins in Prostate Radiotherapy</i>
2011 - 2015	Ph.D. in Physics École Polytechnique Fédérale de Lausanne, EPFL, Switzerland Conducted at the Paul Scherrer Institute, Switzerland Subject: <i>Analysis of Femtosecond Electron Bunches at the SwissFEL Injector Test Facility</i>